

Functional properties and Ca^{2+} -dependent feedback
modulation of voltage-gated Ca^{2+} channels in
glutamatergic nerve terminals of the mammalian
auditory brainstem

Dissertation

for the award of the degree
“Dr. rerum naturalium” (Dr. rer. nat.)
Division of Mathematics and Natural Sciences
of the Georg-August-Universität Göttingen

Submitted by

Kun-Han Lin

From Tainan, Taiwan

Göttingen 2011

Member of the Thesis Committee:

Dr. Holger Taschenberger (Supervisor)

Research Group Activity-Dependent and Developmental Plasticity at the Calyx of Held
at the Max Planck Institute for Biophysical Chemistry, Göttingen

Dr. Takeshi Sakaba (Reviewer)

Research Group for Biophysics of Synaptic Transmission
at the Max Planck Institute for Biophysical Chemistry, Göttingen

Prof. Tobias Moser (Reviewer)

Dept. of Otorhynolaryngology, Georg-August-University Göttingen

Additional reviewers:

Prof. Erwin Neher Max-Planck Institute for Biophysical Chemistry, Göttingen

Prof. Thomas Dresbach Dept. of Anatomy and Embryology, Georg-August-University
Göttingen

Dr. Oliver M. Schlüter European Neuroscience Institute, Göttingen

Date of the thesis defense: at 2pm – 3:30pm, on 8th Apr. 2011

Declaration

I hereby declare that my PhD thesis '*Functional properties and Ca^{2+} -dependent feedback modulation of voltage-gated Ca^{2+} channels in glutamatergic nerve terminals of the mammalian auditory brainstem*' has been written independently with no other aids or sources than quoted.

Göttingen, March 11th 2011

.....

Content

| | |
|---|---------------|
| Introduction | - 1 - |
| 1.1 The auditory pathway | - 1 - |
| 1.2 The endbulb of Held synapse..... | - 1 - |
| 1.3 The calyx of Held synapse | - 4 - |
| 1.4 Voltage-gated calcium channels | - 5 - |
| 1.5 Calcium channel regulation and presynaptic plasticity | - 8 - |
| 1.6 Aim of this study..... | - 9 - |
| 1.6.1 Presynaptic Ca^{2+} influx and vesicle exocytosis at mouse endbulb of Held terminals..... | - 9 - |
| 1.6.2 Intracellular Ca^{2+} requirements for Ca^{2+} -dependent inactivation and facilitation of voltage-gated Ca^{2+} channels at rat calyx of Held synapse | - 9 - |
| Material and Methods | - 11 - |
| 2.1 Slice preparation | - 11 - |
| 2.2 Electrophysiology | - 13 - |
| 2.3 Flash photolysis and presynaptic Ca^{2+} imaging..... | - 15 - |
| 2.4 Ca^{2+} imaging during AP firing in nearly unperturbed terminals | - 16 - |
| 2.5 Analysis of electrophysiological data | - 17 - |
| Results | - 21 - |
| 3.1 Presynaptic Ca^{2+} influx and vesicle exocytosis at mouse endbulb of Held terminals..... | - 21 - |
| 3.1.1 Identification of endbulb of Held terminals in acute mouse brainstem slices containing the AVCN | - 21 - |
| 3.1.2 Passive membrane properties of endbulb and calyx of Held terminals | - 23 - |
| 3.1.3 Properties of voltage-gated Ca^{2+} currents at endbulb and calyx terminals .. | - 25 - |
| 3.1.4 Establishing an HH-type m^2 model of $I_{\text{Ca(V)}}$ in endbulb terminals..... | - 28 - |
| 3.1.5 Simulating Ca^{2+} influx following presynaptic APs..... | - 30 - |
| 3.1.6 Estimating the total number of VGCC expressed at endbulb and calyx terminals..... | - 33 - |
| 3.1.7 $I_{\text{Ca(V)}}$ inactivation and facilitation in endbulb and calyx terminals | - 35 - |
| 3.1.8 Ca^{2+} -dependent vesicle exocytosis assayed by ΔC_m measurements in endbulb and calyx terminals | - 38 - |
| 3.2 Intracellular Ca^{2+} requirements for Ca^{2+} -dependent inactivation and facilitation of voltage-gated Ca^{2+} channels at rat calyx of Held synapse..... | - 43 - |
| 3.2.1 Inactivation of presynaptic voltage-gated Ca^{2+} channels..... | - 43 - |
| 3.2.2 Clustering of presynaptic VGCC may account for insensitivity of $I_{\text{Ca(V)}}$ inactivation to Ca^{2+} chelators..... | - 47 - |
| 3.2.3 Recovery of $I_{\text{Ca(V)}}$ from inactivation | - 49 - |
| 3.2.4 Probing the $[\text{Ca}^{2+}]_\text{i}$ sensitivity of $I_{\text{Ca(V)}}$ inactivation by UV-light flash photolysis of caged Ca^{2+} | - 51 - |
| 3.2.5 Characterization of $I_{\text{Ca(V)}}$ facilitation | - 55 - |
| 3.2.6 $[\text{Ca}^{2+}]_\text{i}$ transients during AP firing in nearly unperturbed calyx terminals .. | - 57 - |
| 3.2.7 Modulation of $I_{\text{Ca(V)}}$ during trains of AP-like depolarizations | - 60 - |

| | |
|--|---------------|
| Discussion..... | - 63 - |
| 4.1 Presynaptic Ca^{2+} influx and vesicle exocytosis at mouse endbulb of Held terminals..... | - 63 - |
| 4.1.1 Unequivocal identification of endbulb terminals..... | - 64 - |
| 4.1.2 Heterogeneous size of endbulb terminals | - 64 - |
| 4.1.3 Fast presynaptic APs in endbulb terminals..... | - 65 - |
| 4.1.4 Rapidly gating Ca^{2+} channels in endbulb terminals..... | - 66 - |
| 4.1.5 Absence of $I_{\text{Ca(V)}}$ inactivation during AP-like trains..... | - 68 - |
| 4.1.6 A large pool of releasable vesicles in endbulb terminals..... | - 68 - |
| 4.2 Intracellular Ca^{2+} requirements for Ca^{2+} -dependent inactivation and facilitation of voltage-gated Ca^{2+} channels at rat calyx of Held synapse..... | - 70 - |
| 4.2.1 Two kinetically distinct components of inactivation | - 70 - |
| 4.2.2 Glutamate release-dependent decrease of $I_{\text{Ca(V)}}$ | - 71 - |
| 4.2.3 Insensitivity of $I_{\text{Ca(V)}}$ inactivation to intracellular chelators | - 71 - |
| 4.2.4 Similar intracellular Ca^{2+} requirements for CDI and CDF | - 73 - |
| 4.2.5 Molecular identity of the Ca^{2+} sensor mediating CDI and CDF..... | - 74 - |
| Summary | - 75 - |
| Bibliography | - 77 - |
| Abbreviation | - 85 - |
| Acknowledgment..... | - 87 - |
| Curriculum Vitae | - 89 - |
| Publication list | - 91 - |

Introduction

1.1 The auditory pathway

The auditory system detects sound and uses acoustic cues to identify and locate sound sources in the environment. What differentiates the auditory system from other sensory systems is its impressive temporal acuity. Sound is a mechanical wave generated by oscillations of air pressure. This mechanical stimulus is transformed by the cochlea into a spike code. Specialized auditory neurons and circuits then use this information to build a neuronal representation of different features of the sound stimulus. For instance, the localization of sound sources in space can be inferred from differences in both arrival time as well as intensity level of sound stimuli arriving at the left and right ear. Figure 1.1 illustrates the circuitry in the superior olivary complex (SOC) of the mammalian brainstem which is involved in computing sound source localization from these two binaural cues. In order to preserve the temporal precision of spike activity for auditory information processing, several neurons in SOC apparently developed morphological and biophysical adaptations like fast-activating ion channels, thick-calibre axons, and large nerve terminals such as the two well-known calyx-type terminals – the calyx of Held and the endbulb of Held, which were first identified by the German anatomist Hans Held (1893).

1.2 The endbulb of Held synapse

Synapses formed between the endings of auditory nerve fibers and bushy cells in the anterior ventral cochlear nucleus (aVCN) are the first relay center in the mammalian

auditory pathway. The axons of spiral ganglion cells give rise to the endbulbs of Held, which synapse onto the spherical bushy cells (SBCs). In contrast to calyces of Held, up to four endbulb terminals can contact a single bushy cell as revealed by reconstructions of endbulb→SBC connections (Fig. 1.2) (Brawer and Morest, 1975; Ryugo and Sento, 1991).

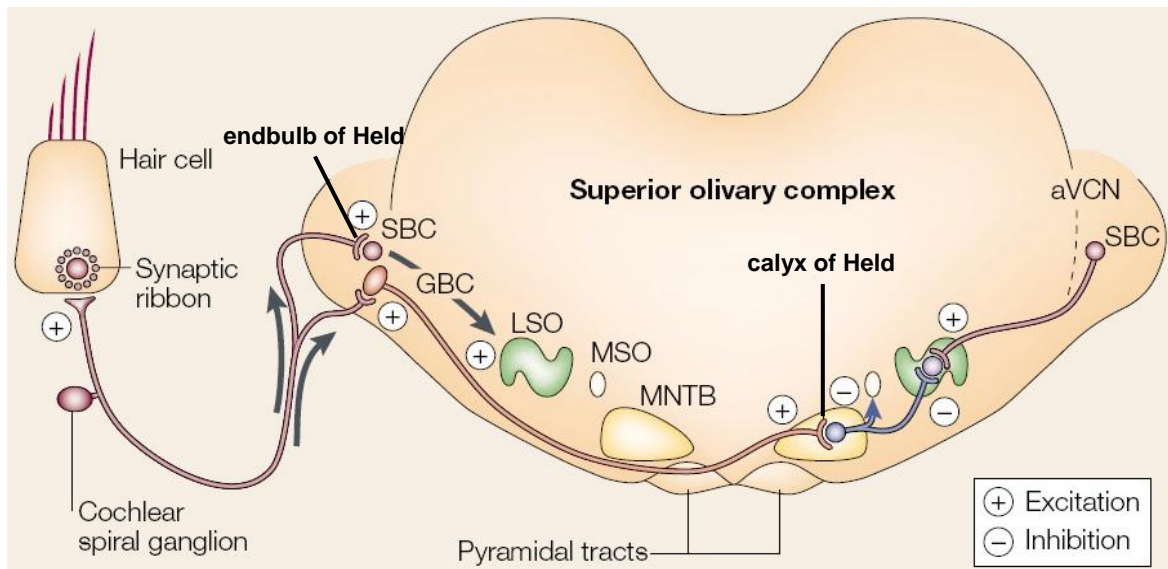


Figure 1.1 Schematic representation of auditory neuronal circuitry.

The hair cells which are responsible for the perception of sound in the cochlea convey information via auditory nerves to the anterior ventral cochlear nucleus (aVCN). Globular bushy cells (GBCs) and spherical bushy cells (SBCs) receive excitatory input from the auditory nerve fibers. The auditory nerve terminates at giant glutamatergic synapses - endbulbs of Held onto SBC. GBC axons cross the brainstem midline and give rise to another giant glutamatergic synapse - the calyx of Held which synapses onto a principal cell in the contralateral medial nucleus of the trapezoid body (MNTB). The glycinergic principal cell of the MNTB projects to the lateral superior olive (LSO) which also receives excitatory input from SBCs of the ipsilateral aVCN. The summation of excitatory and inhibitory inputs in the LSO is thought to play a role in sound source localization. Plus and minus signs indicate excitatory and inhibitory synapses. Adapted from von Gersdorff and Borst (2002).

A detailed morphological characterization of endbulb terminals was presented by Nicol and Walmsley (2002). They reconstructed four endbulb terminals from a P25 rat and reported an average number of 155 AZ with a nearest-neighbor separation of $\sim 0.15 \mu\text{m}$ and mean surface area of $\sim 0.07 \mu\text{m}^2$. These morphological features of endbulb AZs are similar to those of the calyx of Held terminals and other conventional synapses. Isaacson

and Walmsley (1995) recorded synaptic currents evoked in bushy cells by stimulating the auditory nerve. They found that EPSCs were blocked by glutamate antagonists and reported that bushy cells generate glutamatergic EPSCs with very fast kinetics. NMDA receptors contributed to synaptic transmission but their relative contribution decreased during postnatal development of the endbulb synapse. These results agree with immunohistochemical studies suggesting that endbulb terminals are glutamatergic. (Hackney et al., 1996).

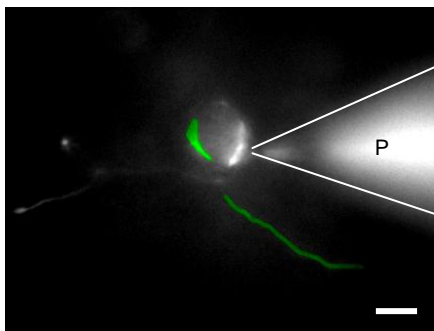


Figure 1.2 Each spherical bushy cell receives more than one giant synapse

Image of endbulb of Held terminals filled with a fluorescent dye via patch-clamp pipette (P). Green and white signals indicate two endbulb terminals, respectively. Scale bar, 10 μm

Endbulb terminals relay sensory information from inner hair cells to the SBCs. This information transfer can be modulated by synaptic plasticity which has been studied by recording postsynaptic currents in SBCs. Presynaptic recordings from endbulbs of Held have been proven technically challenging. However, to understand the mechanisms of presynaptic regulation, direct measurements from the presynaptic terminal are clearly advantageous. In this study, I achieved, for the first time, direct patch-clamp measurements from presynaptic endbulb of Held terminals. This approach enabled me to study in detail the properties of presynaptic VGGCs and their regulation, as well as Ca^{2+} -dependent exocytosis from endbulb terminals.

1.3 The calyx of Held synapse

The calyx of Held synapse is formed between globular bushy cells (GBCs) of the aVCN and principal neurons in the contralateral medial nucleus of the trapezoid body (MNTB). The unusual morphology of the calyx terminal consists of multiple, thick, finger-like structures that clasp the postsynaptic cell. Anatomical characterization further showed that each principal neuron in the MNTB receives one or rarely two calyceal inputs (Kuwabara et al. 1991). The first evidence that the calyx of Held uses glutamate as a neurotransmitter came from immunohistochemical studies (Grandes and Streit, 1989). Later, Banks and Smith (1992) used electrophysiological recordings in brainstem slices to directly demonstrate that excitatory postsynaptic currents (EPSCs) at the calyx synapse are blocked by glutamate antagonists. A detailed electron-microscopic morphological reconstruction of an entire calyx terminal and its contacting principle neuron in a P9 rat was performed by Sätzler et al. (2002). This study demonstrated that a single calyx harbors as many as 554 active zones (AZs). The average surface area of these AZ is $\sim 0.1 \mu\text{m}^2$ and their morphology is similar to that of AZs in conventional bouton-like synapses of the CNS. The axo-somatic contact together with the multiple release sites ensure reliable, rapid and precise synaptic transmission.

For more than a decade, the calyx of Held has been used as a model to study presynaptic ion channels, Ca^{2+} influx, transmitter release and its short-term modulation. It has become one of the most studied model synapses in recent years because its large size makes it directly accessible to electrophysiological recordings. It allows direct presynaptic voltage-clamp recordings, the use of Ca^{2+} indicator dyes as well as the manipulation of the intracellular Ca^{2+} concentration ($[\text{Ca}^{2+}]_i$). Recently, methods have been established

allowing to study the functional roles of different presynaptic proteins by making use of recombinant adenoviral vectors with high levels of transgene expression (Young and Neher, 2009). The expression pattern and mechanisms of regulation of voltage-gated Ca^{2+} channels (VGGCs) in nerve terminals of the mammalian CNS are still incompletely known. In the present study, we take advantage of the large size of the calyx of Held terminal to study the feedback modulation by intracellular Ca^{2+} of presynaptic VGGCs.

1.4 Voltage-gated calcium channels

Voltage-gated calcium channels are important signal transducers that couple electrical signaling to influx of calcium ions which in turn can regulate intracellular processes such as contraction, secretion, neurotransmission, and gene expression in many different cell types (Catterall, 2000). VGCCs are composed of several different subunits: α_1 , $\alpha_2\delta$, β , and γ . The α_1 subunit is the largest subunit. It forms the conducting pore and consists of the voltage-sensing machinery. Most of the drug, toxins or modulators of VGGCs bind to the α_1 subunit. In vertebrates, ten functional calcium channel α_1 subunits are defined by homology screening, and they are divided into three structurally and functionally related families (Fig. 1.3) (Ertel et al., 2000).

The Ca_v1 subfamily ($\text{Ca}_v1.1$ - $\text{Ca}_v1.4$) includes channels containing α_{1S} , α_{1C} , α_{1D} , and α_{1F} , which conduct L-type Ca^{2+} currents that initiate excitation-contraction coupling of muscle cells, endocrine secretion, and synaptic transmission at ribbon synapses of the auditory and visual pathway. L-type Ca^{2+} currents are “Long-Lasting” and exhibit a high threshold for activation (Fig. 1.3, HVA). Dihydropyridines, Ca^{2+} channel antagonists, that

selectively block L-type Ca^{2+} channels, are also useful because of their clinical effects on the heart and vascular smooth muscle (Striessnig, 1999).

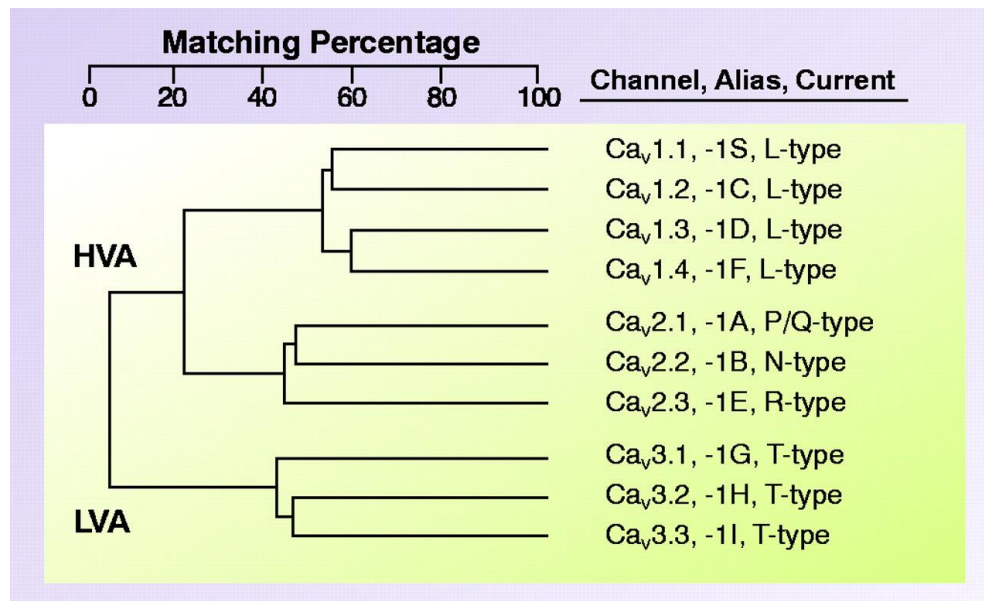


Figure 1.3 Three Subfamilies of voltage-gated calcium channels

Alignment of deduced amino acid sequences of $\alpha 1$ subunits indicates that these channels can be grouped into three subfamilies- Ca_v1 , Ca_v2 , and Ca_v3 . The comparison was restricted to membrane spanning regions and the P-loop of each homologous repeat region, so the more divergent intra- and extracellular loops were not considered. Taken from Perez-Reyes (2004).

The Ca_v3 subfamily ($\text{Ca}_v3.1$ - $\text{Ca}_v3.3$) includes channels containing $\alpha 1G$, $\alpha 1H$, and $\alpha 1I$, which mediate T-type Ca^{2+} currents that are important for depolarization of pacemaker cardiac cells, endocrine secretion, and for controlling patterns of repetitive action potential (AP) firing in neurons (Perez-Reyes, 2003). Compared to HVA Ca^{2+} channels, T-type Ca^{2+} channels open at more negative potentials (Fig. 1.3, LVA), even below the threshold for a typical Na^+ - K^+ -dependent AP. The Tiny unitary conductance and “Transient” Ca^{2+} current because of rapid inactivation are unique features of T-type Ca^{2+} channels (Catterall et al., 2005a; 2005b) Several chemical compounds such as pyridyl amide, 4-aminomethyl-4-fluoropiperidine and TTA-A2 recently have been proved as

potent and selective T-type calcium channel antagonists (Shipe et al., 2008; Kraus et al., 2010).

The Ca_v2 subfamily ($\text{Ca}_v2.1$ - $\text{Ca}_v2.3$) includes channels containing $\alpha 1A$, $\alpha 1B$, and $\alpha 1E$, subunits, which conduct P/Q-type (P for cerebellar Purkinje cells), N-type (N for Neural), and R-type Ca^{2+} (R for Residual) currents, respectively. Ca_v2 Ca^{2+} channels are primarily observed in central and peripheral neurons, where they are involved in fast synaptic transmission (Dunlap et al., 1995; Catterall, 2000). Similar to L-type Ca^{2+} channels, these channels have a high threshold for activation (Fig. 1.3, HVA). P/Q- and N-type channels can be identified by applying specific neurotoxic peptides: ω -agatoxin IVA (ω -AgaTX) from the venom of Funnel web spider and ω -conotoxin from cone snail venoms, respectively (Tsien et al., 1991; Miljanich and Ramachandran, 1995). R-type Ca^{2+} channels are resistant to blockers of L-, N-, and P/Q- type channels (Randall and Tsien, 1995). Only low-doses of Ni^{2+} , and in some preparations, SNX-482, a toxin derived from tarantula venom, can block them entirely, partially or not at all (Newcomb et al., 1998).

Before hearing onset, N-, P/Q-, and R-type channels coexist at calyx of Held terminals where they mediate synaptic transmission (Iwasaki and Takahashi, 1998; Wu et al., 1998; Iwasaki et al., 2000). During development, the relative fraction of N-type channels significantly declines and the fraction of P/Q-type channels increases. At postnatal day 10 (P10), presynaptic Ca^{2+} currents ($I_{\text{Ca}(V)}$) are predominantly mediated by P/Q-type channels (Iwasaki et al., 2000). Furthermore, $\text{Ca}_v2.1$ channels undergo a dual feedback regulation by incoming Ca^{2+} ions, CDF and CDI, was observed in calyces (Borst and Sakmann, 1998a; Cuttle et al., 1998; Forsythe et al., 1998). Ca^{2+} -dependent facilitation

develops rapidly with the first few milliseconds of repeated AP-like depolarization. Increased channel open probability (Chaudhuri et al., 2007) and/or a negative shift in the voltage-dependent activation of $I_{Ca(V)}$ (Borst and Sakmann, 1998b; Cuttle et al., 1998) may underlie the measured increase in amplitude. While CDF is a property unique to P/Q-type VGCCs, CDI is a ubiquitous process amongst many presynaptic VGCC subtypes whereby the entry of Ca^{2+} enhances channel closure during a maintained depolarization (DeMaria et al., 2001; Liang et al., 2003)

1.5 Calcium channel regulation and presynaptic plasticity

Synaptic transmission at most fast chemical synapses is controlled by Ca^{2+} influx through Ca_v2 channels. Several mechanisms directly or indirectly modulate the function of these Ca^{2+} channels and thereby regulate synaptic strength. At the calyx of Held, glutamate binding to presynaptic metabotropic glutamate receptors (mGluR) has been demonstrated to suppress the presynaptic Ca^{2+} conductance (Takahashi et al., 1996). Similarly, $I_{Ca(V)}$ can be inhibited by endo-cannabinoids, which are released after via postsynaptic mGluR activation and bind to CB1 receptors (Kushmerick et al., 2004). However, metabotropic feedback modulation of $I_{Ca(V)}$ contributes only little to short-term synaptic depression (von Gersdorff et al., 1997). Therefore, vesicle depletion is generally believed to be the major mechanism of synaptic depression. In addition, at lower frequencies (2 to 30 Hz) and during long-lasting tetanic stimulation at high frequency, CDI of $I_{Ca(V)}$ was shown to contribute significantly to synaptic depression (Forsythe et al., 1998; Xu and Wu, 2005).

Synaptic facilitation is thought to be mediated by an increase in the residual $[Ca^{2+}]_i$ and/or by CDF of VGCCs. The relative contribution of CDF to synaptic facilitation is

still under debate (Ishikawa et al., 2005; Inchauspe et al., 2007; Muller et al., 2008). But, both, paired-pulse facilitation of $I_{Ca(V)}$ as well as paired-pulse facilitation of synaptic transmission are abolished in $\alpha 1A$ -deficient (P/Q-type channel KO) mice. This finding further supports the notion that CDF of P/Q-type channels significantly contributes to synaptic facilitation.

1.6 Aim of this study

This study is composed of two main projects: a characterization of presynaptic VGCCs and their regulation in endbulb of Held terminals (1.6.1) and a detailed study of CDI and CDF of VGCCs in calyx of Held terminals as well as a characterization of the dynamics of AP-induced intracellular Ca^{2+} transients in nearly unperturbed calyx terminals (1.6.2).

1.6.1 Presynaptic Ca^{2+} influx and vesicle exocytosis at mouse endbulb of Held terminals

Direct presynaptic recordings were performed in endbulb of Held terminals to study expression and gating properties of their presynaptic VGCCs. In order to characterize AP-driven $I_{Ca(V)}$ at this synapse, we established a Hodgkin-Huxley m^2 type kinetic scheme of $I_{Ca(V)}$. In addition, we characterized Ca^{2+} -dependent vesicle exocytosis and quantified the size of the pool of readily releasable vesicles by means of membrane capacitance recordings.

1.6.2 Intracellular Ca^{2+} requirements for Ca^{2+} -dependent inactivation and facilitation of voltage-gated Ca^{2+} channels at rat calyx of Held synapse

We took advantage of the large size of the calyx of Held to study Ca^{2+} -dependent regulation of presynaptic P/Q-type VGCCs. In particular, we were interested to determine

the intracellular Ca^{2+} requirements for CDI and CDF and relate those to changes in $[\text{Ca}^{2+}]_i$ typically occurring during presynaptic AP firing. To this end, we combined whole-cell recordings of presynaptic $I_{\text{Ca(V)}}$ with Ca^{2+} uncaging via flash photolysis while monitoring presynaptic $[\text{Ca}^{2+}]_i$ with Ca^{2+} indicator dyes.

Material and Methods

2.1 Slice preparation

Brainstem slices were prepared from (P8–P10) Wistar rats and C57BL/6N mice (P9–11). For comparison, some recordings were also obtained from P9–11 α_{1A} -deficient ($\alpha_{1A}^{-/-}$) mice (Jun et al., 1999) and in some cases from P14–16 rats. All brainstem slices were prepared in accordance with animal care and use guidelines of the State of Lower Saxony as previously described (Taschenberger and von Gersdorff, 2000). Briefly, rats or mice were decapitated and the skull was opened by carefully cutting along the midline from the neck close to eyes. Additional four cuts along the mediolateral axis were applied to exposure the entire brain. The cerebrum close to the rostral-dorsal region was cut at an angle of $\sim 20^\circ$ to the midsagittal plane and second cut was applied close to the eye line. The entire cerebrum was quickly removed from the cut-open skull with forceps and then immersed into ice-cold low Ca^{2+} artificial CSF (aCSF) containing (in mM): 125 NaCl, 2.5 KCl, 3 MgCl_2 , 0.1 CaCl_2 , 10 glucose, 25 NaHCO_3 , 1.25 NaH_2PO_4 , 0.4 ascorbic acid, 3 myo-inositol, and 2 Na-pyruvate, pH 7.3. For aVCN preparation, gently removing the whole cerebellum with forceps is an additional process for improving visibility while disconnecting the auditory nerve from the AVCN. Using cold and low Ca^{2+} aCSF helped to prevent hypoxic damage of the nerve cells and down-regulated the metabolic activity. In order to facilitate the slicing, fine forceps were used to remove the arachnoid mater and the pia mater. The remaining brainstem was glued onto the stage of a VT1000S vibratome (Leica, Nussloch, Germany). The 7th cranial nerve was used as a landmark indicating the start of the region of interest containing MNTB and aVCN (Fig. 2.1). Once

the 7th nerve was visible, coronal slices (180–200 μm) containing the AVCN were collected. In contrast, slices containing the medial nucleus of the trapezoid body (MNTB) were collected immediately after the 7th nerve disappeared. Slices were incubated for ≥ 30 min at 35 $^{\circ}\text{C}$ in an incubation chamber containing normal aCSF and kept at room temperature (22–24 $^{\circ}\text{C}$) for 4 h thereafter. The composition of normal aCSF was identical to low Ca^{2+} aCSF except that 1.0 mM MgCl_2 and 2.0 mM CaCl_2 were used. All solutions were oxygenated by continuous equilibration with carbogen gas (95% O_2 , 5% CO_2).

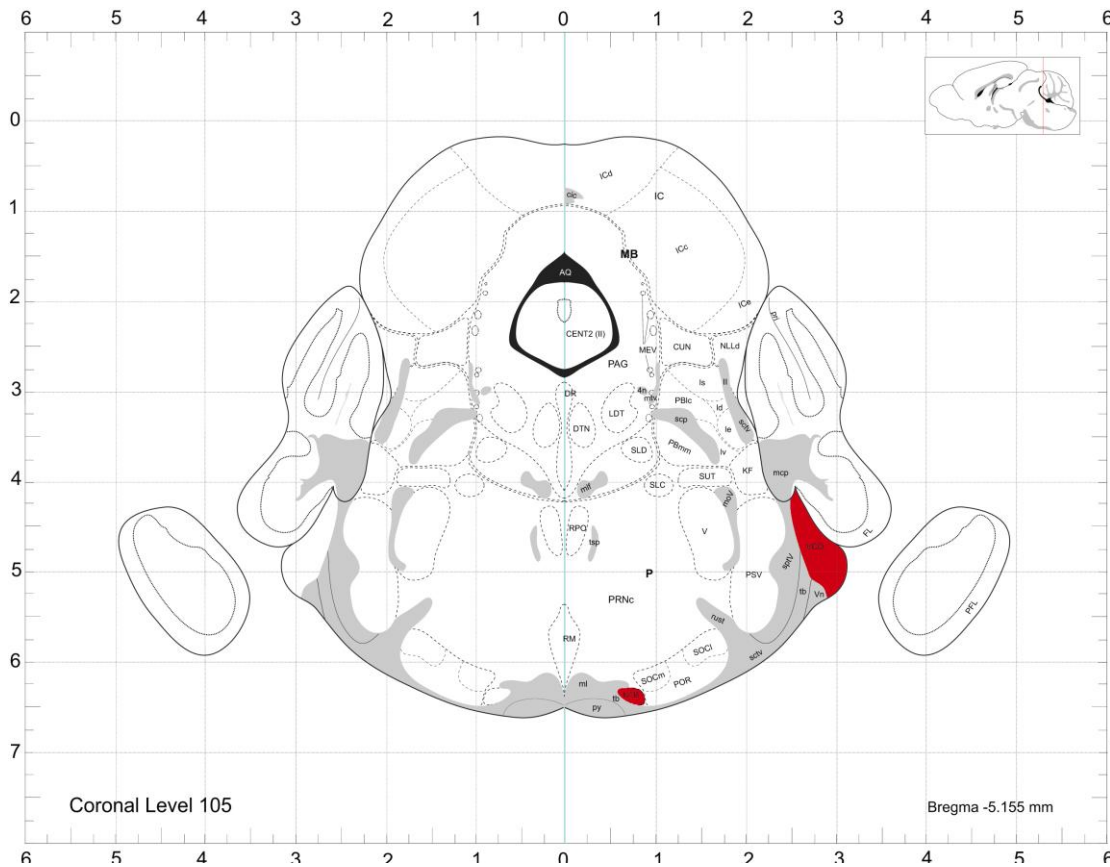


Figure 2.1 Coronal section of the adult rat brain

Slice preparation procedure. Schematic map of a transverse slice, containing the region of interest which is labeled in red: medial nucleus of the trapezoid body (MNTB), marked “NTB”, and “VCO” is anterior ventral cochlear nucleus (aVCN). While slicing, the 7th nerve served as a marker that indicated the start of the region of interest. Modified from “Allen reference atlas” (Dong, 2008)

2.2 Electrophysiology

Patch-clamp recordings were made from endbulb of Held terminals, SBCs of the AVCN, calyx of Held terminals and principal cells of the MNTB using an EPC-10 amplifier controlled by Pulse software (HEKA Elektronik, Lambrecht/Pfalz, Germany). Sampling intervals and filter settings were 20 μ s and 4.5 kHz, respectively. Cells were visualized by differential interference contrast microscopy through a 60 \times water-immersion objective (NA 1.0, Olympus, Hamburg, Germany) using an Axioskop FS microscope (Zeiss, Oberkochen, Germany). All experiments were performed at room temperature.

Patch pipettes were pulled from Borosilicate glass (Science Products GmbH, Hofheim, Germany) on a P-97 micropipette puller (Sutter Instrument, Novato, CA). Pipettes were coated with dental wax to minimize fast capacitive transients during voltage-clamp experiments and to reduce stray capacitance. Open tip pipette resistance was 4–5 M Ω . Access resistance (R_s) values were ≤ 30 M Ω and ≤ 20 M Ω for recordings from endbulb and calyx terminals, respectively. R_s was compensated 50–60% during presynaptic voltage-clamp experiments.

For measuring $I_{Ca(V)}$ and membrane capacitance (ΔC_m), pipettes were filled with a solution containing (in mM): 100 Cs-gluconate, 30 TEA-Cl, 30 CsCl, 10 HEPES, 0.5 EGTA, 5 Na₂-phosphocreatine, 4 ATP-Mg, 0.3 GTP, pH 7.3 with CsOH. The pipette solution was supplemented with varying concentrations of EGTA or BAPTA as indicated. The bath solution was supplemented with 1 μ M TTX, 1 mM 4-AP, and 40 mM TEA-Cl to suppress voltage-gated sodium and potassium currents. In some experiments a

cocktail of antagonists (50 μ M D-AP5, 5 μ M NBQX, 300 μ M CPPG and 5 μ M AM251) was applied in order to study a possible inactivation of presynaptic $I_{Ca(V)}$ by mechanisms that involve depletion of Ca^{2+} ions from the synaptic cleft and/or activation of metabotropic glutamate or cannabinoid receptors negatively coupled to presynaptic VGCCs (see Fig. 3.2.3). For pharmacological dissection of $I_{Ca(V)}$, ω -Agatoxin IVA (ω -AgaTX; 200 nM) (Alomone Labs, Jerusalem, Israel) was dissolved in aCSF containing 0.1 mg/ml Cytochrome *c*. Because a saturating concentration of ω -AgaTX was applied, complications resulting from voltage-dependent toxin unblock were highly unlikely (Mintz et al., 1992).

Changes in membrane capacitance (Reim et al.) were monitored using the Sine+DC technique (Lindau and Neher, 1988) with a software lock-in amplifier (HEKA Pulse) by adding a 1 kHz sine-wave voltage command (amplitude ± 35 mV) to the holding potential (V_h) of -80 mV. To avoid a contamination of ΔC_m estimates after long-lasting presynaptic depolarizations with small C_m transients unrelated to vesicle exocytosis (Yamashita et al., 2005), ΔC_m was estimated from the averaged C_m values during 50 ms time windows immediately before and 450 ms after the end of the depolarizations. Presynaptic recordings with a leak current >150 pA were excluded from the analysis.

Presynaptic APs were elicited by either depolarizing current injections or afferent fiber stimulation. Stimulation pulses (100 μ s duration) were applied using a stimulus isolator unit (A.M.P.I., Jerusalem, Israel), with the output voltage set to 1–2 V above threshold for AP generation (≤ 40 V). APs were measured in the current-clamp mode of the EPC-10 after carefully adjusting the fast-capacitance cancellation in cell-attached mode. For

measuring APs, pipettes were filled with a solution containing (in mM): 100 K-gluconate, 60 KCl, 10 HEPES, 5 EGTA, 5 Na_2 -phosphocreatine, 4 ATP-Mg, 0.3 GTP, pH 7.3 with KOH. No liquid junction potential corrections (<10 mV) were applied.

2.3 Flash photolysis and presynaptic Ca^{2+} imaging

A UV flash lamp (Rapp Optoelectronic, Hamburg, Germany) was used to uncage Ca^{2+} from DM-nitrophen to elicit step-like elevations of the intracellular free Ca^{2+} concentration ($[\text{Ca}^{2+}]_i$) in presynaptic terminals (Schneggenburger and Neher, 2000). Different postflash amplitudes of $[\text{Ca}^{2+}]_i$ were obtained by controlling the flash light intensity using neutral density filters and/or by varying the concentration of DM-nitrophen in the pipette solution (0.6 to 9 mM).

Presynaptic $[\text{Ca}^{2+}]_i$ was monitored using the ratiometric Ca^{2+} indicator dyes Fura 4F ($K_d = 1 \mu\text{M}$) or Fura 2FF ($K_d = 10 \mu\text{M}$), which were excited at 350 and 380 nm by a monochromator (Polychrome 5, TILL Photonics, Gräfelfing, Germany). Fluorescent images were collected with an interline-transfer 640×480 -pixel CCD (VGA, TILL Photonics, Gräfelfing, Germany). To allow for brief exposure times, on-chip pixel binning (8×15) was used. Monochromator and CCD camera were controlled by the TILLvisION software (TILL Photonics, Gräfelfing, Germany). Presynaptic patch pipettes contained (in mM): 100–125 Cs-gluconate, 20 TEA-Cl, 20 HEPES, 0.5 MgCl_2 , 5 Na_2 -ATP, 0.3 GTP, 0.5–9 DM-Nitrophen, 0.3–7.8 CaCl_2 , and 0.2 Fura 2FF or 0.2 Fura 4F, pH 7.3 with CsOH. Time series images were analyzed off-line using Igor Pro software. The background fluorescence of a small area adjacent to the region of interest was subtracted

to obtain the background-corrected fluorescence ratio $R = F_{350}/F_{380}$. That ratio was converted into the $[\text{Ca}^{2+}]_i$ using the following equation (Grynkiewicz et al., 1985):

$$[\text{Ca}^{2+}]_i = K_{\text{eff}} (R - R_{\min}) / (R_{\max} - R).$$

The calibration constants (K_{eff} , R_{\max} and R_{\min}) for each dye were obtained from *in vitro* measurements.

2.4 Ca^{2+} imaging during AP firing in nearly unperturbed terminals

For measuring AP-evoked Ca^{2+} transients in unperturbed calyces, presynaptic patch pipettes were filled with K-gluconate based solution described above plus the low affinity Ca^{2+} dye Fura-6F (300 μM , $K_d = 15 \mu\text{M}$). To preload calyx terminals with $\sim 100\text{--}150 \mu\text{M}$ Fura-6F, whole-cell recording configuration was established for a period of 40 to 60 s (depending on R_s) and thereafter the pipette was gently retracted. The dye loading kinetics was obtained from a separate set of experiments in which changes of fluorescence intensities were recorded every 10 s at the isobestic point of Fura 6F ($\lambda = 358 \text{ nm}$) in whole-cell configuration (see Fig. 3.2.11A). Based on that dye loading time course, we estimate that the preloading procedure achieved a final cytosolic concentration of $\sim 125 \mu\text{M}$ Fura-6F.

To increase the time resolution and minimize photobleaching, single-wavelength imaging of the Ca^{2+} -sensitive fluorescence at 380 nm was applied during AP firing at an acquisition rate of 100 Hz (Müller et al., 2007). Single wavelength images were preceded and followed by 20 images taken with dual excitation at wavelengths of 350 nm and

380 nm. Fluorescence signals were converted into $[Ca^{2+}]_i$ using the following equation (Lee et al., 2000b):

$$[Ca^{2+}]_i = K_{eff} (R' - (R_{min} + \alpha)) / ((R_{max} + \alpha) - R'),$$

where α (0.237) is the isocoefficient of Fura-6F and R' is the ratio F_{sum} / F_{380} .

α can be found by searching for a constant which makes the sum of the measured fluorescence (F_{sum}) independent of $[Ca^{2+}]_i$ (Zhou and Neher, 1993):

$$F_{sum} = F_{350} + \alpha F_{380}.$$

F_{sum} can be used as a substitute for the fluorescence signal recorded at the isobestic point. F_{sum} was calculated from the initial 20 and final 20 images acquired at 350 and 380 nm. Linear interpolation was used to estimate the time course of F_{sum} during single-wavelength imaging.

2.5 Analysis of electrophysiological data

All off-line analysis was done with Igor Pro (WaveMetrics, Lake Oswego, OR, USA). Simulation of Ca^{2+} influx during an action potential was done using an m^2 Hodgkin–Huxley (HH) model (Hodgkin and Huxley, 1952; Borst and Sakmann, 1998b). This approach neglects any functional heterogeneities within the population of VGCCs (Wu et al., 1999; Li et al., 2007). For endbulb terminals, this should however not be a major complication because we found that ~86% of their $I_{Ca(V)}$ is mediated by P/Q-type Ca^{2+} channels (*see below*). Integrals of Ca^{2+} tail currents (500 μ s) after 10 ms step depolarizations were used as a measure for steady-state activation (Augustine et al., 1985; Borst and Sakmann, 1998b). The voltage dependence of the average steady-state

activation parameter m_{∞}^2 was obtained by fitting the normalized integrals with a squared Boltzmann function:

$$(1) \quad m_{\infty}^2 = 1 / (1 + \exp((V_{0.5} - V_m) / \kappa))^2 ,$$

where V_m is membrane potential, $V_{0.5}$ is the half-activation voltage and κ is the steepness factor. The current-voltage (I - V) relation of $I_{Ca(V)}$ elicited by 10 ms steps was fitted with a product of the squared Boltzmann term and a modified form of the constant-field equation, giving the following function:

$$(2) \quad I(V_m) = m_{\infty}^2 P(V_m - V') \times \frac{\exp(-2V' / H)}{1 - \exp(2(V_m - V') / H)} ,$$

where P , H and V' are constants determining current amplitude and rectification (Brown et al., 1983; see also Bischofberger et al., 2002).

For the construction of the HH m^2 model, deactivation of $I_{Ca(V)}$ during steps from 0 mV to voltages between -20 and -70 mV was fitted with single exponentials. The obtained time constants τ_f from exponential fits to the tail currents were then used to approximate the time constants of relaxation (τ_m) of the gate m after a voltage step using the following expression (Hagiwara and Ohmori, 1982; Sala, 1991):

$$(3) \quad \tau_f = \tau_m \times (m_{\infty} + m_0) / (2m_0) .$$

Activation of $I_{Ca(V)}$ was measured during steps from $V_h = -80$ mV to potentials between -10 and +30 mV. The time course of current activation (0–3 ms after pulse onset) was fitted with a squared exponential function with delayed onset:

$$(4) \quad I(t) = I_{\infty} \times (1 - \exp(-(t - t_0) / \tau_m))^2 ,$$

where I_{∞} is steady-state current and t_0 defines current onset.

Rate constants of the HH model α_m and β_m , were then calculated from τ_m and m_∞ according to:

$$(5) \quad \alpha_m = m_\infty / \tau_m, \text{ and}$$

$$(6) \quad \beta_m = (1 - m_\infty) / \tau_m.$$

The dependences of α_m and β_m on V_m were fitted with exponential functions:

$$(7) \quad \alpha_m = \alpha_0 \times \exp(V_m / V_\alpha), \text{ and}$$

$$(8) \quad \beta_m = \beta_0 \times \exp(-V_m / V_\beta),$$

and the calculated rates α_m and β_m were used to estimate m during membrane depolarizations:

$$(9) \quad \frac{\partial m}{\partial t} = \alpha_m \times (1 - m) - \beta_m \times m.$$

The time course of the average activation parameter m was solved numerically using a fifth-order Runge–Kutta–Fehlberg algorithm implemented in Igor Pro and the simulated $I_{Ca(V)}$ was obtained from eqn. (2) using the average parameters $P = 3.4 \mu S$, $H = 12.9 \text{ mV}$ and $V' = 35.9 \text{ mV}$ and $P = 1.6 \mu S$, $H = 19.3 \text{ mV}$ and $V' = 36.0 \text{ mV}$ for endbulb and calyx terminals, respectively.

For non-stationary ensemble fluctuation analysis of $I_{Ca(V)}$, records with identical pulse protocols (20 ms depolarizations to potentials between -19 and -8 mV) were taken every 3–5 s until a run of 20–151 current traces (on average 74 repetitions) was obtained. Next, we derived estimates for variance and mean, point by point, along a trace (Sigworth, 1980). The low-pass filtered ensemble variance $\sigma^2(t)$ of $I_{Ca(V)}$ was calculated from the

$N-I$ difference traces between consecutive responses in order to optimally eliminate trends and drifts (Roberts et al., 1990; Heinemann and Conti, 1992):

$$(10) \quad \sigma^2(t) = \frac{1}{2(N-1)} \sum_{n=1}^{N-1} (\Delta I_n(t))^2$$

where $\Delta I_n(t)$ represent the n^{th} difference trace $\Delta I_n(t) = I_n(t) - I_{n+1}(t)$ after off-line low-pass filtering using a 10-pole Bessel filter with a cut-off frequency $f_c = 2.5$ kHz. The ensemble mean $\bar{I}(t)$ of $I_{\text{Ca(V)}}$ was calculated according to:

$$(11) \quad \bar{I}(t) = \frac{1}{N} \sum_{n=1}^N I_n(t).$$

Only in a few cases the variance-mean relationship showed unambiguous indications of deviation from linearity. Therefore, the single channel current of VGCCs was estimated from the slopes of regression lines fitted to the initial part of the variance-mean plots after subtracting the baseline variance σ_0^2 (see Fig. 3.1.9 for examples). All values are given as mean \pm SEM. Significance of difference was evaluated with the two-tailed Student's unpaired t test. $P < 0.05$ was taken as the level of significance.

Results

3.1 Presynaptic Ca^{2+} influx and vesicle exocytosis at mouse endbulb of Held terminals

3.1.1 Identification of endbulb of Held terminals in acute mouse brainstem slices containing the AVCN

Using high-resolution differential interference contrast optics we were able to visualize and record from bouton-like structures surrounding the SBCs of the AVCN. These structures were identified as endbulb of Held terminals based on four distinct morphological and functional criteria: (I) small size, (Townsend et al.) small whole-cell capacitance, (III) high input resistance, and (IV) the presence of an increase in whole-cell capacitance (ΔC_m) reflecting vesicle exocytosis after eliciting presynaptic Ca^{2+} influx.

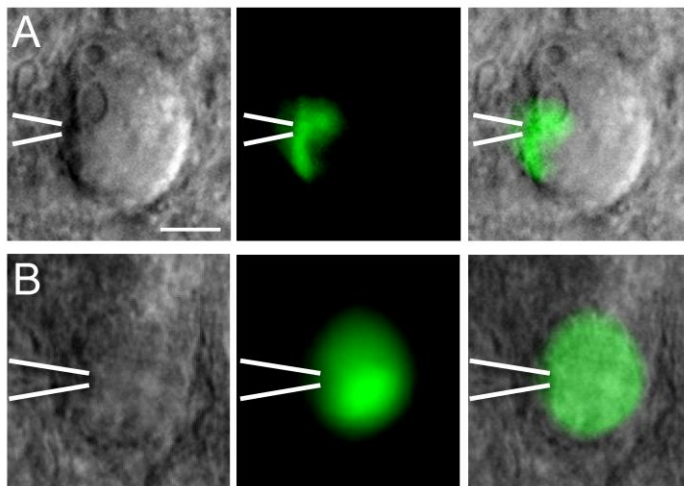


Figure 3.1.1 Identification of endbulb of Held terminals.

A-B, IR-DIC (*left*) and fluorescence (*middle*) images of spherical bushy cells in a brain slice taken after direct presynaptic (**A**) or postsynaptic (**B**) whole-cell recording. The intracellular recording solution contained a fluorescent dye. Overlays of both images are shown in the right column. Presynaptic recording sites were confirmed by exclusion of the fluorescent dye from the postsynaptic neurons. Position of the recording pipette as indicated by the white bars. Calibration bar corresponds to 10 μm .

In a pilot set of experiments, patch-pipettes were filled with an indicator dye to validate our approach for identifying presynaptic recordings. Figure 3.1.1 shows fluorescence images taken after recording from a presynaptic endbulb terminal and a postsynaptic SBC with pipettes containing a fluorescent dye. SBCs were identified by their large spherical

somata with centrally located nuclei and a lack of prominent dendritic arborizations (Brawer et al., 1974; Cant and Morest, 1979; Wu and Oertel, 1984). During presynaptic recordings (Fig. 3.1.1A), the dye labeled terminals, but was clearly excluded from postsynaptic cells. Labeled terminals covered $\leq 25\%$ of the SBC surface and their morphology resembled that of endbulb of Held terminals of young mice or kitten (Brawer and Morest, 1975; Ryugo and Fekete, 1982; Limb and Ryugo, 2000)

Whole-cell membrane capacitance values were estimated from the automatic C_{slow} compensation setting of the EPC-10 amplifier from 54 endbulb terminals and 30 SBCs (Fig. 3.1.2A,B). The mean C_{slow} value was ~ 6 times smaller for presynaptic terminals compared to postsynaptic cells (3.73 ± 0.18 vs. 22.40 ± 1.19 pF, $p < 0.001$, Fig. 3.1.2B) and the distributions of C_{slow} values did not overlap (Fig. 3.1.2A), thus illustrating the clear separation between pre- and postsynaptic recordings. In addition, endbulb terminals had an $\sim 60\%$ higher mean input resistance when compared to SBCs (1.13 ± 0.09 G Ω [$n = 54$] vs. 0.71 ± 0.07 G Ω [$n = 30$], $p < 0.001$, Fig. 3.1.2C).

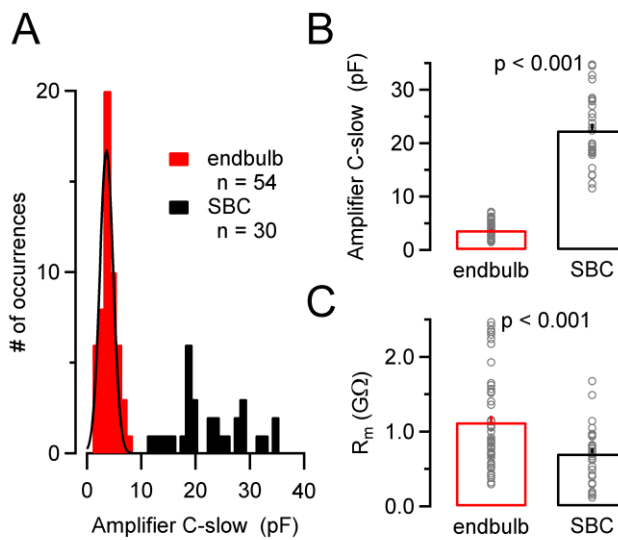


Figure 3.1.2 Passive membrane properties of endbulb terminals and SBCs.

A-C, Pre- and postsynaptic compartments can be easily distinguished by virtue of their divergent passive membrane properties. **A,B,** Frequency distribution (**A**) and means (**B**) of the whole-cell capacitance (reading of the amplifier's C_{slow} cancellation setting) suggest a ~ 6 times smaller surface area for endbulb terminals compared to bushy cells. Note that the two frequency distributions in (**B**) do not overlap. The smooth black curve in (**A**) represents a Gaussian fit with a mean = 3.6 pF and SD = 1.7 pF. **C,** Presynaptic terminals had higher input resistance than postsynaptic SBCs. R_m was determined from the passive current responses elicited by hyperpolarizing voltage steps from $V_h = -80$ to -90 mV.

3.1.2 Passive membrane properties of endbulb and calyx of Held terminals

To compare the passive membrane properties of endbulb and calyx of Held terminals, we analyzed capacitive current transients elicited by small hyperpolarizing voltage steps from $V_h = -80$ mV to -90 mV. To facilitate identification of presynaptic recordings, experiments were done under conditions that pharmacologically isolated voltage-gated Ca^{2+} currents and allowed time-resolved presynaptic capacitance measurements. Figure 3.1.3 A illustrates $I_{\text{Ca}(V)}$ and the associated ΔC_m recorded from an endbulb and a calyx terminal. Passive current transients are shown in the bottom panels. The total capacitance of the entire presynaptic compartment (C_{total}) calculated from the current integrals was ~ 3 times smaller for endbulb compared to calyx terminals (13.0 ± 0.9 [n = 54] vs. 37.9 ± 1.8 pF [n = 46], $p < 0.001$). Passive current transients generally decayed bi-exponentially following voltage steps. The amplitude of the slowly decaying component was highly variable and most likely represented the slow charging of the membrane of the presynaptic axon of variable length (Borst and Sakmann, 1998b).

To estimate the surface area of the terminals, we fitted the passive capacitive current transients with bi-exponential functions and calculated the time integrals of the fast and slowly decaying current components presumably reflecting the membrane capacitance of the terminal (C_{terminal}) and that of the attached axon (C_{axon}), respectively (Fig. 3.1.3B–D). On average, the capacitance of endbulb terminals was ~ 4 times smaller than that of calyces (Table 1) and little overlap between the two populations of C_m estimates was observed (Fig. 3.1.3C). In addition, C_{terminal} estimates for endbulb terminals showed a significantly higher variability as indicated by their larger coefficient of variation (CV = 0.33 vs. 0.22, $p < 0.05$ by bootstrap analysis), suggesting a more variable size of endbulbs

compared with calyx terminals. Interestingly, the estimated surface area of the presynaptic axons (C_{axon}) was also smaller for endbulbs compared to calyx terminals (8.6 ± 0.8 pF [n=54] vs. 20.6 ± 1.7 pF [n=46], $p < 0.001$, Fig. 3.1.3D). This is consistent with the idea that coronal slices may preserve a larger portion of the presynaptic axon for calyx synapses. The input resistance of both types of presynaptic terminals was very high (on average >1 G Ω , Fig. 3.1.3E, Table 1).

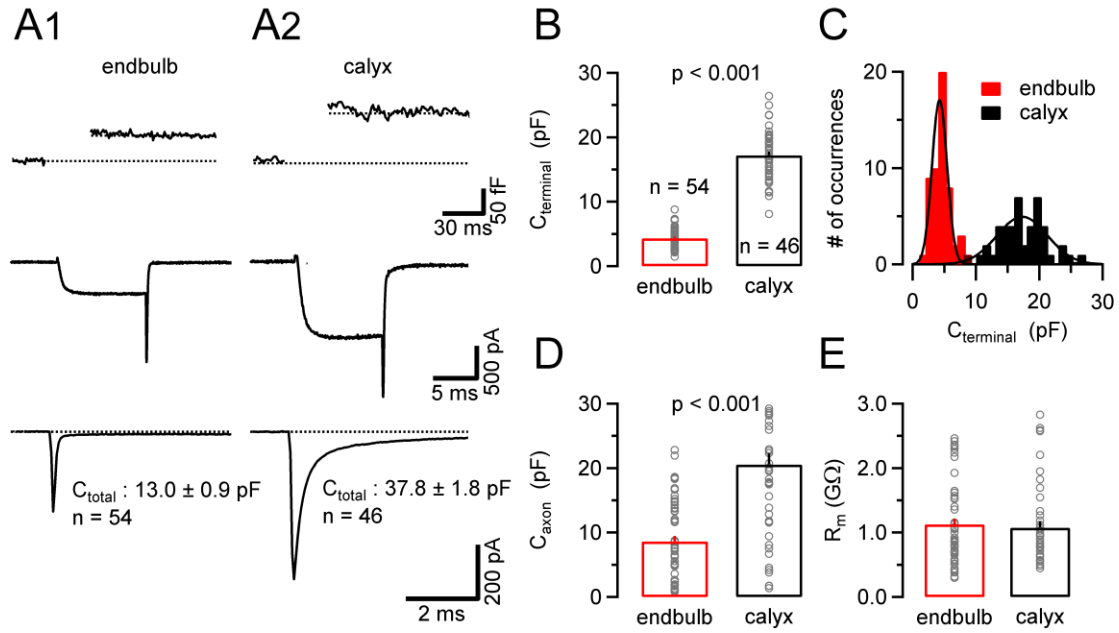


Figure 3.1.3 Comparison of passive membrane properties between endbulb and calyx terminals.

A, Changes in membrane capacitance (ΔC_m , *top panel*) elicited by step-depolarizations (10 ms, from $V_h = -80$ to 0 mV). The corresponding $I_{\text{Ca(V)}}$ are shown in the *middle panel*. The total resting membrane capacitance of the terminals (C_{total}) was estimated from integrals of passive current transients elicited by hyperpolarizing steps to -90 mV (*bottom*) recorded in whole-cell voltage-clamp after compensating the pipette's capacitance in cell-attached mode. C_{total} was on average ~ 3 times smaller for endbulb terminals. Capacitive current transients of most terminals decayed double exponentially suggesting a variable contribution of the attached axon to the total membrane capacitance. **B-D**, To distinguish the whole-cell capacitance of the terminals (C_{terminal} , **B,C**) from that of the attached axons (C_{axon} , **D**) we separated the capacitive current transients into fast and slowly decaying components. On average, endbulb terminals had a ~ 4 times smaller C_{terminal} (**B**) with a larger coefficient of variation (**C**) suggesting more variable size of these terminals. The smooth black curves in (**C**) represent Gaussian fits with means of 4.25 pF vs. 17.3 pF and SDs of 1.68 pF vs. 5.63 pF for endbulb and calyces, respectively. **E**, Input resistance was on average ≥ 1 M Ω for both endbulb and calyx terminals.

3.1.3 Properties of voltage-gated Ca^{2+} currents at endbulb and calyx terminals

The expression of VGCC subtypes at presynaptic terminals varies between different types of synapses (Luebke et al., 1993; Takahashi and Momiyama, 1993; Li et al., 2007). In addition, the expression of VGCC subtypes may be developmentally regulated: for example young calyces of Held express a mixture of P/Q-, N- and R-type VGCCs whereas mature terminals express nearly exclusively P/Q-type VGCCs (Iwasaki and Takahashi, 1998; Iwasaki et al., 2000). Application of the P/Q-type channel blocker ω -AgaTX reduced evoked EPSCs to <20% at P11–16 endbulb synapses suggesting that glutamate release is predominantly governed by P/Q-types already at this age (Oleskevich and Walmsley, 2002). To directly quantify the fractional expression of P/Q-type VGCCs in endbulbs, we measured the block by ω -AgaTX of pharmacologically isolated presynaptic $I_{\text{Ca(V)}}$ in endbulb synapses (Fig. 3.1.4A,B). Application of a saturating concentration of ω -AgaTX (200 nM) blocked ~86% of $I_{\text{Ca(V)}}$. Only a minor fraction of $I_{\text{Ca(V)}}$ was insensitive to ω -AgaTX ($13.8 \pm 2.8\%$, $n=3$).

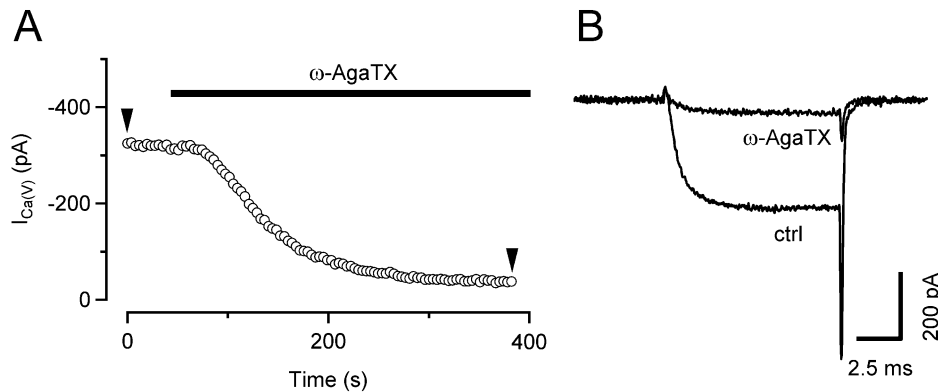


Figure 3.1.4 Pharmacological dissection of Ca^{2+} currents in endbulb terminals.

A-B, P/Q-type VGCC account for ~86% of $I_{\text{Ca(V)}}$ in endbulb terminals. $I_{\text{Ca(V)}}$ was elicited every 3.9 s by depolarizing voltage steps (10 ms, from $V_h = -80$ to 0 mV) while ω -AgaTX (200 nM) was applied to the external solution as indicated by the bar. Time course of block (**A**) and individual sweeps (**B**) representing the amplitude values at arrow heads.

To study voltage dependence of $I_{\text{Ca(V)}}$ in endbulb and calyx terminals, V_m was stepped from -80 mV to various potentials (10 ms duration, Fig. 3.1.5A). I - V relationships of $I_{\text{Ca(V)}}$ are illustrated in Fig. 3.1.5B for both terminals. The threshold for activation of $I_{\text{Ca(V)}}$ was around -40 mV, the I - V curves peaked between -10 and ± 0 mV. The smooth curves in Fig. 3.1.5B represent fits to the I - V relationships using a modified form of the constant field equation (eqn. (2), Brown et al., 1983; see also Bischofberger et al., 2002). Parameters from the fit were $P = 3.4$ μS , $H = 12.9$ mV and $V' = 35.9$ mV versus $P = 1.6$ μS , $H = 19.3$ mV and $V' = 36.0$ mV for endbulb and calyx terminals, respectively (Fig. 3.1.5B).

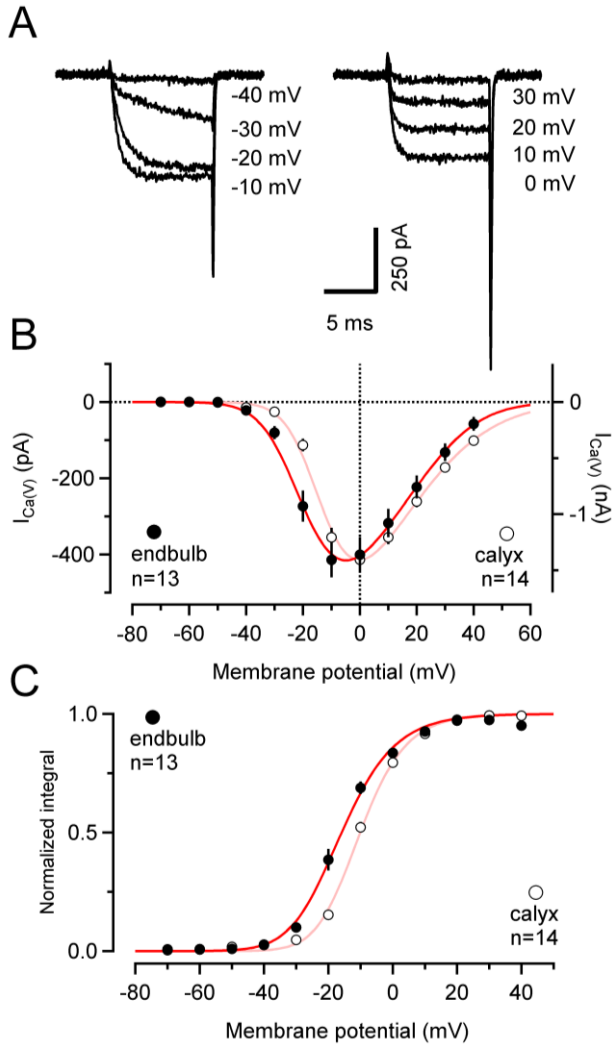


Figure 3.1.5 Properties of voltage-gated Ca^{2+} currents in endbulb terminals.

A, Current-voltage relationship of $I_{\text{Ca(V)}}$ in endbulb and calyx terminals. $I_{\text{Ca(V)}}$ was elicited by step depolarizations (10 ms duration) from $V_h = -80$ mV to the potentials indicated next to each trace and recorded in an endbulb terminal. **B**, I - V curves obtained from peak amplitudes of $I_{\text{Ca(V)}}$ from 13 endbulb (black) and 14 calyx (gray) terminals. The smooth red curves represent fits to the data points using a modified form of the constant-field equation (see Methods eqn. (2)). **C**, Normalized tail current integrals of 10 ms step depolarizations plotted as a function of V_m to estimate the steady-state activation parameter m_∞^2 . The smooth red curves represents fits to the data points using a squared Boltzman function with half-activation voltages $V_{0.5} = -24.4$ mV (endbulb) and -17.4 mV (calyx) and steepness factors $\kappa = 9.63$ mV (endbulb) and 8.23 mV (calyx).

In endbulb terminals, $I_{\text{Ca(V)}}$ started to activate at slightly more negative V_m values. This is also reflected in a slight left shift of the corresponding steady-state activation curve obtained from the normalized integrals of Ca^{2+} tail currents (Fig. 3.1.5C). The voltage dependence of the steady-state activation parameter (m_∞^2) of calcium channels was fitted with a squared Boltzman function (eqn. (1)). Midpoint potentials of the steady-state activation curves (V_h) were -24.4 mV vs. -17.4 mV, and the slope factors of the activation curve (κ) were 9.63 mV versus 8.23 mV for endbulb and calyx terminals, respectively (Fig. 3.1.5C).

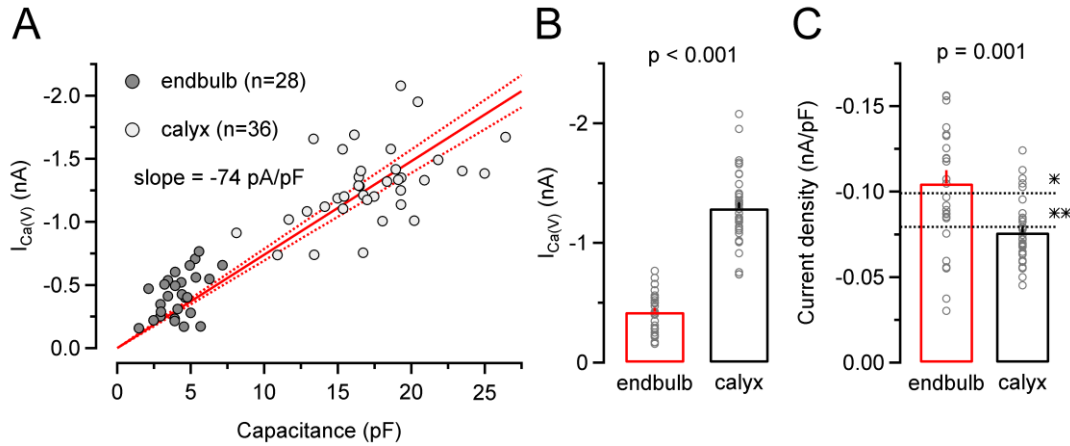


Figure 3.1.6 Ca^{2+} current densities are slightly larger in endbulb versus calyx terminals.

A, Scatter plot of $I_{\text{Ca(V)}}$ versus terminal capacitance obtained from 28 endbulb and 36 calyx terminals. $I_{\text{Ca(V)}}$ was elicited by step depolarizations to $V_h = 0$ mV. Solid and dotted red lines represent linear regression and 95% confidence intervals for the entire data set, respectively. The slope of the regression line was -74 pA/pF. **B,C**, Average amplitudes (**B**) and current densities (**C**) of $I_{\text{Ca(V)}}$ in endbulb and calyx terminals. For comparison, current densities for rat calyces (Borst and Sakmann, 1998a) (*) and rat hippocampal mossy fiber terminal (Bischofberger et al., 2002) (**) are indicated by the dotted lines.

To study current density of $I_{\text{Ca(V)}}$ in both types of presynaptic terminals, peak amplitudes of $I_{\text{Ca(V)}}$ were plotted versus terminal capacitance (Fig 3.1.6A). Linear regression analysis indicated that the amplitude of $I_{\text{Ca(V)}}$ increased by ~ 74 pA per pF membrane capacitance. On average, peak amplitudes of $I_{\text{Ca(V)}}$ were ~ 3 times smaller in endbulbs compared to calyces (Fig. 3.1.6B) which is consistent with the much smaller size of the former

terminals (see Fig. 3.1.3B,C, Table 1). Interestingly, mean Ca^{2+} current densities were slightly larger in endbulbs (Fig. 3.1.6C). In both cases, Ca^{2+} current densities were comparable to previously reported values for calyces in P8–10 rats (Borst and Sakmann, 1998b) or rat hippocampal mossy fiber terminal (Bischofberger et al., 2002).

3.1.4 Establishing an HH-type m^2 model of $I_{Ca(V)}$ in endbulb terminals

We next studied activation and deactivation kinetics of $I_{Ca(V)}$ with the aim of establishing a simple HH-type m^2 model to simulate Ca^{2+} influx during presynaptic AP activity. Rapid voltage clamp is critical for determining the gating kinetics of VGCCs. Voltage-clamp speed is limited by the kinetics of the charging of the terminal, which occurs with a time constant $\tau = R_s \times C_{terminal}$, where R_s is the uncompensated series resistance and $C_{terminal}$ is the terminal capacitance. Mean time constants were 34 μs and 88 μs for endbulb and calyx recordings, respectively. Figure 3.1.7A1 illustrates a family of $I_{Ca(V)}$ elicited by 10 ms voltage steps to V_m between -10 and $+30$ mV. $I_{Ca(V)}$ activated very rapidly with time constants <1 ms when fitted with single exponentials. Average activation time constants (τ_A) were 0.84, 0.60, 0.45, 0.33 and 0.32 ms for steps to -10 , ± 0 , 10, 20 and 30 mV, respectively ($n = 10$). The activation time constants of the m gate (τ_m) were obtained from fitting the current onset with eqn. (4). Deactivation of $I_{Ca(V)}$ was studied by analyzing Ca^{2+} tail currents elicited by 10 ms depolarizations to 0 mV followed by steps to V_m between -20 and -70 mV (Fig. 3.1.7A2). Some experiments in which $I_{Ca(V)}$ was followed by slow tail currents, possibly reflecting axonal Ca^{2+} conductances (Borst and Sakmann, 1998b), were excluded from the analysis. Decay time constants derived from single exponential fits to Ca^{2+} tail currents (τ_D) were 0.10, 0.13, 0.18, 0.26, 0.39 and 0.51 ms in endbulb ($n = 10$) vs. 0.12, 0.14, 0.17, 0.24, 0.40, and 0.63 ms in calyx terminals ($n = 12$).

for steps to -70 , -60 , -50 , -40 , -30 and -20 mV, respectively. The deactivation time constants τ_m were estimated from τ_D according to eqn. (3) and plotted together with those derived from activation of $I_{Ca(V)}$ (Fig. 3.1.7B). The bell-shaped dependence of τ_m on membrane potential is expected for a voltage-gated channel. The corresponding opening (α_m) and closing (β_m) rates were then calculated from the steady-state activation parameter m_∞^2 and τ_m , and their voltage dependence was fitted with single exponential functions (Fig. 3.1.7C). Table 2 summarizes model parameters for presynaptic $I_{Ca(V)}$ in mouse endbulb and calyx terminals.

To validate our HH-type m^2 model for endbulb VGCCs, we compared the experimentally recorded $I_{Ca(V)}$ elicited by a 1ms depolarization to 0 mV with the predicted one (Fig. 3.1.7D). The simulated voltage step was low-pass filtered with a single-pole filter having a relaxation time constant as predicted by the measured values for membrane capacitance and series resistance (Fig. 3.1.7D *top panel*). The time course of the activation parameter m^2 is shown in the middle panel. Its peak value was ~ 0.71 . Except for the absence of the small outward transient at current onset, possibly reflecting a gating current, and a small deviation at the end of the deactivation time course, the simulated $I_{Ca(V)}$ (*red trace*) closely matched the measured one (*bottom panel*).

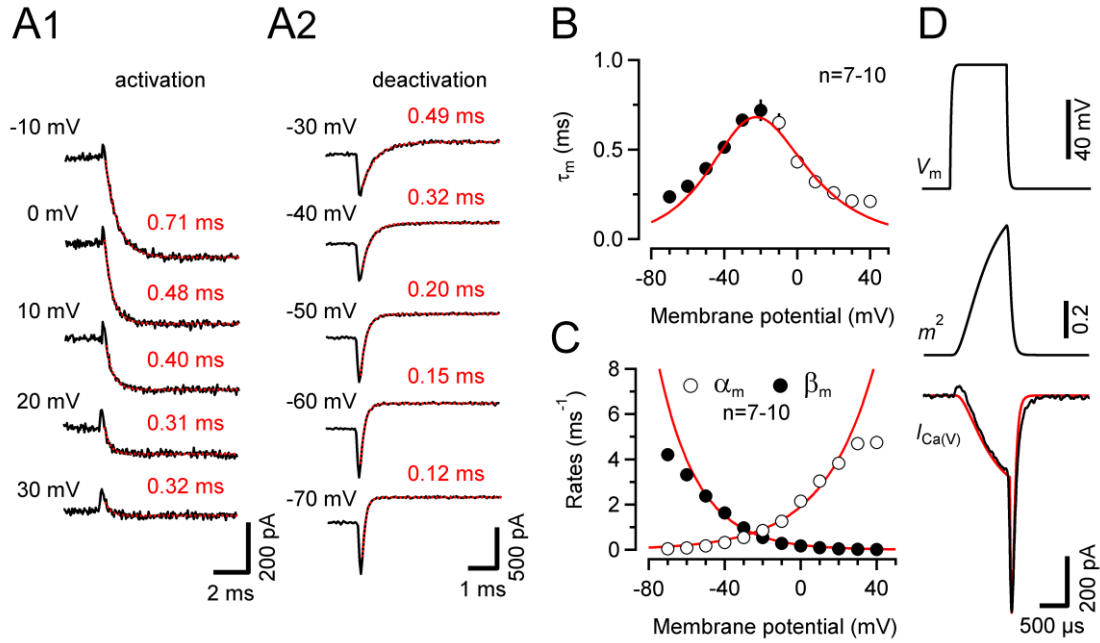


Figure 3.1.7 Hodgkin-Huxley model of Ca^{2+} influx in endbulb terminals.

A, Rapid activation (**A1**) and deactivation (**A2**) kinetics of $I_{\text{Ca(V)}}$. Smooth red curves represent single exponential fits. **A1**, Activation of $I_{\text{Ca(V)}}$ elicited by depolarizing voltage steps from $V_h = -80$ mV to various V_m values ($\tau_A = 0.71, 0.46, 0.40, 0.31$ and 0.32 ms for steps to $-10, 0, 10, 20$ and 30 mV, respectively). **A2**, Deactivation of $I_{\text{Ca(V)}}$ after a 10 ms depolarization to 0 mV after stepping back to various V_m values ($\tau_D = 0.49, 0.32, 0.20, 0.15$ and 0.12 ms for steps to $-30, -40, -50, -60$ and -70 mV, respectively). **B**, Time constants τ_m measured from deactivation (-70 to -20 mV, eqn.3) or activation (-10 to 40 mV, eqn.4) of $I_{\text{Ca(V)}}$. The smooth line represents the time constants predicted from the rate constants of the HH-model ($\tau_m = 1/(\alpha_m + \beta_m)$). **C**, Activation (α_m) and deactivation (β_m) rates of the gate m plotted as a function of V_m . Continuous lines are single exponential fits (eqns. (7) and (8)), with $\alpha_0 = 2.03 \text{ ms}^{-1}$, $V_\alpha = 26.5$ mV and $\beta_0 = 0.22 \text{ ms}^{-1}$, $V_\beta = 19.8$ mV. Potentials >20 and <-60 mV were excluded from the fit. **D**, Comparison of measured and simulated $I_{\text{Ca(V)}}$ elicited by a 1 ms depolarization to 0 mV. The assumed time course of V_m (top panel) was obtained by digitally filtering a 1 ms step with a single-pole filter (time constant $\tau = R_s \times C_m$, where R_s and C_m represent uncompensated series resistance and whole-cell capacitance, respectively). The activation parameter m^2 peaked at ~ 0.71 (middle panel). Except for a small deviation at the end of the deactivation time course, the simulated $I_{\text{Ca(V)}}$ (red trace) closely matched the measured current (black trace, bottom panel).

3.1.5 Simulating Ca^{2+} influx following presynaptic APs

The presynaptic AP waveform is a key parameter for determining presynaptic Ca^{2+} influx and thereby vesicles release (Llinas et al., 1982; Augustine, 1990; Sabatini and Regehr, 1997; Borst and Sakmann, 1999b). Presynaptic APs in calyx terminals are very fast (Barnes-Davies and Forsythe, 1995; Borst et al., 1995) and their time course is further accelerated during synapse maturation (Taschenberger and von Gersdorff, 2000). In order

to determine the presynaptic AP waveform in endbulb terminals we used two approaches. Firstly, we depolarized the terminals under current-clamp by injecting sustained or pulse-like depolarizing currents. Secondly, we stimulated the afferent fibers and recorded the shape of the invading presynaptic AP.

Figure 3.1.8 compares changes in membrane voltage in response to injection of sustained hyper- or depolarizing currents (Fig. 3.1.8A1), pulse-like depolarizing currents (Fig. 3.1.8A2) or a train of afferent-fiber stimuli (Fig. 3.1.8A3). For comparison, the waveforms of the first AP in the trains are shown at a faster time scale in Fig. 3.1.8B1. In response to sustained depolarizing currents, endbulb terminals generally generated only a single APs (two APs in 1 out of 14 terminals tested), similar as reported for P13–15 rat calyces (Nakamura and Takahashi, 2007). As expected from a synapse that is able to transmit at high frequency (Joris et al., 1994), endbulb terminals fired reliably at high frequency when stimulated with either trains of pulse-like depolarizations or by trains of afferent fiber stimuli. AP peak amplitudes were similar when evoked by either current injection or afferent fiber stimulation (121.4 ± 2.7 mV [$n = 10$] versus 122.0 ± 5.1 mV [$n = 5$], $p = 0.92$) (Fig. 3.1.8C). Surprisingly, the duration of endbulb APs was ~65% longer when elicited by current injection (432.5 ± 29.2 μs [$n = 10$] vs. 262.8 ± 14.7 μs [$n = 5$], $p < 0.001$) (Fig. 3.1.8B,C). We therefore decided to use AP waveforms recorded after fiber stimulation exclusively in the simulation described below.

In order to estimate $I_{\text{Ca(V)}}$ during single presynaptic APs at endbulb terminals, we used the recorded AP waveforms to drive the HH-type m^2 model of $I_{\text{Ca(V)}}$ described above. The estimate of endbulb AP-driven Ca^{2+} influx was then compared to that in calyx terminals.

Typical presynaptic APs from an endbulb and a calyx are shown superimposed in Fig. 3.1.8E. Presynaptic APs of both auditory terminals are much briefer than those recorded in hippocampal mossy-fiber boutons (half-width 852 μs at RT, Bischofberger et al., 2002).

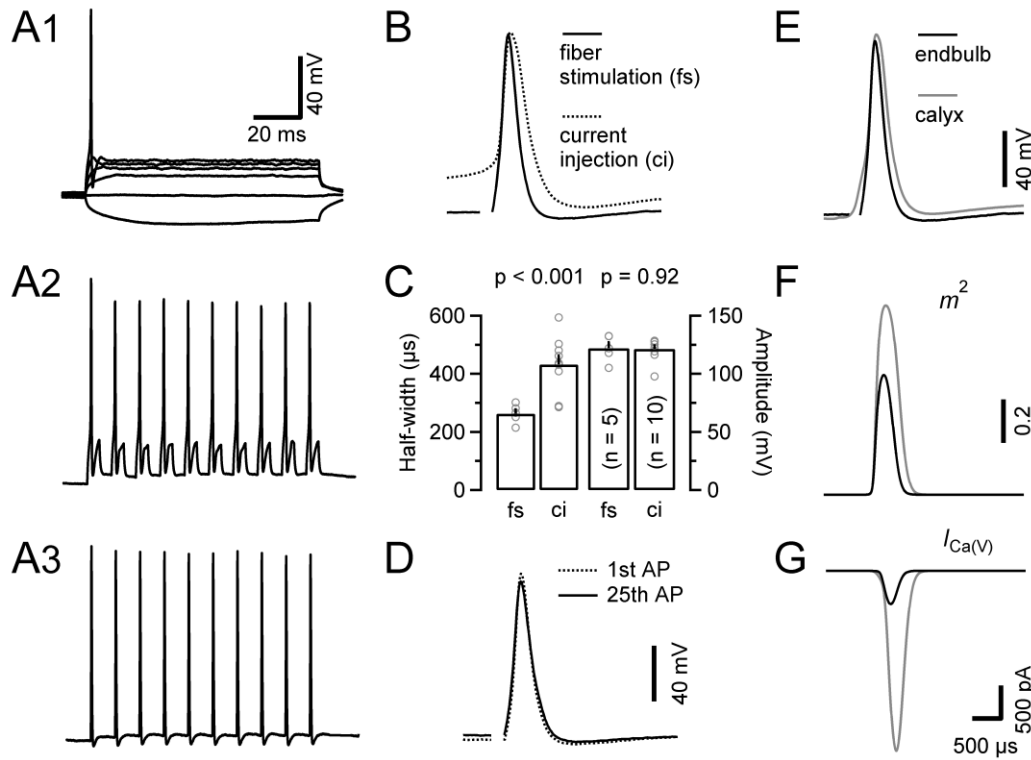


Figure 3.1.8 Ca^{2+} influx during a single presynaptic action potential is significantly less at endbulb versus calyx terminals.

A, Presynaptic membrane potential responses to either sustained (**A1**, 100 ms duration, -30 to 120 pA) or pulse-like (**A2**, 1 ms duration, 180 pA) current injections recorded in current-clamp configuration. **B**, Comparison of presynaptic APs elicited by current injection of afferent fiber stimulation. Initial APs from the trains illustrated in **A2** and **A3** shown superimposed. **C**, Presynaptic APs elicited by afferent fiber stimulation had shorter half-widths (*left*) but similar peak amplitudes (*right*) when compared with those elicited by depolarizing current injections. **D**, First and last APs elicited by a 100Hz train consisting of 25 stimuli are shown superimposed to illustrate stability of AP waveform during high-frequency stimulation. **E-G**, Comparison of simulated $I_{\text{Ca(V)}}$ during presynaptic endbulb and calyx APs. **E**, Endbulb APs (*black*) were slightly smaller in amplitude and shorter in duration compared to those recorded from calyces (*gray*). **F**, Simulated time course of the activation parameter m^2 . Because of its larger amplitude and longer duration, the calyceal AP waveform opened presynaptic VGCC more efficiently than the endbulb AP. **G**, Simulated $I_{\text{Ca(V)}}$ during presynaptic APs in endbulb (*black*) and calyx (*gray*) AP. On average, the simulated presynaptic $I_{\text{Ca(V)}}$ was ~6 times smaller for endbulb terminals compared to the simulated current for calyx terminals.

On average, the duration of endbulb APs was ~26% shorter compared to calyx APs, and their peak amplitude was ~7% lower (Table 1). This suggests that endbulb APs may open presynaptic VGCC less effectively than calyx APs recorded at the same age. Fig. 3.1.8F shows that this is indeed the case: the average peak value of m^2 was substantially lower in endbulb compared to calyx terminals (Table 2). Taken together, our simulations estimate that AP-driven Ca^{2+} influx is greatly reduced (~6 times less) in endbulb compared to calyx terminals. In addition, the half-width of $I_{\text{Ca(V)}}$ during presynaptic APs was ~13% shorter in endbulb compared to calyx terminals (Fig. 3.1.8G, Table 1). Peak amplitudes and charge of the simulated $I_{\text{Ca(V)}}$ during presynaptic APs reported here for the P9–P11 mouse calyx of Held are slightly smaller than the values previously reported for P8–P10 rat calyces of Held (Borst and Sakmann, 1998b)

3.1.6 Estimating the total number of VGCC expressed at endbulb and calyx terminals

Estimating the total number of VGCC expressed at endbulb and calyx synapses requires knowledge about their unitary current amplitude (i) and open probability (p_o). We therefore set out to obtain estimates of i from non-stationary fluctuation analysis of presynaptic $I_{\text{Ca(V)}}$ (Sigworth, 1980; Brandt et al., 2005; Li et al., 2007). To facilitate the analysis of current fluctuations around mean currents of variable amplitudes, we elicited $I_{\text{Ca(V)}}$ by 20 ms steps to relatively low V_m values (–19 to –8 mV) which resulted in relatively slowly activating currents. Such stimuli also avoided the contamination of the rising phase of $I_{\text{Ca(V)}}$ with outward ‘asymmetry’ currents that were reported earlier by Borst and Sakmann (1998b) and generally seen at current onset. Sets of 20–151 (on average 74) identical, 20 ms depolarizations were applied. Families of successively

recorded $I_{Ca(V)}$ are shown in Fig. 3.1.9 for an endbulb (Fig. 3.1.9A) and a calyx (Fig. 3.1.9 A,B) terminal.

The rising phase of the Ca^{2+} currents was associated with a marked variance increase. Variance-mean plots are shown in the bottom panels of Fig. 3.1.9A–C. Using line fits to the initial portion of these plots, we thus estimated the unitary current amplitude i to be -0.117 pA and -0.130 pA for the two terminals illustrated in Fig. 3.1.9. To verify that the observed increase in variance originated from stochastic gating of VGCCs, we repeated the experiments in the presence of elevated external Ca^{2+} (6 mM). Under these conditions, i increased (-0.309 pA for the terminal illustrated in Fig. 3.1.9C) which is expected from the substantial increase in Ca^{2+} flux at this concentration (Schneggenburger et al., 1999, their Fig. 2). An expression relating i to the expected unitary current amplitude at $V_m = 0$ mV ($i(0)$) can be obtained from eqn. (2):

$$(12) \quad \frac{i}{i(0)} = \frac{(V_m - V') \times (\exp(2V' / H) - 1)}{V' \times (\exp(2V_m / H) - \exp(2V' / H))}.$$

Average values for $i(0)$ were similar for endbulb and calyx terminals (Fig. 3.1.9D , Table 1), but smaller than those previously estimated for hippocampal mossy fiber boutons (Li et al., 2007). Using these unitary current amplitudes, we estimate that an average number of 5500 versus 16400 VGCCs open at the peak of 0 mV depolarizations in endbulb and calyx terminals, respectively. We estimate an average total number of 6400 channels (endbulb) versus 20400 channels (calyx) are expressed in these presynaptic terminals, assuming that the macroscopic steady state activation parameter m^2 (Fig. 3.1.5B3) reflects the microscopic channel open probability (endbulb $m^2(0) = 0.86$, calyx $m^2(0) = 0.80$).

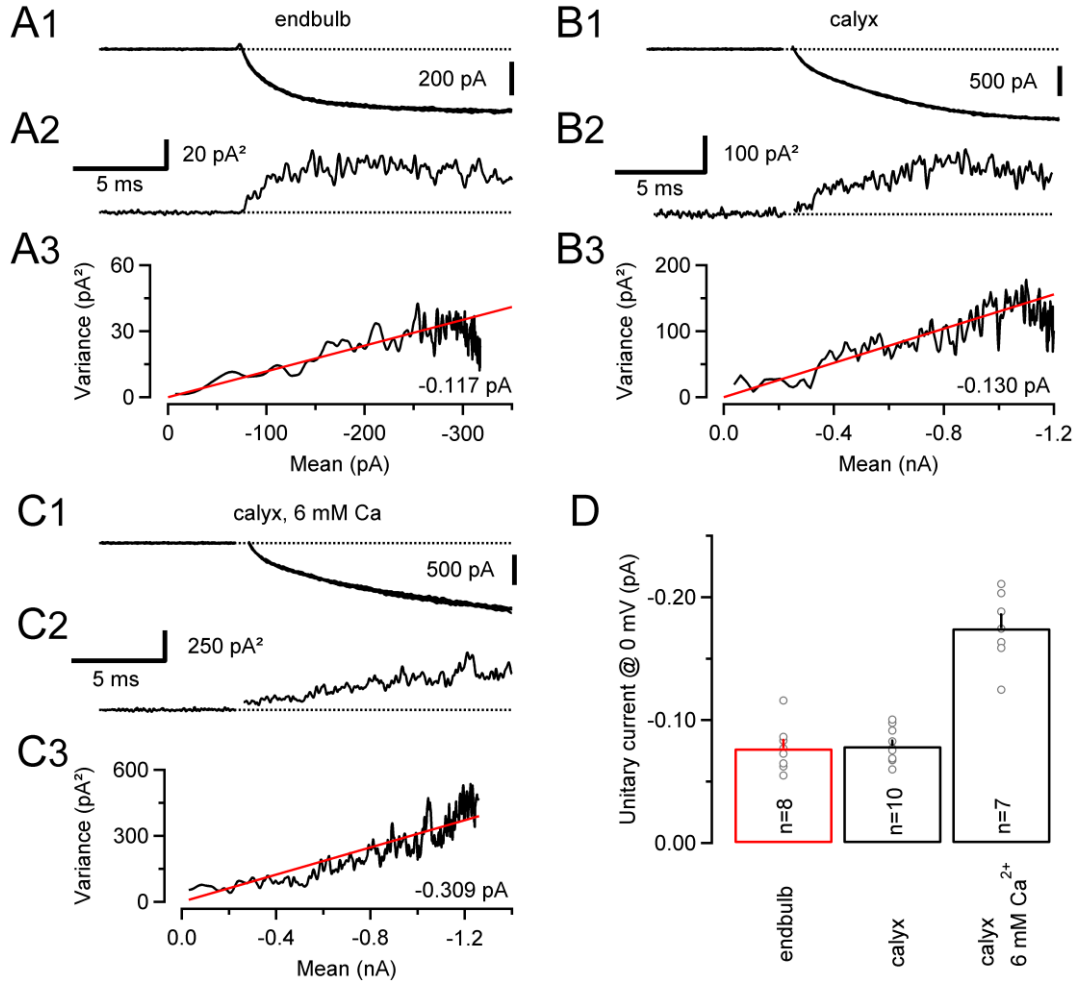


Figure 3.1.9 Single channel current of VGCC expressed in endbulb and calyx terminals.

Ensemble variance-mean analysis of $I_{Ca(V)}$ recorded from an endbulb (**A**, $V_m = -13$ mV, 74 repetitions) and two calyx synapses at 2 mM (**B**, $V_m = -15$ mV, 65 repetitions) and 6 mM (**C**, $V_m = -10$ mV, 65 repetitions) external Ca^{2+} . Seven consecutive sweeps are shown superimposed in the top row (**A1**, **B1**, **C1**). The corresponding variance traces are shown below (**A2**, **B2**, **C2**). Variance was estimated from difference traces (eqn. (10)) to optimally eliminate trends and drifts, and background variance was subtracted. **A3**, **B3**, **C3**, Variance mean plots for the same terminals. Red lines represent linear fits to the initial slope after the variance was corrected for the contribution from the background. The estimated unitary currents i were -0.117 pA, -0.130 pA and -0.308 pA for the endbulb, respectively. **D**, Summary data obtained from 8 endbulbs and 10 calyces. The expected unitary current amplitudes at $V_m = 0$ mV ($i(0)$) were calculated according to eqn. (12). For comparison, the estimated $i(0)$ at elevated external Ca^{2+} (6 mM) is shown.

3.1.7 $I_{Ca(V)}$ inactivation and facilitation in endbulb and calyx terminals

During sustained membrane depolarizations or high-frequency trains of short, AP-like depolarizations, the presynaptic $I_{Ca(V)}$ in calyx terminals shows prominent current inactivation (Forsythe et al., 1998). Since transmitter release is highly nonlinearly related

to calcium influx (Neher, 1998), even minute changes in presynaptic Ca^{2+} flux can strongly modulate vesicle release. Indeed, inactivation of $I_{Ca(V)}$ during repetitive presynaptic AP firing has been suggested to account for a sizable fraction of synaptic depression at the calyx of Held (Xu and Wu, 2005; but see Nakamura et al., 2008). In Fig. 3.1.10A, $I_{Ca(V)}$ inactivation during 100 ms depolarizations to 0 mV is compared between endbulb and a calyx terminals. Significantly less inactivation of $I_{Ca(V)}$ was observed in the endbulb terminals (Fig. 3.1.10A2, Table 1). Since $I_{Ca(V)}$ inactivation is at least partially Ca^{2+} -dependent, we quantified $I_{Ca(V)}$ inactivation in the presence of a high intracellular concentration of the Ca^{2+} chelator BAPTA. Interestingly, $I_{Ca(V)}$ inactivation was further reduced under these condition in endbulb terminals but nearly unaffected in calyx terminals (Fig. 3.1.10B).

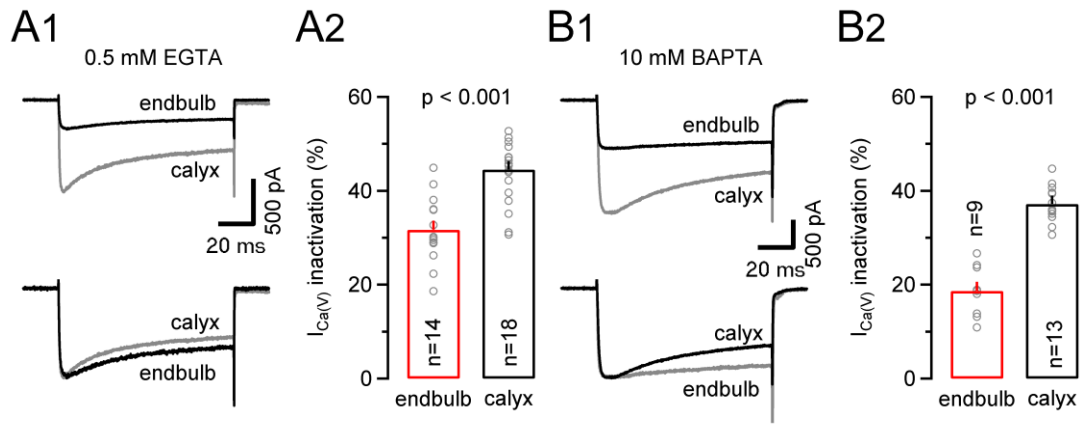


Figure 3.1.10 Inactivation of presynaptic $I_{Ca(V)}$ during sustained depolarizations is significantly less at endbulb versus calyx terminals.

A1, Representative recordings of $I_{Ca(V)}$ (100 ms depolarization to 0 mV) from an endbulb (black) and a calyx (gray) terminal (top panel) recorded with a pipette solution containing 0.5 mM EGTA. Both currents were normalized with respect to their peak amplitudes for comparison (bottom panel). **A2**, Comparison of fractional inactivation ($(I_{peak} - I_{100 ms}) / I_{peak} \times 100\%$) in endbulb and calyx terminals. On average, $I_{Ca(V)}$ showed less inactivation in endbulb terminals versus calyx terminals. **B1**, Similar recordings as illustrated in **A1**, but with 10 mM BAPTA in the internal recording solution. **B2**, Under these recording conditions, the amount of $I_{Ca(V)}$ inactivation was only slightly attenuated in calyx terminals but profoundly reduced in endbulbs.

To investigate if $I_{Ca(V)}$ inactivation during presynaptic AP activity varies with auditory nerve firing frequency, we delivered trains consisting of 25 AP-like depolarizations (1 ms from $V_h = -80$ to 0 mV, Fig. 3.1.11) at various frequencies. Figure 3.1.11A illustrates the resulting $I_{Ca(V)}$ trains recorded in an endbulb (Fig. 3.1.11A1) and a calyx (Fig. 3.1.11A2) elicited at a frequency of 200 Hz (Fig. 3.1.11A left panels). During the first 2-3 stimuli, $I_{Ca(V)}$ facilitated (Borst and Sakmann, 1998a; Cuttle et al., 1998). Its peak amplitude remained stable thereafter in the endbulb but decreased in the calyx terminal. First and last $I_{Ca(V)}$ of the 200 Hz trains are shown superimposed for comparison (Fig. 3.1.11A middle panels). In contrast, during 10 Hz stimulation, $I_{Ca(V)}$ remained stable throughout the train in the endbulb but inactivated in the calyx (Fig. 3.1.11A right panels).

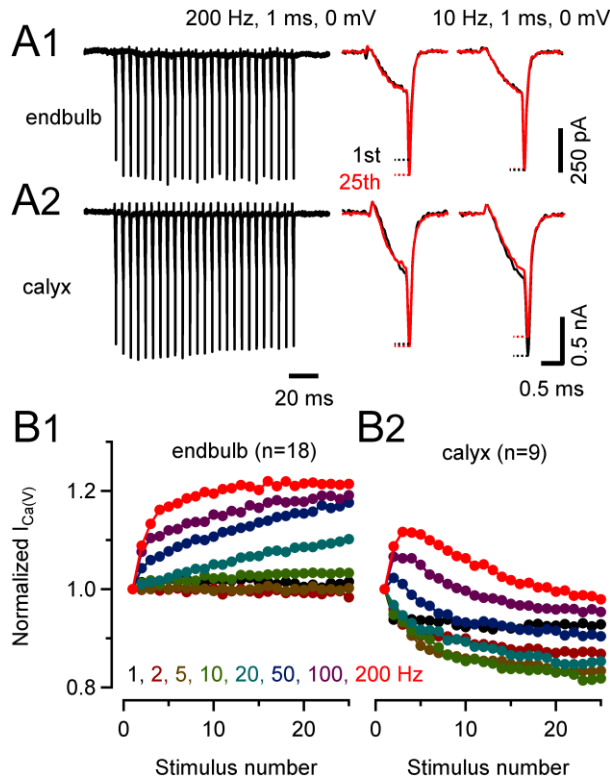


Figure 3.11 Presynaptic $I_{Ca(V)}$ at endbulb terminals facilitates and does not inactivate during trains of AP-like depolarizations.

A, Representative 200 Hz trains of $I_{Ca(V)}$ elicited by brief depolarizations (1 ms, 0 mV) recorded with a pipette solution containing 0.5 mM EGTA from an endbulb (**A1**) and a calyx (**A2**) terminal (*left panel*). Initial and final $I_{Ca(V)}$ are shown superimposed for comparison (*middle panel*). Facilitation of $I_{Ca(V)}$ was observed during train stimulation of endbulb terminal. In calyx terminals, $I_{Ca(V)}$ inactivated after initial facilitation. Low frequency stimulation (10 Hz) induced inactivation of $I_{Ca(V)}$ in calyx but not in endbulb terminals (*right panel*). **B**, Facilitation and inactivation of presynaptic $I_{Ca(V)}$ during train stimulation at frequencies ranging from 1 to 200 Hz. Summary results from 18 endbulb (**B1**) and 9 calyx terminals (**B2**).

Summary results for various train frequencies ranging from 1 to 200 Hz are compared in Fig. 3.1.11B. $I_{Ca(V)}$ inactivation was completely absent from endbulb terminals for all

frequencies tested (Fig. 3.1.11B1). $I_{\text{Ca(V)}}$ facilitation was observed for frequencies ≥ 20 Hz and peaked at a level of $\sim 20\%$. Calyces of Held, on the other hand, showed robust $I_{\text{Ca(V)}}$ inactivation during low-frequency stimulation (≤ 10 Hz). For frequencies ≥ 20 Hz, calyceal $I_{\text{Ca(V)}}$ showed net facilitation during the onset of the stimulus train whereas $I_{\text{Ca(V)}}$ inactivation dominated the remainder of the train (Fig. 3.1.11B2).

3.1.8 Ca^{2+} -dependent vesicle exocytosis assayed by ΔC_m measurements in endbulb and calyx terminals

We used capacitance measurements to quantify and compare Ca^{2+} -dependent vesicle release in endbulb and calyx terminals (Sun and Wu, 2001; Taschenberger et al., 2002). Figure 3.1.12A shows families of $I_{\text{Ca(V)}}$ and corresponding changes in C_m that were elicited by variable-length depolarizations to 0 mV lasting between 2 and 50 ms for an endbulb (Fig. 3.1.12A1) and a calyx terminal (Fig. 3.1.12A2). Capacitance jumps evoked by depolarizations shorter than 2 ms were difficult to resolve in endbulb terminals. The 2 ms depolarization elicited ΔC_m of 17.9 fF and 51.0 fF in the endbulb and calyx, respectively. Assuming a mean vesicle diameter of ~ 50 nm (Ryugo et al., 1996; Taschenberger et al., 2002) and a specific membrane capacitance of $10 \text{ fF}/\mu\text{m}^2$, we estimate an average capacitance of ~ 80 aF for a single vesicle. Capacitance jumps measured in response to 2 ms depolarizations thus correspond to the release of ~ 220 (endbulb) vs. ~ 640 (calyx) vesicles. Longer depolarizations induced larger capacitance jumps. But the increase in ΔC_m became smaller or saturated for pulse durations ≥ 40 ms suggesting depletion of a readily releasable pool of vesicles. In the terminals illustrated in Fig. 3.1.12A, 50 ms steps increased C_m by 77.7 fF (971 vesicles) and 271.9 fF (3399 vesicles) in the endbulb and calyx terminals, respectively.

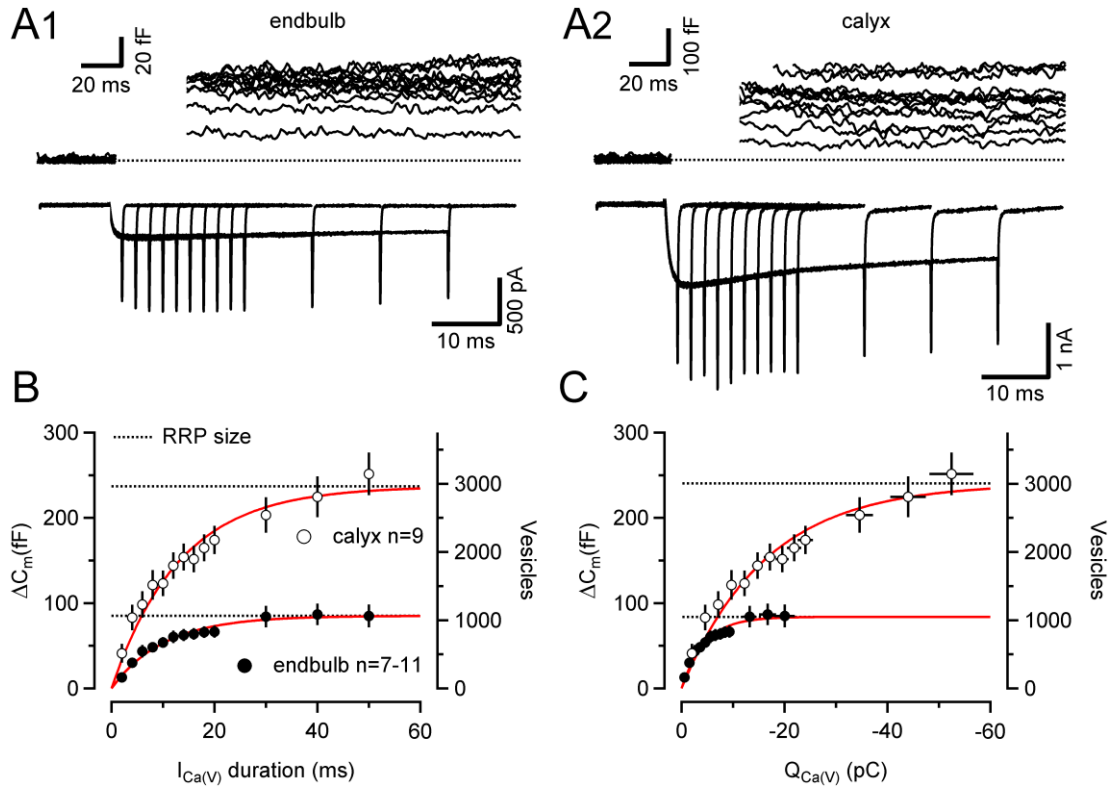


Figure 3.1.12 Readily releasable pool size is significantly smaller at endbulb compared with calyx terminals.

A, Series of depolarizing voltage steps (0 mV, duration from 2 to 50 ms) were applied to an endbulb (A1) and a calyx (A2) terminal. Top panels illustrate ΔC_m . Baseline levels of C_m , R_m , and R_s were 3.81 pF, 1.24 G Ω , and 16.7 M Ω and 22.2 pF, 6.09 G Ω , and 11.5 M Ω for the endbulb and calyx recording, respectively. Corresponding $I_{\text{Ca(V)}}$ are shown in the bottom panels. B,C, Changes in C_m plotted as a function of pulse duration (B) and presynaptic Ca^{2+} charge (C). The corresponding vesicle number (assuming 80 aF as the single vesicle capacitance, see results) are shown on the right axis. ΔC_m saturated for depolarizing voltage steps ≥ 40 ms. Smooth red lines represent single exponential fits. Estimates for the total number of readily releasable vesicles (dotted lines) were derived from the amplitudes of the exponentials.

Pooled data obtained from 7–11 endbulb and 9 calyx terminals are plotted as a function of pulse duration or Ca^{2+} current charge in Figs. 3.1.12B and C, respectively. Single exponentials fitted to the relationship between ΔC_m and pulse duration yielded time constants of 10.2 ms vs. 13.2 ms for endbulbs and calyces, respectively. These values are similar to a ‘weighted’ time constant of vesicle depletion obtained from deconvolution analysis of postsynaptic currents at the calyx synapse when using the same pipette concentration of EGTA (11.1 ms, Sakaba and Neher, 2001). About half of the readily

releasable vesicles were consumed after 7.1 ms versus 9.2 ms pulse durations in the endbulb and calyx terminals, respectively. Faster time constants of release have been observed in the presence of lower concentrations of internal Ca^{2+} buffers (Sakaba and Neher, 2001; Sun and Wu, 2001). Moreover, release probability is heterogeneous at the calyx (Sakaba and Neher, 2001) and other central synapses (Walmsley et al., 1988; Hessler et al., 1993; Rosenmund et al., 1993; Murthy et al., 1997). When fitted with double exponential functions, the fast components of vesicle depletion had time constants of 4.49 ms (endbulb) and 4.46 ms (calyx), which is slightly slower than those obtained from deconvolution analysis of calyceal EPSCs (Sakaba and Neher, 2001).

The average size of the readily releasable pool, obtained from the exponential fits, amounted to 85.1 fF (1064 vesicles) and 237.0 fF (2963 vesicles) for endbulb and calyx terminals, respectively. The total number of readily releasable vesicles was thus ~2.8 times larger for calyx terminals, which is consistent with their ~4 times larger surface area (see above). To estimate the fraction of vesicles released during single APs we ‘back-calculated’ the predicted ΔC_m in response to the Ca^{2+} charge influx elicited by presynaptic APs (see Fig. 3.1.8G, Table 2). Such estimates indicated 20 fF and 3.1 fF corresponding to 250 and 40 vesicles. Thus, the Ca^{2+} current charge entering the terminal during single APs triggers the release of <10% of the total RRP.

Table 1. Comparison of functional properties of endbulb of Held (P9-P11) and calyx of Held (P8-P11) terminals of mice.

| | endbulb P9-P11 | calyx P8-P11 | Significance level (p) |
|--|-------------------------|-------------------------|---------------------------|
| <i>Passive membrane properties</i> | | | |
| C_{terminal} (pF) | 4.3 ± 0.2 (54) | 17.2 ± 0.6 (46) | < 0.001 |
| C_{axon} (pF) | 8.6 ± 0.8 (54) | 20.6 ± 1.7 (46) | < 0.001 |
| R_m (G Ω) | 1.13 ± 0.09 (54) | 1.08 ± 0.09 (46) | n.s. |
| <i>Presynaptic $I_{\text{Ca(V)}}$</i> | | | |
| amplitude (nA) ^a | -0.42 ± 0.03 (28) | -1.29 ± 0.05 (36) | < 0.001 |
| current density (nA/pF) | -0.105 ± 0.008 (28) | -0.076 ± 0.003 (36) | 0.001 |
| inactivation during 100 ms (%) ^b (0.5 mM EGTA) | 31.7 ± 2.0 (14) | 44.5 ± 1.8 (18) | < 0.001 |
| inactivation during 100 ms (%) (10 mM BAPTA) | 18.7 ± 1.8 (9) | 37.2 ± 1.1 (13) | < 0.001 |
| unitary current at 0 mV (pA) | 0.08 ± 0.01 (8) | 0.08 ± 0.00 (10) | n.s. |
| unitary slope conductance (pS) | 1.85 ± 0.16 (8) | 1.80 ± 0.1 (10) | n.s. |
| Ca^{2+} channels/terminal ^d | $6,367 \pm 498$ (28) | $20,438 \pm 801$ (36) | < 0.001 |
| <i>Presynaptic APs</i> | | | |
| AP amplitude (mV) | 122.0 ± 5.1 (5) | 130.5 ± 0.8 (5) | n.s. |
| AP half-width (μ s) | 262.8 ± 14.7 (5) | 356.3 ± 19.2 (5) | < 0.05 |
| <i>Vesicle exocytosis</i> | | | |
| RRP from ΔC_m ^c | 1064 | 2963 | |
| $I_{\text{Ca(V)}}$ (nA) | -0.48 ± 0.05 (7) | -1.29 ± 0.06 (9) | < 0.001 |
| Ca^{2+} channels/vesicle in RRP | 7.6 ± 1.2 (7) | 6.8 ± 0.6 (9) | n.s. |

^a Peak amplitude of $I_{\text{Ca(V)}}$ evoked by a 10 ms step depolarization from -80 mV to 0 mV

^b Inactivation of Ca^{2+} current during the 100 ms step depolarization to 0 mV was expressed as $(I_{\text{peak}} - I_{100\text{ms}}) / I_{\text{peak}}$

^c Size of the RRP was estimated by capacitance measurements. ΔC_m values were converted into vesicle numbers by assuming a single vesicle capacitance of 80aF .

^d Estimates for the total number of VGCCs are derived by dividing $I_{\text{Ca(V)}}$ by the product of unitary current amplitude and the open probability at $V_m = 0$ mV.

Table 2. Parameters of the HH-type m^2 model of presynaptic $I_{\text{Ca(V)}}$ used to simulate AP-driven presynaptic Ca^{2+} influx in endbulb and calyx terminals.

| | endbulb P9-P11 | calyx P8-P11 |
|--|------------------------|------------------------|
| HH-model parameters | | |
| half-activation voltage (mV) | 24.35 | 17.37 |
| steepness factor κ (mV) | 9.63 | 8.23 |
| α_0 (ms^{-1}) | 1.9135 | 1.5012 |
| V_α (mV) | 26.81 | 20.51 |
| β_0 (ms^{-1}) | 0.2146 | 0.2384 |
| V_β (mV) | 20.55 | 20.85 |
| P (μS) | 3.3967 | 1.5916 |
| H (mV) | 12.912 | 19.264 |
| V' (mV) | 35.913 | 32.955 |
| Simulated $I_{\text{Ca(V)}}$ during single presynaptic APs | | |
| peak m^2 | 0.49 ± 0.06 (5) | 0.88 ± 0.01 (5) |
| amplitude (nA) | -0.45 ± 0.06 (5) | -2.78 ± 0.02 (5) |
| current density (nA/pF) | -0.105 ± 0.013 (5) | -0.161 ± 0.001 (5) |
| $Q_{\text{Ca(V)}}$ (pC) | -0.11 ± 0.01 (5) | -0.82 ± 0.03 (5) |
| half-width (μs) | 240 ± 15 (5) | 276 ± 13 (5) |
| open Ca^{2+} channels at peak | $2,616 \pm 318$ (5) | $16,405 \pm 136$ (5) |

3.2 Intracellular Ca^{2+} requirements for Ca^{2+} -dependent inactivation and facilitation of voltage-gated Ca^{2+} channels at rat calyx of Held synapse

3.2.1 Inactivation of presynaptic voltage-gated Ca^{2+} channels

During long-lasting membrane depolarizations, $I_{\text{Ca(V)}}$ in calyx terminals inactivate prominently following a biphasic time course (Fig. 3.2.1A) (Forsythe et al., 1998; Ishikawa et al., 2005). To quantify the contribution of the two kinetically distinct components to $I_{\text{Ca(V)}}$ inactivation during long depolarizations (1 s), we calculated the fractional inactivation during the first 100 ms $[(I_{\text{peak}} - I_{100 \text{ ms}})/I_{\text{peak}}]$ in comparison to that during the remaining 900 ms $[(I_{100 \text{ ms}} - I_{1 \text{ s}})/I_{\text{peak}}]$ (Fig. 3.2.1A,B). When external Ca^{2+} was replaced by Ba^{2+} as a charge carrier, $I_{\text{Ca(V)}}$ peak amplitudes decreased slightly (-1.61 ± 0.14 nA [$n = 10$] vs. -1.14 ± 0.07 nA [$n = 5$], $p = 0.009$, Fig. 3.2.1B *left*). More importantly, the fast component of $I_{\text{Ca(V)}}$ inactivation was strongly reduced in external Ba^{2+} (45.6 ± 2.0 % vs. 24.5 ± 1.6 %, $p < 0.001$, Fig. 3.2.1A,B) whereas the slowly inactivating component was nearly unaffected (24.6 ± 1.1 % vs. 19.9 ± 1.7 %, $p = 0.06$, Fig. 3.2.1B). This observation suggests that the fast but not (or to a lesser extent) the slowly inactivating component of $I_{\text{Ca(V)}}$ is Ca^{2+} -dependent. Because calyces are unlikely to experience long-lasting depolarizations comparable to those shown in Fig. 3.2.1A, we reasoned that the contribution of the slowly inactivating component to $I_{\text{Ca(V)}}$ inactivation under *in-vivo* conditions is very limited and we did not further characterize it in this study.

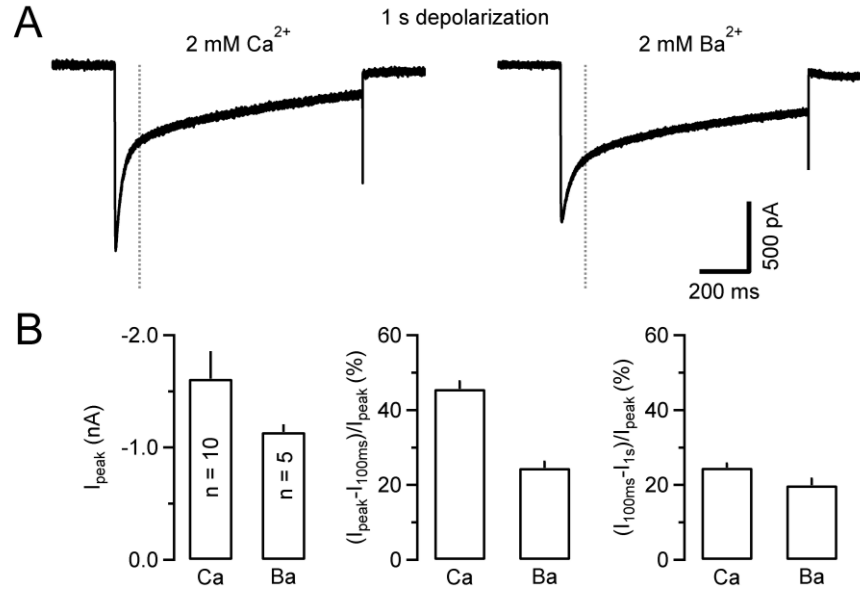


Figure 3.2.1 Two kinetically distinct components of $I_{\text{Ca(V)}}$ inactivation, fast and Ca^{2+} -dependent, slow and Ca^{2+} -independent.

A, Presynaptic $I_{\text{Ca(V)}}$ elicited by 1 s depolarizations from $V_h = -80$ to 0 mV and recorded with either Ca^{2+} (left) or Ba^{2+} (right) as the charge carrier. Inactivation of $I_{\text{Ca(V)}}$ was biphasic under both conditions. The rapidly inactivating component was strongly reduced in amplitude when recording in Ba^{2+} . **B**, Pooled results showing average values of peak amplitudes (left) and normalized fractions of fast (middle) and slowly (right) inactivating components of $I_{\text{Ca(V)}}$. Average amplitudes of $I_{\text{Ca(V)}}$ slightly decreased when substituting extracellular Ca^{2+} with Ba^{2+} ($p = 0.03$). The amplitude of the fast inactivating component of $I_{\text{Ca(V)}}$ was profoundly reduced in extracellular Ba^{2+} ($p < 0.001$) whereas that of the slowly inactivating component was nearly unaltered ($p = 0.06$).

We next tested whether increasing the intracellular Ca^{2+} buffering strength affects $I_{\text{Ca(V)}}$ inactivation. Figure 3.2.2A1 shows samples traces of $I_{\text{Ca(V)}}$ recorded with pipette solutions containing variable chelator species and concentrations. Surprisingly, the time course of $I_{\text{Ca(V)}}$ inactivation was insensitive to manipulation of the Ca^{2+} buffering strength (45.9 ± 1.1 % [0.5 mM EGTA, $n = 12$] vs. 43.6 ± 1.9 % [10 mM EGTA, $n = 9$] vs. 41.8 ± 2.2 % [10 mM BAPTA, $n = 19$] vs. 44.6 ± 1.6 % [30 mM BAPTA, $n = 15$], $p = 0.46$, ANOVA) (Fig. 3.2.2B). In contrast, changes in ΔC_m responses were nearly completely abolished with high concentrations of EGTA or BAPTA in the pipette solution (Fig. 3.2.2A2,B) (Borst et al., 1995).

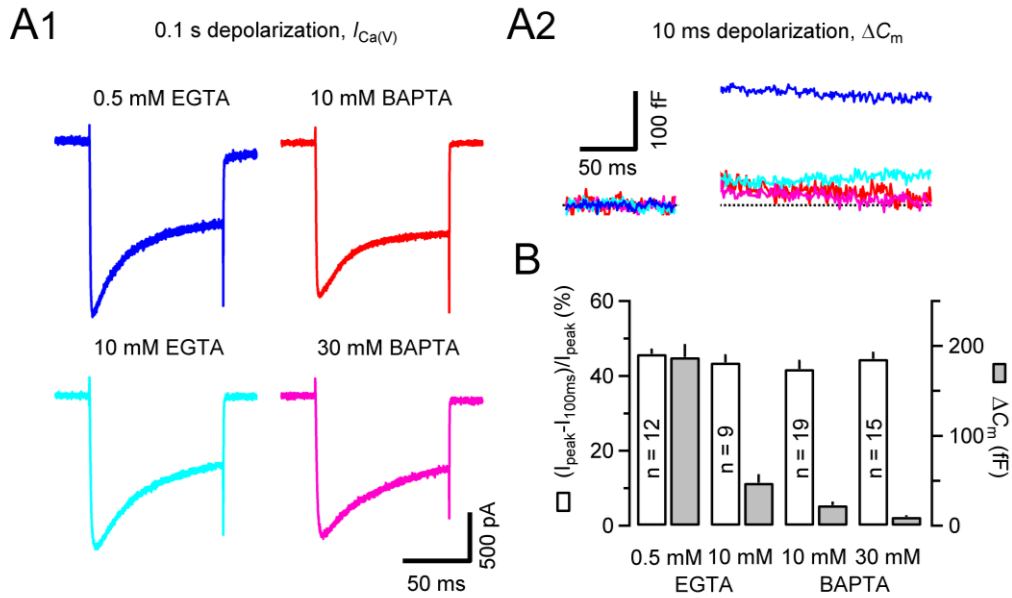


Figure 3.2.2 Insensitivity of Ca^{2+} -dependent inactivation to intracellular Ca^{2+} chelators.

A, Increasing intracellular Ca^{2+} buffering strength has little effect on $I_{\text{Ca(V)}}$ inactivation during 100 ms step depolarizations to 0 mV. **A1**, Presynaptic $I_{\text{Ca(V)}}$ recorded with different concentrations of either EGTA (blue, magenta) or BAPTA (red, pink) in the patch pipette. **A2**, Corresponding ΔC_m traces for the recordings shown in **A1**. As expected, exocytosis is strongly attenuated in the presence of ≥ 10 mM intracellular Ca^{2+} chelator. **B**, Pooled results showing average values for $I_{\text{Ca(V)}}$ inactivation and vesicle exocytosis. Fractional inactivation of $I_{\text{Ca(V)}}$ during 100 ms depolarizations was similar for the three different conditions ($p = 0.46$, ANOVA).

Because even 30 mM of the fast Ca^{2+} buffer BAPTA were unable to effectively antagonize the rate of $I_{\text{Ca(V)}}$ inactivation during 100 ms depolarizations (Fig. 3.2.2B), mechanisms other than Ca^{2+} -dependent inactivation (CDI) of $I_{\text{Ca(V)}}$ may alternatively or additionally account for the current decline. We therefore considered the following two possibilities: (I) Activation of pre- and/or postsynaptic Ca^{2+} permeable conductances may cause a depletion of Ca^{2+} ions from the synaptic cleft (Borst and Sakmann, 1999a). (II) Metabotropic receptors could be directly (mGluRs) or indirectly (CBRs) activated by released glutamate and thereby attenuate $I_{\text{Ca(V)}}$ (Takahashi et al., 1996; Kushmerick et al., 2004). In order to test a contribution of these two mechanisms to $I_{\text{Ca(V)}}$ inactivation I applied a cocktail of antagonists with the aim of blocking all Ca^{2+} permeable ionotropic GluRs as well as mGluRs and CBRs (see Methods). Figure 3.2.3A illustrates a paired

recording of presynaptic $I_{\text{Ca(V)}}$ and EPSCs before and after application of antagonists. While the EPSC is nearly completely abolished, $I_{\text{Ca(V)}}$ remained virtually unchanged in the presence of antagonists (Fig. 3.2.3A2). With 0.5 mM EGTA in the pipette solution, the fractional inactivation of $I_{\text{Ca(V)}}$ during 100 ms depolarizations increased only slightly from $45.9 \pm 1.1\%$ ($n = 12$) in control solution to $49.2 \pm 2.6\%$ ($n = 8$) in the presence of antagonists in the bath ($p = 0.26$). Similar results were obtained with higher EGTA concentration in the pipette ($43.6 \pm 1.1\%$ [$n = 9$] vs. $44.8 \pm 2.0\%$ [$n = 8$], $p = 0.66$, 10 mM EGTA). As shown in Fig. 3.2.3B, a small positive correlation was observed between $I_{\text{Ca(V)}}$ inactivation and its peak amplitude, indicating that the fractional inactivation increases by $\sim 5.5\%$ per nA current amplitude.

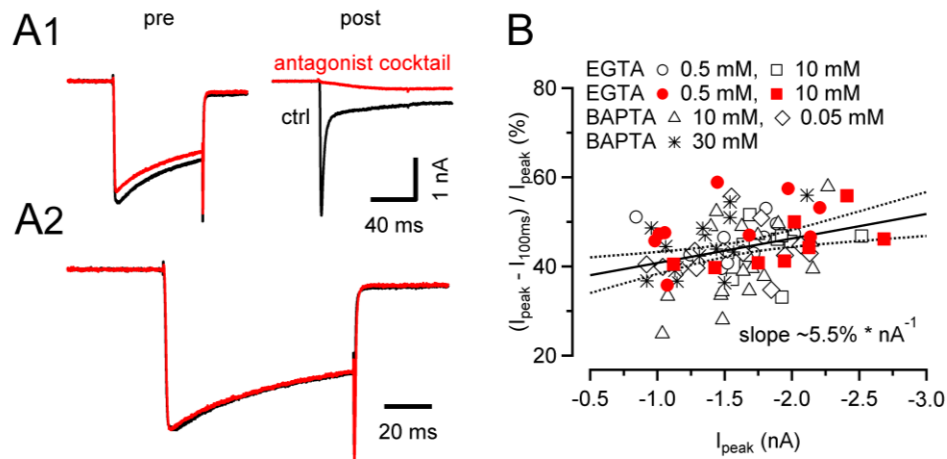


Figure 3.2.3 Depletion of extracellular Ca^{2+} from the synaptic cleft and/or inhibition of VGCCs via metabotropic receptors does not measurably contribute to $I_{\text{Ca(V)}}$ inactivation during sustained depolarizations.

A1, Paired recordings of $I_{\text{Ca(V)}}$ (left) and EPSCs (right) in control (black) solution and after adding a cocktail of glutamate and cannabinoid receptor antagonists (red, see Methods) to suppress Ca^{2+} influx through GluR channels and feedback inhibition via mGluRs and/or CBRs. **A2**, Peak scaled traces of $I_{\text{Ca(V)}}$ shown in **A1** are virtually indistinguishable. **B**, Scatter plot of inactivation vs. peak amplitudes of $I_{\text{Ca(V)}}$. Pooled results obtained with different intracellular Ca^{2+} chelator species and concentrations. Data obtained from recordings in the presence of the antagonist cocktail are plotted with the red symbols. Solid and broken lines represent line fit and 95% confidence limits to the entire data set indicating a positive correlation of $I_{\text{Ca(V)}}$ peak amplitude and degree of inactivation with a slope of $\sim 5.5\% \times \text{nA}^{-1}$.

3.2.2 Clustering of presynaptic VGCC may account for insensitivity of $I_{Ca(V)}$ inactivation to Ca^{2+} chelators

In contrast to somatic VGCCs, those expressed in nerve terminals are known to cluster near release sites (Heuser and Reese, 1981; Pawson et al., 1998). Within overlapping $[Ca^{2+}]_i$ micro domains that built up during channel opening, intracellular chelators can not effectively buffer $[Ca^{2+}]_i$. Even though individual channels switch stochastically between open and closed states during depolarizations, at any time there will be some open channels in a cluster. Despite the presence of chelators, presynaptic VGCCs may thus be constantly exposed to elevated $[Ca^{2+}]_i$ if they are part of a larger channel cluster. We therefore ask whether a reduction of the number of available channels would reduce the rate of $I_{Ca(V)}$ inactivation. Figure 3.2.4A shows that this is indeed the case. When the irreversible P/Q-type VGCC blocker ω -AgaTX was applied to the bath solution, not only the amplitude but also the fractional inactivation of $I_{Ca(V)}$ decreased notably from 47.8% (control) to 34.7% (~50% current block) with 10 mM BAPTA in pipette solution (Fig. 3.2.4A2). A regression line fitted to a scatter plot of $I_{Ca(V)}$ inactivation vs. its peak amplitudes measured after 0%, 33%, 50% and 66% block by ω -AgaTX had a slope of 11.1% per nA (Fig. 3.2.4B,D1). A slowing of $I_{Ca(V)}$ inactivation because of a larger relative contribution of ω -AgaTX-resistant channels is unlikely because the fractional inactivation of $I_{Ca(V)}$ in P/Q-type VGCC deficient mice was essentially equal to that measured in *w.t.* synapses (44.5 ± 1.8 % [n = 18] vs. 44.8 ± 2.4 % [n = 12], p = 0.93, Fig. 3.2.4D2).

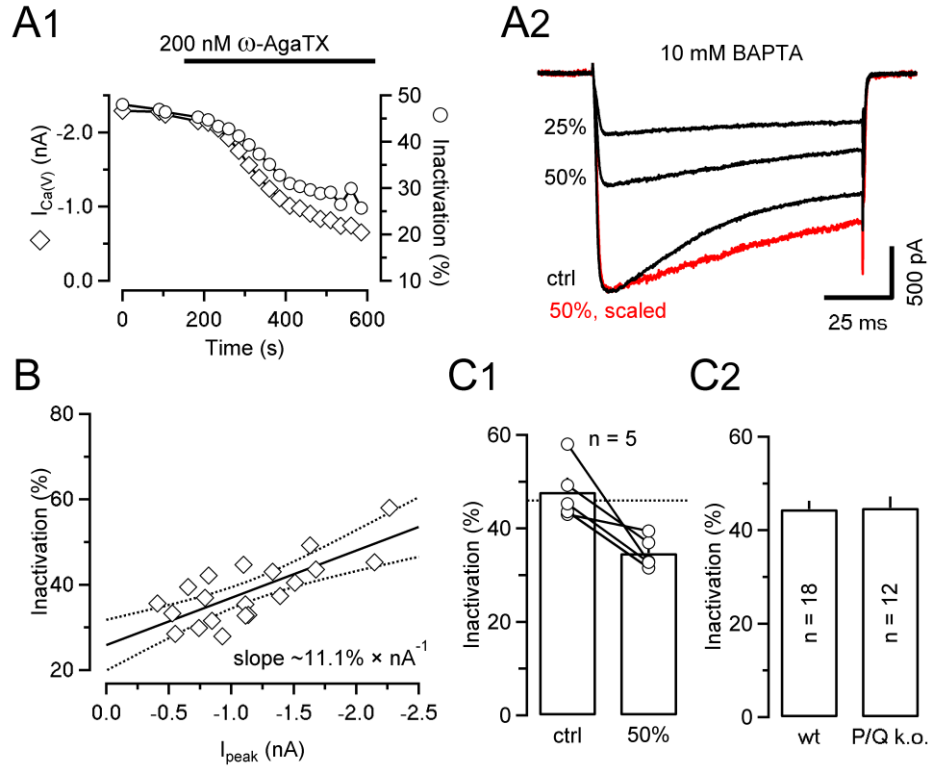


Figure 3.2.4 Clustering of presynaptic VGCCs may account for insensitivity of Ca^{2+} dependent inactivation to intracellular Ca^{2+} chelators.

A1, Time course of peak amplitudes and fractional inactivation of $I_{Ca(V)}$ during bath application of the P/Q-type VGCC blocker ω -AgaTX. **A2**, Sample traces of $I_{Ca(V)}$ recorded before (*ctrl*) or during (50% and 25%) bath application of ω -AgaTX shown superimposed. The red trace represents a peak scaled version of $I_{Ca(V)}$ recorded when it was reduced to ~50% of its initial amplitude. **B**, Line fit to a scatter plot of inactivation vs. peak amplitudes of $I_{Ca(V)}$ at various degrees of block by ω -AgaTX (0%, 33%, 50% and 66%) indicating a positive correlation with a slope of $\sim 11.1\% \times nA^{-1}$. **C**, Comparison of fractional inactivation of $I_{Ca(V)}$. Pooled results obtained from recordings under control condition and after blocking about ~50% of $I_{Ca(V)}$ by ω -AgaTX (**C1**), from calyces lacking P/Q-type VGCCs (**C2**).

During postnatal maturation of the calyx synapse, larger AZ seem to disappear in favor of small ones (Taschenberger et al., 2002) and the number of VGCCs associated with individual docked vesicles seems to decrease (Wang et al., 2008). These developmental changes may result in smaller VGCC cluster in more mature compared to P8–10 calyces. We therefore asked whether $I_{Ca(V)}$ inactivation may decline with age. Indeed, the fractional inactivation of $I_{Ca(V)}$ was strongly reduced in P14–16 calyces compared to younger terminals, and it was further attenuated when recording with a pipette solution

supplemented with high concentration of BAPTA ($28.8 \pm 1.0\%$ [$n = 6$] vs. $12.8 \pm 2.4\%$ [$n = 6$], $p < 0.001$, Fig. 3.2.5A,B).

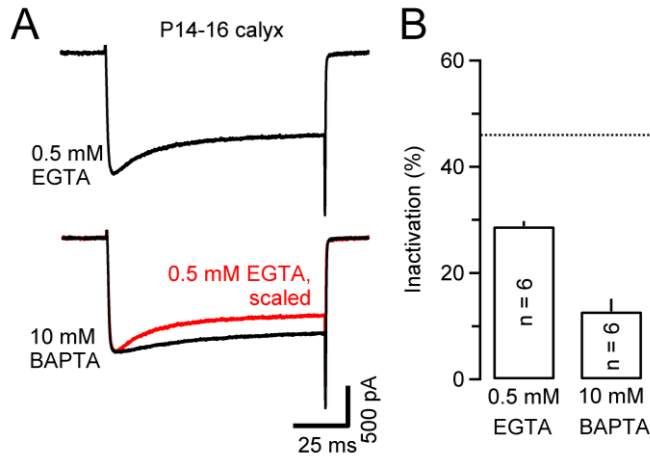


Figure 3.2.5 Inactivation of $I_{Ca(V)}$ becomes sensitive to intracellular Ca^{2+} chelators in mature calyces.

A, Inactivation of $I_{Ca(V)}$ is strongly reduced in more mature calyces. Recordings from two P14–16 terminals with either 0.5 mM EGTA (*top panel*) or 10 mM BAPTA (*bottom panel*) in the patch pipette. The red trace represents a peak scaled version of $I_{Ca(V)}$ recorded with 0.5 mM EGTA. **B**, Comparison of fractional inactivation of $I_{Ca(V)}$. Pooled results obtained from recordings from P14–P16 calyces.

3.2.3 Recovery of $I_{Ca(V)}$ from inactivation

During repetitive AP firing, the modulation of AP-evoked presynaptic Ca^{2+} influx by VGCC inactivation critically depends on the rate of recovery of $I_{Ca(V)}$ from inactivation. To measure the recovery time course we used paired pulse protocol consisting of a 100 ms depolarization 0 mV followed by 20 ms test pulses at various recovery time intervals between 25 ms and 15 s (Fig. 3.2.6). The recovery of $I_{Ca(V)}$ from inactivation was surprisingly slow and followed a biphasic time course with a fast recovery time constant of ~ 320 ms and a slow recovery time constant of ~ 7.2 s (Fig. 3.2.6B). To exclude the possibility that this slow recovery was caused by a delayed clearance of Ca^{2+} entering the terminals during the 100 ms depolarization, we repeated the experiments with elevated intracellular Ca^{2+} chelator concentrations. As expected, the rise of global $[Ca^{2+}]_i$ was strongly attenuated with 10 mM EGTA and nearly completely abolished with 10 mM BAPTA in the pipette solution (Fig. 3.2.6B1). In contrast, the time course of recovery from inactivation was nearly unaffected (Fig. 3.2.6B2). This slow ‘intrinsic’ recovery of

calyceal $I_{Ca(V)}$ from inactivation leads to cumulative inactivation of VGCCs during repetitive stimulation and may account for the strong reduction of presynaptic Ca^{2+} influx observed during high-frequency stimulation (Forsythe et al., 1998; Nakamura et al., 2008).

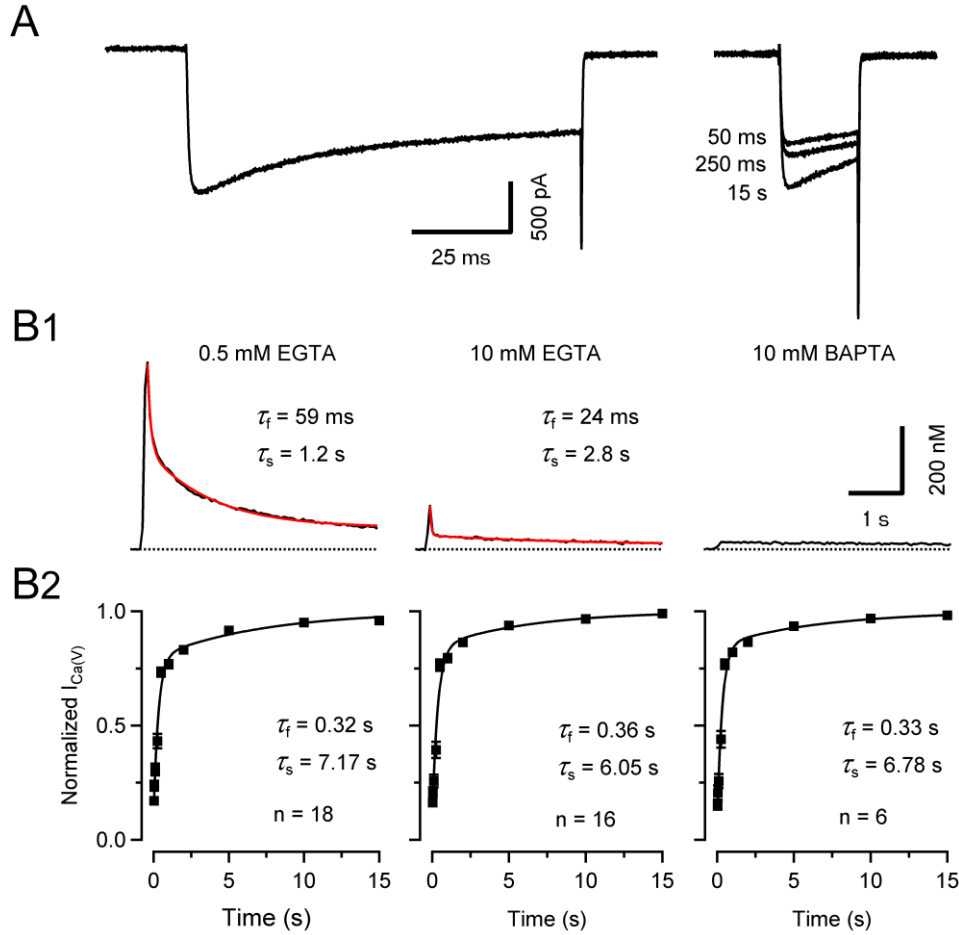


Figure 3.2.6 Recovery of $I_{Ca(V)}$ from inactivation is intrinsically slow, regardless of the Ca^{2+} buffering conditions

A, Recovery of $I_{Ca(V)}$ from inactivation was tested at variable intervals using a paired-pulse protocol consisting of a 100 ms depolarization to 0 mV followed by a 20 ms depolarization at variable inter-stimulus interval. Pipette solution contained 0.5 mM EGTA. Traces for three different recovery intervals are shown superimposed. **B**, The time course of recovery from inactivation was biphasic and was insensitive to changes in Ca^{2+} chelator species and/or concentrations in the pipette solution. **B1**, $[Ca^{2+}]_i$ transients evoked by 100 ms step depolarizations. The rise of global $[Ca^{2+}]_i$ was nearly completely suppressed when adding 10 mM BAPTA to the pipette solution (*right*). **B2**, Average time course of recovery from inactivation. Solid lines represent double exponential fits. Fast and slow time constants were similar for the three $[Ca^{2+}]_i$ buffering conditions ($p > 0.56$, ANOVA).

3.2.4 Probing the $[Ca^{2+}]_i$ sensitivity of $I_{Ca(V)}$ inactivation by UV-light flash photolysis of caged Ca^{2+}

To directly examine the Ca^{2+} requirements for induction of $I_{Ca(V)}$ inactivation, we used Ca^{2+} uncaging while monitoring $[Ca^{2+}]_i$. In a first set of experiments, a UV-light flash was delivered during a 100 ms depolarization to 0 mV to produce a rapid, step-like elevation of the global volume averaged $[Ca^{2+}]_i$ (Fig. 3.2.7). To monitor $[Ca^{2+}]_i$, either Fura 4F (low-intensity flashes) or Fura 2FF (high-intensity flashes) were included in the pipette solution. In the absence of the UV-light flash, 100 ms depolarizations resulted in an maximum elevation of $[Ca^{2+}]_i$ to $\sim 15 \pm 2 \mu M$ ($n = 26$). As illustrated in Fig. 5A, increasing $[Ca^{2+}]_i$ level via Ca^{2+} uncaging by a few micromole did not result in a noticeable change in the rate of $I_{Ca(V)}$ inactivation (Fig. 3.2.7A). This suggests that the Ca^{2+} sensor is either already saturated or ‘sees’ a significantly higher, possibly local $[Ca^{2+}]_i$ signal such that a small increase in global $[Ca^{2+}]_i$ has little further effect on inactivation rate. To differentiate between these two possibilities, we applied a strong UV-light flash that resulted in an elevation of global $[Ca^{2+}]_i$ to $\sim 100 \mu M$ which resulted in a substantial acceleration of the inactivation rate (Fig. 3.2.7B). Three conclusions may be drawn from these experiments: (I) The accelerated decay of $I_{Ca(V)}$ after Ca^{2+} uncaging directly demonstrates that $I_{Ca(V)}$ inactivation is, at least in part, Ca^{2+} -dependent. (Townsend et al.) The immediate change in inactivation time course following high post-flash $[Ca^{2+}]_i$ without any noticeable delay is incompatible with a mechanisms that involves a diffusible molecule and rather suggests that the Ca^{2+} sensor for CDI must be located on a protein pre-associated with VGCCs. (III) Because only large elevations in post-flash $[Ca^{2+}]_i$ affected the inactivation kinetics, we postulate that during depolarizations the Ca^{2+} sensor experiences high $[Ca^{2+}]_i$, further supporting the notion

that the effector protein responsible for CDI must be located within molecular distance to the channel itself.

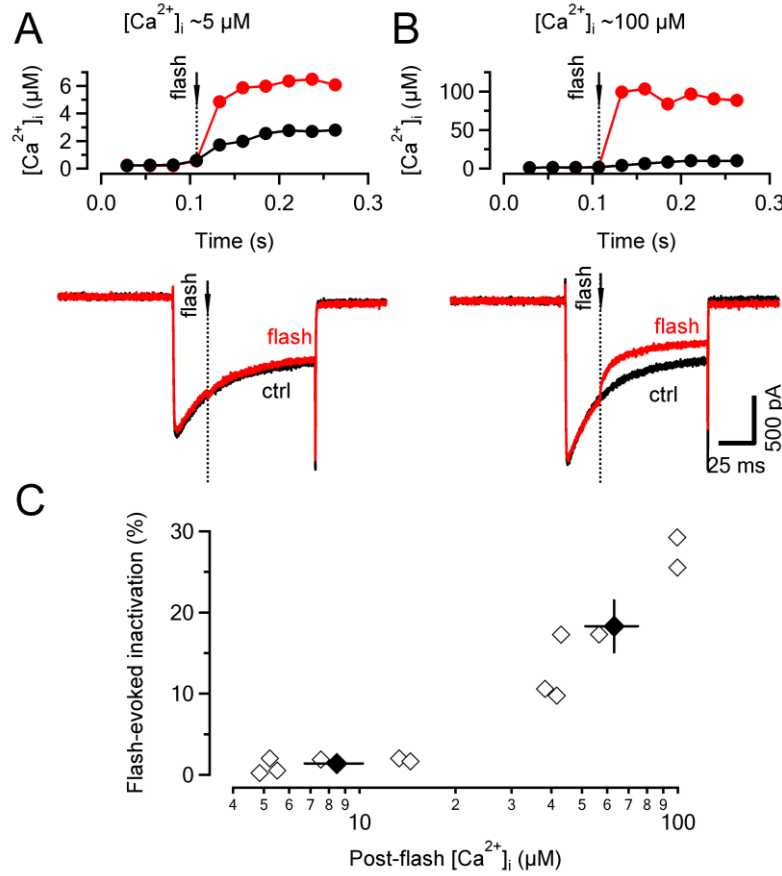


Figure 3.2.7 The sensor mediating Ca^{2+} -dependent inactivation ‘sees’ high $[Ca^{2+}]_i$ concentrations and must be closely associated with Ca^{2+} channels.

A, $I_{Ca(V)}$ (bottom panel) elicited by step depolarizations to 0 mV with (black) and without a UV-light flash (dotted line) delivered ~ 25 ms after current onset. Changes in $[Ca^{2+}]_i$ are illustrated in the top panel. Note that the rate of $I_{Ca(V)}$ inactivation was unaltered after UV-flash uncaging despite a ~ 3 fold elevation of $[Ca^{2+}]_i$ relative to control conditions (without flash). **B**, Similar experiment as illustrated in (A) except that the post flash $[Ca^{2+}]_i$ increased to $\sim 100 \mu M$. Note the immediate acceleration of the inactivation time course after Ca^{2+} uncaging. **C**, Scatter plot of flash-evoked $I_{Ca(V)}$ inactivation as a function of global $[Ca^{2+}]_i$. Flash-evoked $I_{Ca(V)}$ inactivation was quantified as the ratio of the final $I_{Ca(V)}$ amplitude measured after a flash compared to that of a control current. Black symbols represent mean \pm SEM for post-flash $[Ca^{2+}]_i$ of $\leq 15 \mu M$ and $\geq 40 \mu M$. Note that for $[Ca^{2+}]_i$ of $\leq 15 \mu M$ virtually no additional inactivation was elicited by Ca^{2+} uncaging.

In a second set of experiments, we quantified the fractional inactivation induced by Ca^{2+} uncaging 56 ms before a test $I_{Ca(V)}$ with the principal aim of establishing the apparent

dose response relationship between $[Ca^{2+}]_i$ and $I_{Ca(V)}$ inactivation (Fig. 3.2.8). We elicited elevations of $[Ca^{2+}]_i$ between 0.6 and 100 μM by adjusting flash intensity and/or DM-nitrophen concentration in the patch pipette while monitoring $[Ca^{2+}]_i$. Inactivation was measured as the ratio between peak amplitudes of post-flash $I_{Ca(V)}$ relative to a control current measured ~20 s before the flash. The 20 s interval was long enough to allow full recovery from inactivation induced during the control depolarization (Fig. 3.2.8A1).

Inactivation of $I_{Ca(V)}$ was first noticeable for post-flash $[Ca^{2+}]_i \geq 1 \mu M$ and severe for post-flash $[Ca^{2+}]_i \geq 10 \mu M$ (Fig. 3.2.8A2). The amount of inactivation did not increase when probed with second test depolarization delivery 112 ms after a flash (twice the interval between flash and the 1st depolarization) (Fig. 3.2.8B). To exclude the possibility that the measured $I_{Ca(V)}$ inactivation merely resulted from a changed driving force due to elevated cytosolic Ca^{2+} , we compared the I - V relationship after uncaging with that of a control current recorded before the flash by applying voltage ramps (Fig. 3.2.8C). As with step depolarizations, the post-flash $I_{Ca(V)}$ was strongly reduced in amplitude. However, its I - V relationship was virtually unaltered (Fig. 3.2.8C inset) which is the expected behavior for an ion conductance for highly asymmetrically distributed in- and extracellular charge carriers. Figure 3.2.8D shows pooled data from 75 flashes in 40 terminals. The relationship between $[Ca^{2+}]_i$ and the fractional inactivation of $I_{Ca(V)}$ was fitted by a Hill function. The apparent half maximal inhibitory concentration (IC_{50}), maximal inactivation and Hill coefficient were $6.1 \pm 0.8 \mu M$, $38 \pm 2\%$ and 1.6 ± 0.2 , respectively.

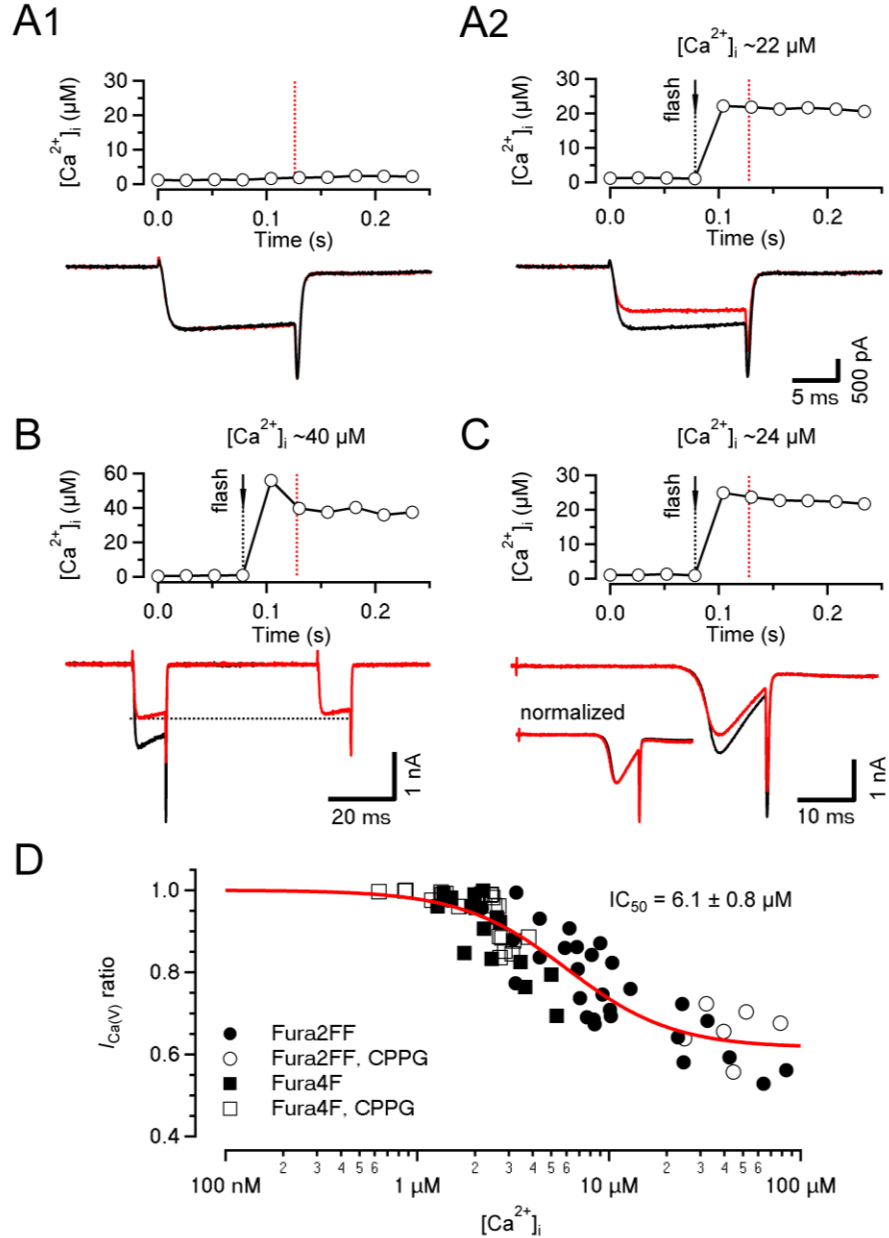


Figure 3.2.8 $[Ca^{2+}]_i$ sensitivity of $I_{Ca(V)}$ inactivation assayed by Ca^{2+} uncaging via flash UV-photolysis.

A, Comparison of $I_{Ca(V)}$ elicited by two step depolarizations to 0 mV separated by a 20 s interval, without (**A1**) or with (**A2**) a UV-light flash delivered 50 ms before the 2nd $I_{Ca(V)}$ (red traces). The time course of $[Ca^{2+}]_i$ shortly before and during the 2nd depolarization (red dotted line) is shown in the top panel. In the absence of the UV-light flash, the two currents were nearly identical indicating that a 20 s interval was sufficient to allow full recovery from inactivation (**A1**, bottom). In contrast, a global elevation of $[Ca^{2+}]_i$ by UV-flash photolysis induced a pronounced reduction of the 2nd current in the same terminal (**A2**). **B**, No further reduction of $I_{Ca(V)}$ was observed when probed with an additional depolarization ~112 ms after the UV-light flash. **C**, Similar experiment as illustrated in (**A**) except that $I_{Ca(V)}$ was elicited by ramping V_m from -80 to +40 mV. Note the reduced current amplitude (bottom panel) but similar $I-V$ relation (bottom panel inset) of the 2nd $I_{Ca(V)}$ (red trace) following the UV-light flash. **D**, Dose-response relationship of Ca^{2+} -dependent inactivation vs. $[Ca^{2+}]_i$. Pooled data obtained from 75 flashes in 40 terminals. Solid line represents a Hill function fitted to the data.

3.2.5 Characterization of $I_{Ca(V)}$ facilitation

Among presynaptically expressed R-, N- and P/Q-type VGCCs, the latter channel subtype is unique in that it can exhibit strong Ca^{2+} -dependent facilitation (CDF) during repetitive depolarizations (Borst and Sakmann, 1998a; Cuttle et al., 1998). We therefore set out to compare the $[Ca^{2+}]_i$ requirements for CDF to those for inducing CDI. To quantify CDF, we compared the charge transfer during the initial 3 ms of $I_{Ca(V)}$ ($Q_{3\text{ ms(test)}}$ / $Q_{3\text{ ms(ctrl)}}$) elicited by a 10 ms test pulse to V_m between -15 to -25 mV with and without a 10 ms conditioning pulse to $+20$ mV. The conditioning pre-pulse resulted in both an accelerated activation as well as a larger amplitude of the test current (Fig. 3.2.9A1). A hyperpolarization of the terminal to -140 mV during the inter-pulse interval (Fig. 3.2.9A1 *blue trace*), did not affect the amount of facilitation ruling out the possibility that it was voltage- rather than Ca^{2+} -dependend ($n = 5$). The ratio $Q_{3\text{ ms(test)}}$ / $Q_{3\text{ ms(ctrl)}}$ showed little sensitivity to changes in the intracellular Ca^{2+} buffering strength (Fig. 7A2, 0.5 mM EGTA: 1.82 ± 0.06 [$n = 16$]; 10 mM EGTA: 1.65 ± 0.05 [$n = 15$]; 10 mM BAPTA: 1.65 ± 0.06 [$n = 15$], $p = 0.6$, ANOVA) and, unlike CDI (Fig. 3.2.6), CDF decayed very quickly with a mean time constant of ~ 30 ms irrespective of the different strength of Ca^{2+} chelator (Fig. 3.2.9B).

To assay the $[Ca^{2+}]_i$ sensitivity of CDF, we elicited step-like elevation of $[Ca^{2+}]_i$ by flash photolysis. The degree of CDF of $I_{Ca(V)}$ elicited by Ca^{2+} uncaging was comparable to that elicited by conditioning pre-pulses (Fig. 3.2.10A). The scatter plot in Fig. 3.2.10B illustrates the relationship between CDF and post-flash $[Ca^{2+}]_i$ in the concentration range between ~ 1 μM to ~ 100 μM . CDF was first observed for $[Ca^{2+}]_i$ values ≥ 2 μM and

peaked between $\sim 5 \mu\text{M}$ to $10 \mu\text{M}$. With higher $[\text{Ca}^{2+}]_i$, CDF was difficult to elicit because $I_{Ca(V)}$ tended to decrease relative to control. We fitted the data with the product of two Hill functions with the parameters for CDI fixed to the values obtained earlier (Fig. 3.2.8D) and obtained an apparent half maximum $[\text{Ca}^{2+}]_i$ for CDF of $2.4 \pm 0.7 \mu\text{M}$ (maximum CDF = 1.6 ± 0.3 , Hill coefficient = 3.0 ± 2.7). The $[\text{Ca}^{2+}]_i$ sensitivity for CDF was thus surprisingly similar to that of CDI.

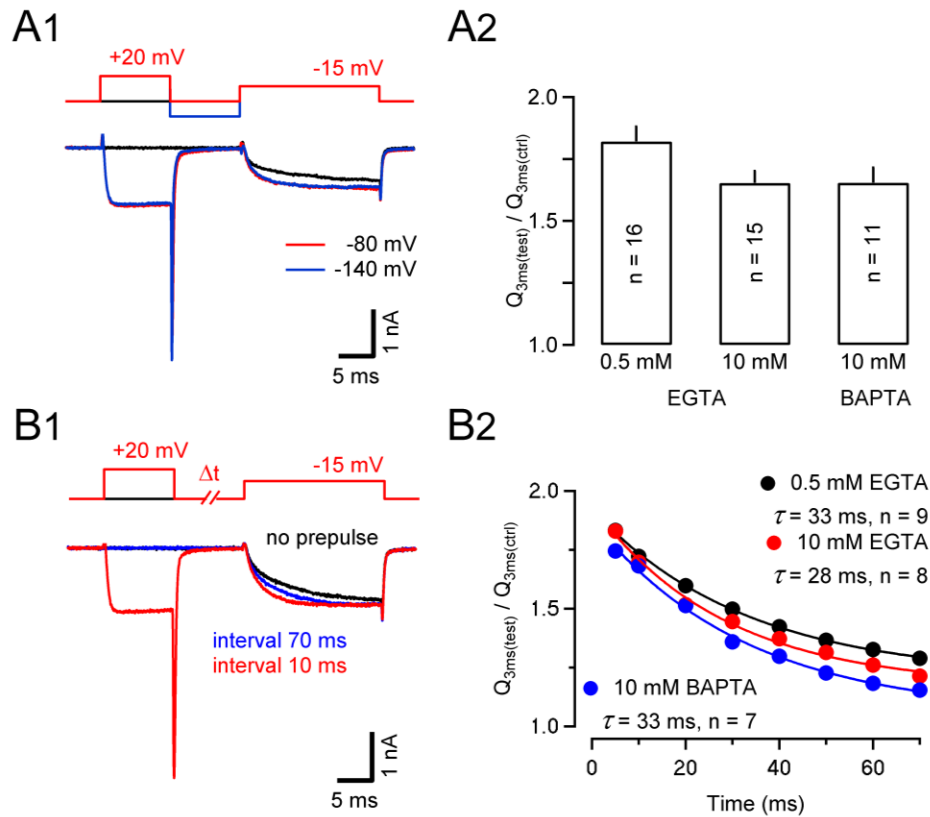


Figure 3.2.9 Presynaptic $I_{Ca(V)}$ shows robust Ca^{2+} dependent facilitation during pre-pulse protocols.

A1, Sample traces of $I_{Ca(V)}$ elicited by stepping to -15 mV with (red trace) or without (black trace) a preceding pre-pulse to $+20 \text{ mV}$ (20 ms inter-pulse interval). Facilitation was quantified as the ratio of charges transferred during the initial 3 ms of $I_{Ca(V)}$ with or without pre-pulse. Note that a hyperpolarization to -140 between pre- and test pulse (blue trace) did not alter the amount of current facilitation. **A2**, Increasing intracellular Ca^{2+} buffer strength only slightly suppressed facilitation of $I_{Ca(V)}$. **B1**, Sample traces of $I_{Ca(V)}$ without (black trace) or with prepulse at 10 ms (red) or 70 ms interval (blue). **B2**, The relaxation of $I_{Ca(V)}$ facilitation is an order of magnitude faster than recovery from inactivation and insensitive to changes in $[\text{Ca}^{2+}]_i$ buffering strength. Solid lines represent single exponential fits.

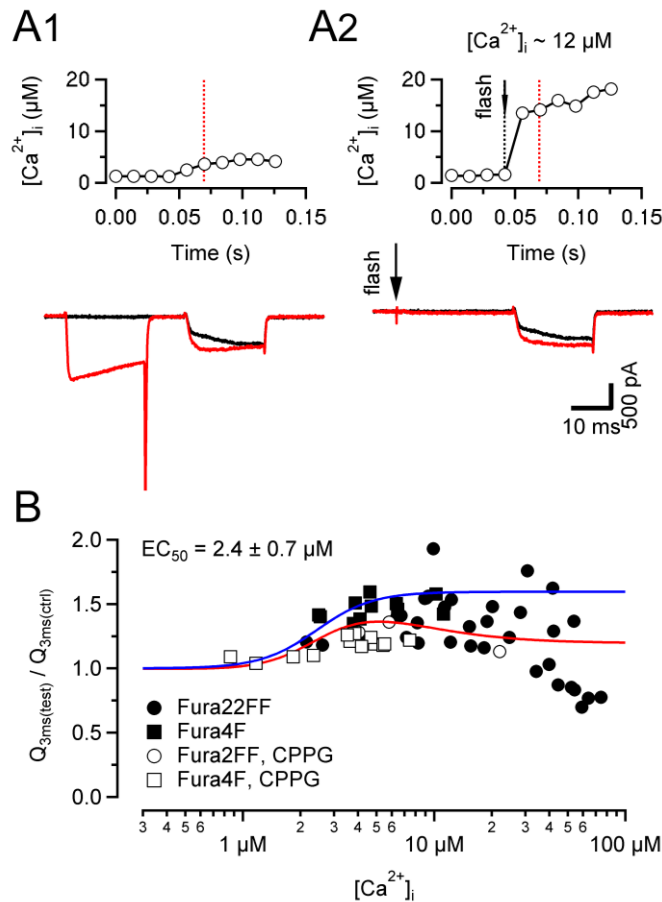


Figure 3.2.10 $[Ca^{2+}]_i$ sensitivity of $I_{Ca(V)}$ facilitation assayed by Ca^{2+} uncaging via UV-flash photolysis.

A, Comparison of $I_{Ca(V)}$ facilitation elicited by either prepulse (**A1**) or Ca^{2+} uncaging (**A2**) (red traces). The interval between the UV-light flash and the test depolarization was 20 ms. Control current traces without preceding prepulse or without Ca^{2+} uncaging are shown for comparison (black traces). Recordings were obtained from the same terminal. The time course of $[Ca^{2+}]_i$ shortly before and during the 2nd depolarization is shown in the top panel. **B**, Dose-response relationship of $I_{Ca(V)}$ facilitation vs. $[Ca^{2+}]_i$. Maximum facilitation was observed for $[Ca^{2+}]_i$ elevations between 5 to 15 μM . At $[Ca^{2+}]_i > 20 \mu M$, Ca^{2+} -dependent inactivation of $I_{Ca(V)}$ was observed. The solid red line represents a product of two Hill functions fitted to the data. The solid blue line represent the simulated dose-response relationship of $[Ca^{2+}]_i$ facilitation in the absence of Ca^{2+} -dependent inactivation

3.2.6 $[Ca^{2+}]_i$ transients during AP firing in nearly unperturbed calyx terminals

Having established the $[Ca^{2+}]_i$ requirements for CDI and CDF in calyx terminals, we wanted to estimate the range of global $[Ca^{2+}]_i$ achieved during presynaptic AP firing in order to predict the contribution of CDF and/or CDI to the modulation of AP-evoked Ca^{2+} influx. The nerve fibers giving rise to calyces of Held typically discharge at frequencies between <1 Hz and >100 Hz even in the complete absence of sound (Sonntag et al., 2009). During sound stimulation, AP firing rates can transiently reach several hundreds of Hz (Kopp-Scheinpflug et al., 2008). In order to establish a concentration range of the presynaptic volume averaged cytosolic Ca^{2+} and its dependency on firing

frequency and number of APs in a burst, we imaged $[Ca^{2+}]_i$ in nearly unperturbed calyx terminals.

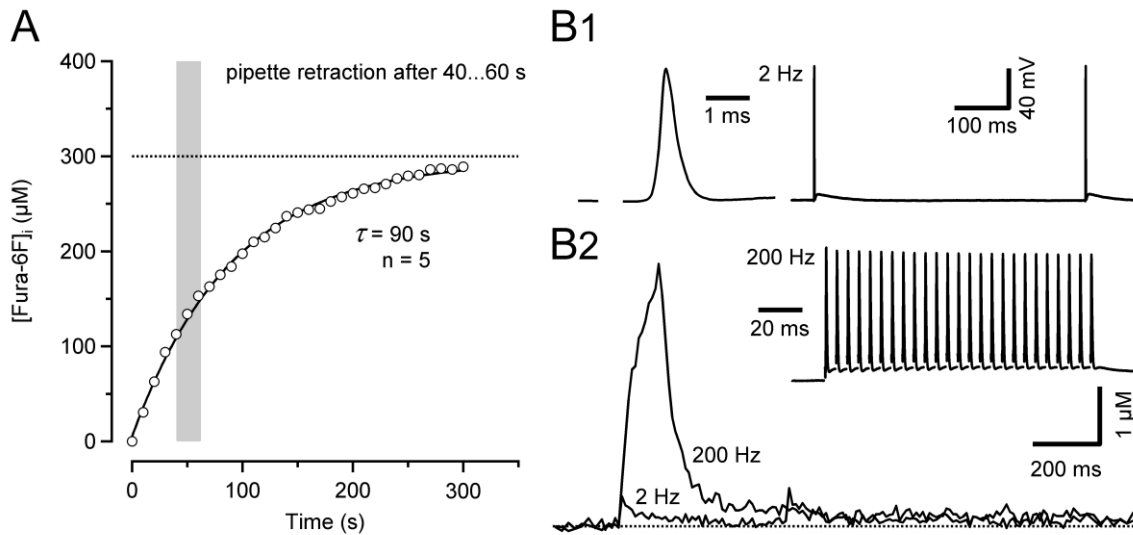


Figure 3.2.11 Estimating AP-evoked changes in global $[Ca^{2+}]_i$ in nearly unperturbed calyx terminals.

A, Changes in fluorescence intensity measured every 10 s at the isobestic point ($F_{iso}=358$ nm) after establishing presynaptic whole-cell configuration with a pipette containing 300 μM Fura-6F (black circles). The solid line represents a single exponential fit yielding a time constant of ~ 90 s. For measuring $[Ca^{2+}]_i$ during AP trains in nearly unperturbed terminals, pipettes were gently retracted after 40–60 s (estimated $[Fura-6F]_i \sim 125$ μM). **B**, Changes in $[Ca^{2+}]_i$ elicited by presynaptic APs. **B1**, Two APs separated by 500 ms inter-stimulus interval (top panel) and a 200 Hz train of APs (bottom panel) were elicited by after afferent fiber stimulation. AP waveforms were recorded during dye preloading. **B2**, Corresponding changes in $[Ca^{2+}]_i$ measured after pipette retraction. To improve the signal to noise ratio, 25 (2 Hz) and 5 (200 Hz) individual sweeps were averaged.

To preserve the concentration of mobile endogenous Ca^{2+} buffers, terminals were preloaded with ~ 125 μM of the low-affinity Ca^{2+} indicator Fura 6F ($K_d = 15$ μM) (Fig. 3.2.11). During the preloading time in whole-cell configuration, presynaptic APs were recorded in current-clamp mode (Fig. 3.2.11B1) to establish the stimulation threshold for AP generation and excluded terminals with AP failures during afferent fiber stimulation. After gently retracting the pipette, global $[Ca^{2+}]_i$ signals in response to train stimulation were measured. Sample traces illustrating the time course of $[Ca^{2+}]_i$ during AP firing at 2 Hz and 200 Hz are shown in Figure 3.2.11B2.

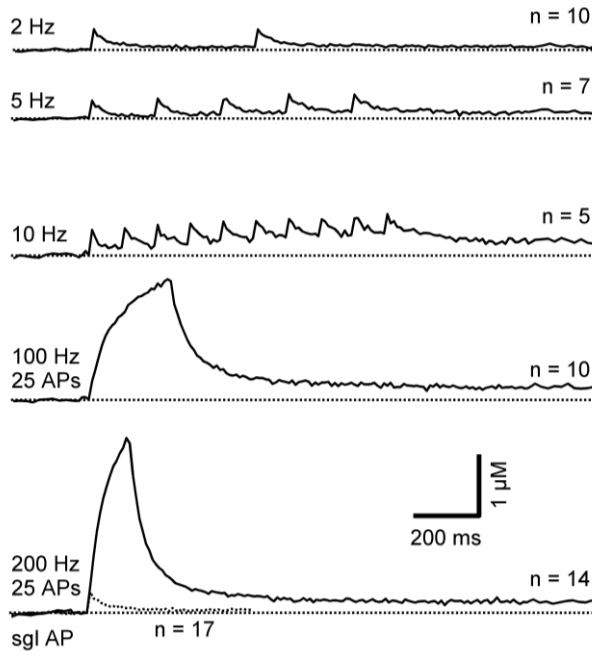


Figure 3.2.12 Global $[Ca^{2+}]_i$ can increase to several micromoles during short high-frequency AP bursts.

$[Ca^{2+}]_i$ measured in preloaded calyx terminals during AP trains evoked by afferent fiber stimulation (2 Hz to 200 Hz). Averages traces from 5 to 14 terminals. Single APs elicited $[Ca^{2+}]_i$ transients with a peak amplitude of ~ 300 nM that decayed quickly ($\tau = 29$ ms) back to resting level. During train stimulation with frequencies ≤ 5 Hz little summation of AP-evoked $[Ca^{2+}]_i$ transients was observed. For stimulus frequencies ≥ 10 Hz, $[Ca^{2+}]_i$ transients elicited by individual APs summated. During high-frequency stimulation with burst consisting of 25 APs, the global $[Ca^{2+}]_i$ transient peaked at ~ 2.0 μ M (100 Hz) and ~ 2.8 μ M (200 Hz). The dotted red line in the two bottom panels represent the simulated $[Ca^{2+}]_i$ for the same stimulus. The time course of $[Ca^{2+}]_i$ after a single AP is shown superimposed in the bottom panel for comparison (dotted black trace).

Figure 3.2.12 shows average $[Ca^{2+}]_i$ transients obtained from 5 to 17 individual nerve terminals. A single AP elevated the volume averaged global $[Ca^{2+}]_i$ by 341 ± 36 nM (Fig. 3.2.12, $n = 22$) which is similar to previously reported values (Helmchen et al., 1997; Müller et al., 2007). The relaxation of the Ca^{2+} transients was well fit by a double-exponential function having fast and slow decay time constants of 24 ± 6 ms and 190 ± 92 ms ($n = 17$), respectively (Müller et al., 2007). During paired pulse stimulation (500 ms interval), $[Ca^{2+}]_i$ transients decreased slightly in amplitude from 336 ± 36 nM to 289 ± 40 nM ($p = 0.12$, $n = 10$) presumably due to $I_{Ca(V)}$ inactivation (Xu and Wu, 2005). At firing frequencies ≥ 10 Hz, AP-evoked transients started to summated and finally reached peak concentrations of several micromoles. Again, a trend towards smaller peak amplitudes of individual AP-evoked Ca^{2+} transients was observed during the 10 Hz trains (1st AP: 413 ± 69 nM, 10th AP: 315 ± 16 nM, $n = 5$, $p = 0.19$). $[Ca^{2+}]_i$ transients elicited by high-frequency stimulation peaked at 2.0 μ M (100 Hz) and 2.9 μ M (200 Hz) and

decayed slightly slower compared to single AP responses, with fast and slow decay time constants of 33 ± 1 ms and 211 ± 20 ms (200 Hz, $n = 14$), respectively.

3.2.7 Modulation of $I_{Ca(V)}$ during trains of AP-like depolarizations

As illustrated above, CDF had a rapid onset kinetics whereas CDI developed more slowly. In addition, the recovery kinetics of both process differed by an order of magnitude, suggesting that CDI and CDF will be differentially recruited during trains of brief, AP-like depolarizations of different frequencies. Figure 3.2.13 illustrates relative changes in Ca^{2+} tail current amplitudes during trains consisting of 25 AP-like depolarizations (1 ms from $V_h = -80$ to 0 mV) at frequencies from 1 Hz to 200 Hz and with variable amounts of buffers in the patch pipette. Tail current amplitudes elicited by the first 1 ms depolarization were comparable among the three different recording conditions (0.5 mM EGTA: 2.27 ± 0.13 nA, Fig. 3.2.13A; 10 mM EGTA: 1.87 ± 0.09 nA, Fig. 3.2.13C; 10 mM BAPTA: 1.91 ± 0.18 nA, Fig. 3.2.13D; $p = 0.15$, ANOVA). Under control conditions (0.5 mM EGTA), CDI was observed for stimulation frequencies ≤ 20 Hz. For frequencies ≥ 50 Hz, $I_{Ca(V)}$ facilitated during the initial 3–5 stimuli before decreasing in amplitude such that at the end of the trains, it was smaller than the initial value (Fig. 3.2.13A). Interestingly, the late inactivation of $I_{Ca(V)}$ during high-frequency trains was attenuated by conditioning low-frequency (10 Hz) trains (Fig. 3.2.13B).

Raising the intracellular concentration of EGTA or replacing it with 10 mM BAPTA primarily attenuated the amount of CDI during trains but left CDF nearly intact (Fig. 3.2.13C,D). For 10 Hz trains, the average reduction of the last $I_{Ca(V)}$ compared to the 1st decreased from 16.3 ± 1.3 % (0.5 mM EGTA) to 11.6 ± 1.3 % (10 mM EGTA) and $3.4 \pm$

0.5 % (10 mM BAPTA) ($p < 0.001$, ANOVA). In contrast, the maximum CDF measured during 200 Hz trains increased slightly from 9.2 ± 1.0 % (0.5 mM EGTA) to 12.5 ± 0.9 % (10 mM EGTA, $p = 0.05$).

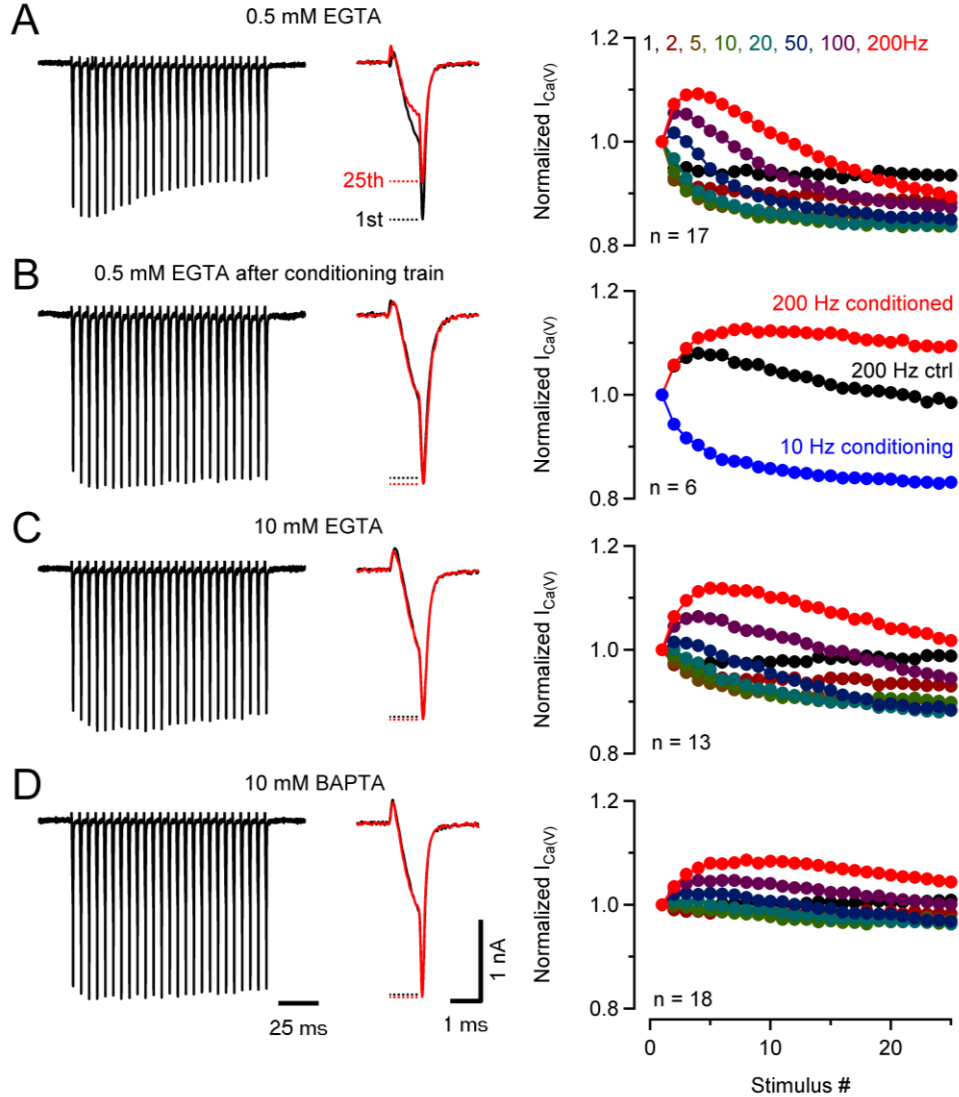


Figure 3.2.13 Inactivation of $I_{Ca(V)}$ during high-frequency trains of AP-like depolarizations is strongly attenuated by Ca^{2+} buffers and by conditioning low-frequency trains.

$I_{Ca(V)}$ was elicited by a burst of 1 ms depolarizations to 0 mV (25 stimuli) in the presence of 0.5 mM EGTA (A,B), 10 mM EGTA (C), and 10 mM BAPTA (D) in the patch-pipette. Representative experiments are shown in the *left column*, summary results are plotted in the *right column*. First (black traces) and last (red traces) $I_{Ca(V)}$ are shown superimposed for comparison next to the $I_{Ca(V)}$ train. **A**, Under control conditions, $I_{Ca(V)}$ showed initial facilitation followed by inactivation. **B**, Inactivation was strongly reduced relative to control (black symbols) after preconditioning with a 10 Hz train (15 depolarizations, blue symbols). **C,D**, Increasing intracellular Ca^{2+} buffering strength attenuated $I_{Ca(V)}$ inactivation but left $I_{Ca(V)}$ facilitation largely intact.

Discussion

4.1 Presynaptic Ca^{2+} influx and vesicle exocytosis at mouse endbulb of Held terminals

A large glutamatergic mammalian presynaptic terminal – the endbulb of Held – was characterized in depth in this study. Beyond demonstrating the feasibility of direct recordings from this presynaptic ending in acute brain slices, our study revealed several fundamental parameters including passive membrane properties and the kinetics of presynaptic APs. We studied gating characteristics of VGCCs and estimate their unitary current amplitudes to approximate the number of VGCC per terminal. We used a combination of electrophysiological recordings together with modeling to study AP-evoked Ca^{2+} influx at the endbulb synapse. Finally, we used capacitance measurements to estimate the number of readily releasable vesicles.

Although all endbulbs are large axosomatic endings, they can vary considerably in shape (Ryugo and Fekete, 1982). We cannot exclude that different morphological categories of endbulb terminals also differ in their functional properties. Endbulbs arising from auditory fibers having low spontaneous discharge rates have been reported to have a more complex shape than those of high discharge rates (Ryugo and Sento, 1991). In addition, at the age P9–11, mouse endbulb terminals have not yet acquired their mature morphology (Neises et al., 1982; Limb and Ryugo, 2000). Thus, further developmental changes in their functional properties analogous to those reported for calyx of Held terminals (Iwasaki and Takahashi, 1998; Taschenberger and von Gersdorff, 2000; Taschenberger et al., 2002; Fedchyshyn and Wang, 2005; Wang et al., 2008) are likely to occur.

4.1.1 Unequivocal identification of endbulb terminals

We recorded from relatively young endbulb terminals which have a cup-shaped morphology and only few filopodia arise from their main swelling (Limb and Ryugo, 2000). This compact morphology facilitates identification the presynaptic terminals in acute slices and may be advantageous during voltage-clamp experiments. In some experiments we used fluorescent dyes to verify pre- or postsynaptic recording sites. However, because of their distinct passive membrane properties, recordings from endbulbs and bushy cells can be easily distinguished without the use of fluorescent dyes. During most experiments, we took advantage of the capacitance jump observed in response to membrane depolarization as an additional criterion to identify presynaptic terminals.

4.1.2 Heterogeneous size of endbulb terminals

We determined the membrane capacitance of endbulbs in comparison to calyces from the fast components of charging transients recorded under voltage-clamp. Assuming a specific membrane capacitance of $10 \text{ fF}/\mu\text{m}^2$, we estimate an average surface area of $\sim 430 \mu\text{m}^2$ vs. $1720 \mu\text{m}^2$ for endbulb and calyx terminals, respectively. The area values are probably upper estimates because the charging of proximal parts of the axon may contribute to the fast capacitive current transients.

Our estimate for the total surface area of endbulb terminals is 2–4 times larger than those for hippocampal ($40\text{--}110 \mu\text{m}^2$; Rollenhagen et al., 2007) and cerebellar mossy terminals ($69\text{--}200 \mu\text{m}^2$, Xu-Friedman and Regehr, 2003) based on serial electron microscopy, but

considerably smaller than those for calyces of Held from mice (this study) or rats ($\sim 2400 \mu\text{m}^2$; Borst and Sakmann, 1998b; $\sim 2500 \mu\text{m}^2$; Sätzler et al., 2002). Assuming a disc-like geometry for the two types of terminals and a height of $\sim 1 \mu\text{m}$ (Ryugo and Fekete, 1982; Nicol and Walmsley, 2002; Taschenberger et al., 2002; Ryugo et al., 2006), our surface area estimates correspond to disc diameters of $\sim 16 \mu\text{m}$ versus $\sim 32 \mu\text{m}$, thus representing $\sim 20\%$ versus $\sim 41\%$ of the total circumference of a contacted soma having a diameter of $\sim 25 \mu\text{m}$. The surface of such disc-like structures would represent $\sim 22\%$ vs. $\sim 88\%$ of the surface of the contacted neurons for endbulbs and calyces, respectively. These estimates seem reasonable because SBCs of the AVCN accommodate 1 to 4 presynaptic contacts (Ryugo and Sento, 1991; Nicol and Walmsley, 2002) whereas principal cells of the MNTB generally receive only a single calyceal input. Interestingly, the area covered by endbulb silhouettes in Golgi impregnations or HRP-labeled terminals of the cat AVCN typically range from ~ 200 to $\sim 400 \mu\text{m}^2$ (Brawer and Morest, 1975; Ryugo and Sento, 1991) which comes close to the expected $\sim 50\%$ of the total surface area of endbulb terminals estimated in this study.

4.1.3 Fast presynaptic APs in endbulb terminals

A characteristic feature of auditory synapses is their ability to transmit reliably at high rates of stimulation. Brief presynaptic APs may help to generate fast release transients and rapid EPSCs which are advantageous to accomplish this task. Indeed, calyceal APs acquire very rapid kinetics during postnatal development (Taschenberger and von Gersdorff, 2000). We found that endbulb APs have similar rapid kinetics. In fact, the average half-width of the endbulb APs was significantly shorter when compared to calyx

APs of the same age (see Fig. 3.1.8). It should be noted that presynaptic APs evoked by afferent fiber stimulation had slightly faster kinetics than those evoked by current injection. A similar tendency towards shorter half-width for fiber stimulation-evoked APs was also observed for mossy fiber boutons (Bischofberger et al., 2002). Interestingly, during prolonged depolarizations by current injection, endbulb terminals generally generated only single APs, which is reminiscent of the behavior of more mature calyx terminals (Nakamura and Takahashi, 2007). These findings may indicate that endbulb terminals are slightly advanced in their functional maturation with respect to calyx of Held terminals at the same age. This would not be surprising because initial contact between endbulb terminals and SBCs is established before birth (Neises et al., 1982) but only at ~P2 for the calyx of Held terminal and principal MNTB neuron (Hoffpauir et al., 2006; Rodriguez-Contreras et al., 2008).

4.1.4 Rapidly gating Ca^{2+} channels in endbulb terminals

Amplitudes of $I_{\text{Ca(V)}}$ were on average 3 times smaller in endbulb compared to calyx terminals which is consistent with the much smaller size of endbulb terminals (see Fig. 3.1.6). In contrast, Ca^{2+} current densities were relatively similar for the two types of terminals studied here and also in comparison to hippocampal mossy fiber boutons (Bischofberger et al., 2002) suggesting that this parameter may be relatively uniform among mammalian synapses.

$I_{\text{Ca(V)}}$ at endbulb terminals activated at slightly more negative V_m when compared to that of calyx terminals. This could be related to the finding that the endbulb $I_{\text{Ca(V)}}$ was dominated by P/Q-type channels which seem to have a steady-state activation curve with

a slightly more negative midpoint potential when compared to N-type VGCCs (Ishikawa et al., 2005; Li et al., 2007). Calyx terminals of the same age may express a higher fraction of N-type VGCCs (Wu et al., 1999). At P10, ~75 % of $I_{\text{Ca(V)}}$ was contributed by P/Q-type channels in calyces (Iwasaki et al., 2000) whereas the fraction of ω -AgaTX-sensitive VGCCs was ~86% at endbulb terminals (see Fig. 3.1.4A).

In order to approximate the total number of Ca^{2+} channels expressed at endbulb and calyx terminals, we estimated the unitary conductance i of VGCCs by means of variance-mean analysis. Our estimates for i at $V_h = 0$ mV were similar for endbulb and calyx terminals but slightly small than those obtained at mossy fiber boutons (Li et al., 2007). We estimate an average number of 6,400 and 20,400 VGCCs expressed at endbulb and calyx terminals, respectively. These numbers likely represent lower limits because we assumed an open probability of ≥ 0.8 at $V_m = 0$ mV. However, single channel recordings indicate that even at very high V_m , the open probability of VGCCs is probably significantly lower than 1 (Colecraft et al., 2001). Indeed, the variance-mean relationship for $I_{\text{Ca(V)}}$ measured at around -20 mV was well fit by a linear regression (see Fig. 3.1.9), suggesting a relatively low open probability of VGCCs at this membrane potential.

To simulate AP-driven Ca^{2+} influx at endbulb terminals, we derived a HH-type m^2 model (Borst and Sakmann, 1998b). We estimate that ~50% of all activatable channels are open at the peak of $I_{\text{Ca(V)}}$ during an AP. This number is considerably larger for mouse (~90%, see Fig.3.1.8) or rat (~70 %, Borst and Sakmann, 1998b) calyx terminals because of their longer presynaptic APs at this age. Because of the large number of expressed Ca^{2+}

channels and their effective opening by presynaptic endbulb APs, it is likely that multiple VGCCs control the release of a single transmitter vesicle at the endbulb of Held synapse, similarly as has been suggested for calyx terminals (Borst and Sakmann, 1998b).

4.1.5 Absence of $I_{Ca(V)}$ inactivation during AP-like trains

During long-lasting tetanic stimulation of calyx synapses at high rates, $I_{Ca(V)}$ inactivates substantially (Forsythe et al., 1998) and this Ca^{2+} -dependent inactivation of VGCCs can contribute to synaptic depression (Xu and Wu, 2005). In endbulb terminals, $I_{Ca(V)}$ showed robust facilitation during trains of short AP-like depolarizations especially at stimulus frequencies ≥ 20 Hz (Borst and Sakmann, 1998a; Cuttle et al., 1998). No indication for $I_{Ca(V)}$ inactivation was observed. Thus, synaptic depression at endbulb terminals is likely to be mediated by vesicle depletion and/or postsynaptic receptor desensitization (Yang and Xu-Friedman, 2008; Chanda and Xu-Friedman, 2010) rather than presynaptic Ca^{2+} channel inactivation as suggested recently by Wang et al. (2010).

4.1.6 A large pool of releasable vesicles in endbulb terminals

We compared vesicle exocytosis at endbulb and calyx terminals using capacitance measurements which have the advantage of being independent of postsynaptic receptors and thus avoid non-linearities due to receptor saturation and desensitization. Well resolved capacitance jumps were obtained for depolarizations ≥ 2 ms. We estimate that the pool of readily releasable vesicle in endbulb terminals consists of ~ 1060 vesicles. Thus, the pool is substantially larger than previously estimated using cumulative evoked

EPSCs (Oleskevich et al., 2004). Assuming 155 active zones per endbulb terminal (Nicol and Walmsley, 2002), this would translate into 7 docked vesicles per active zone.

At the endbulb terminal, about half of the vesicles in the readily releasable pool (~530 vesicles) could be release within the first ~7 ms of a depolarization to 0 mV suggesting that multiple rounds of exocytosis occurred at individual active zones during this time. Since short, AP-like depolarizations triggered the release of <10% of the total RRP, release probability must to very low at the endbulb synapse. At the calyx of Held, a large fraction of docked vesicles seems to be located relatively distant from the sites of Ca^{2+} influx (Wadel et al., 2007) and vesicles of the RRP seem heterogeneous regarding their intrinsic properties (Wölfel et al., 2007). Thus, only part of the readily releasable vesicles contributes to the fast, synchronous release transients underlying AP-evoked EPSCs. It remains to be determined whether such heterogeneities exist in the endbulb of Held terminal, and how this shapes synaptic processing in the cochlear nucleus.

4.2 Intracellular Ca^{2+} requirements for Ca^{2+} -dependent inactivation and facilitation of voltage-gated Ca^{2+} channels at rat calyx of Held synapse

In this present study, we combined whole-cell recordings of presynaptic voltage-gated Ca^{2+} current with Ca^{2+} uncaging via flash photolysis and ratiometric Ca^{2+} imaging in order to establish the intracellular Ca^{2+} requirements for the induction of Ca^{2+} -dependent inactivation and facilitation of presynaptic VGCCs. Our results indicate that relative low elevations in $[\text{Ca}^{2+}]_i$ by only a few micromoles are sufficient to induce CDI and CDF. Our experimental results suggest that the global volume averaged $[\text{Ca}^{2+}]_i$ can easily attain such levels during repetitive AP firing of the calyx terminal. Thus, presynaptic Ca^{2+} influx is subject to regulation by CDF and CDI during normal physiological spike activity.

4.2.1 Two kinetically distinct components of inactivation

During long-lasting depolarization the amplitude of the calyceal $I_{\text{Ca(V)}}$ strongly declines (Forsythe et al., 1998). Several potential mechanisms have been suggested to account for this current inactivation. We found that intracellular Ca^{2+} uncaging causes strong inactivation of $I_{\text{Ca(V)}}$. The maximum inactivation observed after flash photolysis was comparable to the amount of inactivation seen during 100 ms depolarization. These results directly demonstrate that elevated $[\text{Ca}^{2+}]_i$ causes $I_{\text{Ca(V)}}$ inactivation and suggest that CDI accounts for the majority of the fast component of $I_{\text{Ca(V)}}$ inactivation. Substituting external Ca^{2+} by Ba^{2+} reduced but did not abolish the fast inactivation while having little effect on the slow inactivation. Thus, we can not exclude that voltage-dependent inactivation (Cox and Dunlap, 1994; Patil et al., 1998) also contributes to the

fast component of inactivation, but we assume that this mechanism accounts for the majority of the slow inactivation of $I_{Ca(V)}$.

4.2.2 Glutamate release-dependent decrease of $I_{Ca(V)}$

Since presynaptic depolarization, especially in the presence of low concentrations of intracellular Ca^{2+} buffers, trigger the release of glutamate from the terminals, we also had to consider a negative regulation of $I_{Ca(V)}$ by activation of mGluRs (Takahashi et al., 1996) or via retroinhibition by cannabinoids acting on CB1Rs (Kushmerick et al., 2004). Additionally or alternatively, a decrease in $I_{Ca(V)}$ amplitude could be caused by the depletion of Ca^{2+} from the synaptic cleft because of concomitant activation of postsynaptic Ca^{2+} permeable NMDA and non-NMDA receptors (Borst and Sakmann, 1999a). However, all the aforementioned mechanisms of $I_{Ca(V)}$ inactivation are ‘release-dependent’, i.e. they require the release of glutamate from the presynaptic terminal. Presynaptic glutamate release is strongly attenuated in the presence of high concentrations of intracellular Ca^{2+} chelators in the young calyx of Held (Borst et al., 1995). Since we did not observe a prominent change in the inactivation kinetics of $I_{Ca(V)}$ between control recordings and those with a high concentration of EGTA or BAPTA in the pipette solution, we conclude that glutamate release-dependent mechanisms do not prominently contribute to inactivation during 100 ms depolarizations.

4.2.3 Insensitivity of $I_{Ca(V)}$ inactivation to intracellular chelators

In some neurons (Kasai and Aosaki, 1988; Cox and Dunlap, 1994; Grant and Fuchs, 2008; Benton and Raman, 2009) and for certain subunit combinations of heterologously expressed VGCCs (Lee et al., 2000a; Kreiner and Lee, 2006), CDI can be effectively

antagonized by high concentrations of intracellular Ca^{2+} buffers. In the calyx of Held, a high intracellular Ca^{2+} buffering strength has little effect on $I_{Ca(V)}$ inactivation (Forsythe et al., 1998; Borst and Sakmann, 1999a). One may speculate that a tight clustering of presynaptic VGCCs may account for the observed insensitivity of CDI to chelators. This speculation would be based on the following two observations: firstly, inactivation gradually decreases when reducing the number of VGCCs by means of application of the irreversible VGCC antagonists ω -AgaTX (Fig. 3.2.4A,B). Secondly, the rate of inactivation is substantially reduced in more mature calyces (Fig. 3.2.5A,B) whose active zones tend to have a smaller average diameter (Taschenberger et al., 2002) and possibly harbor fewer VGCCs,

At the neuromuscular junction, presynaptic VGCCs channels form clusters at the AZ area (Feeney et al., 1998; Harlow et al., 2001) and, although unproven, the topology of calyceal VGCCs may be similar. Because the onset kinetic of CDI elicited by Ca^{2+} uncaging is so rapid (Fig. 3.2.7) (Morad et al., 1988), it is likely that the effector molecule hosting the Ca^{2+} sensor triggering CDI is located within molecular distance to and presumably pre-associated with the Ca^{2+} channel. If this holds true, the Ca^{2+} sensor will be exposed to the micro- or nano-domain Ca^{2+} which is only weakly affected by buffers. In addition, VGCC clustering will lead to a scenario in which the Ca^{2+} sensor for inactivation is constantly exposed to high $[Ca^{2+}]_i$ during depolarizations irrespective of the stochasting opening and closing of individual channels. If the average number of VGCCs in a channel cluster is reduced, either experimentally by applying an open channel blocker or during synapse maturation, Ca^{2+} chelators with a rapid binding kinetics may become more efficient in attenuating the effective Ca^{2+} concentration and

thereby CDI. Interestingly, reducing the number of available VGCCs by applying ω -AgaTX also led to a concomitant decrease of $I_{\text{Ca(V)}}$ inactivation from $48 \pm 4\%$ (control) to $27 \pm 3\%$ (66% block by ω -AgaTX). Moreover, $I_{\text{Ca(V)}}$ inactivation was significantly reduced from an average of $\sim 46\%$ (P8–10) to $\sim 29\%$ in more mature terminals and was further attenuated ($\sim 13\%$) in the presence of high BAPTA (Fig. 3.2.5). Additionally, alternative splicing of the pore-forming $\alpha_12.1$ subunit (Soong et al., 2002) as well as changes in expression of auxiliary VGCC subunits (Lee et al., 2000a) may be responsible for the developmental decline in $I_{\text{Ca(V)}}$ inactivation at the calyx of Held.

4.2.4 Similar intracellular Ca^{2+} requirements for CDI and CDF

When probing their $[\text{Ca}^{2+}]_i$ sensitivity by Ca^{2+} uncaging, we found that both, CDI as well as CDF, could be elicited already by relatively low elevations of $[\text{Ca}^{2+}]_i$ ($<10 \mu\text{M}$) implying a high affinity of the corresponding Ca^{2+} sensors. Assuming that the effector molecules inducing CDI and CDF are closely associated with VGCCs (Fig. 3.2.7) and thus be exposed to the Ca^{2+} micro- or nano-domains that build up during channel opening, the Ca^{2+} concentration at the sensors may approach saturation during sustained depolarizations. During trains of brief, AP-like voltage steps, both Ca^{2+} -dependent feedback mechanisms showed different sensitivity to intracellular chelators. In contrast to CDF, CDI was strongly attenuated by 10 mM intracellular EGTA or BAPTA. A parsimonious explanation for this opposite behavior may lie in a different binding and unbinding kinetics for Ca^{2+} . If the Ca^{2+} sensor for CDI binds Ca^{2+} much more slowly than that for CDF, its occupancy will remain low during very brief Ca^{2+} transient. During trains of brief AP-like depolarization, long lasting Ca^{2+} changes due to the rise of global $[\text{Ca}^{2+}]_i$ will contribute relatively strongly to the induction of CDI compared to the very

brief local Ca^{2+} transients. Eliminating the rise in $[\text{Ca}^{2+}]_i$ by high Ca^{2+} buffers would therefore be expected to reduce the amount of CDI. In contrast, if its Ca^{2+} sensor had rapid binding and unbinding kinetics, CDF would be expected to rely only little on the slowly summing global $[\text{Ca}^{2+}]_i$ signal during trains of AP-like stimuli. Thus, the effect of high concentrations of EGTA or BAPTA should be limited which is what we observed experimentally.

4.2.5 Molecular identity of the Ca^{2+} sensor mediating CDI and CDF

CDI and CDF of P/Q-type VGCCs are presumed to be mediated through an interaction with Ca^{2+} binding to the C-terminal and N-terminal lobes of calmodulin (Lee et al., 2000a; DeMaria et al., 2001; Lee et al., 2003). Kinetic rates of conformational changes of calmodulin upon Ca^{2+} binding to the two lobes differ by more than an order of magnitude (Park et al., 2008). A differential Ca^{2+} binding kinetics of the calmodulin lobes might thus be the molecular substrate conferring “local Ca^{2+} selectivity” to CDF and “global Ca^{2+} selectivity” to CDI (Tadross et al., 2008). Calmodulin binding domain peptide and the organic calmodulin inhibitor calmidazolium reportedly suppress CDI in the calyx of Held (Xu and Wu, 2005). On the other hand, dialyzing calyx terminals with pipette solution containing neuronal calcium sensor 1 (NCS-1) mimicked and partially occluded CDF suggesting that facilitation is largely mediated by NCS-1 (Tsujimoto et al., 2002) rather than calmodulin. Clearly, more work is required in order to understand the molecular underpinnings of VGCC modulation in presynaptic nerve terminals.

Summary

The functional properties of mammalian presynaptic nerve endings remain elusive since most terminals of the central nervous system are not accessible to direct electrophysiological recordings. In the present study, functional properties and Ca^{2+} -dependent feedback modulation of presynaptic voltage-gated Ca^{2+} channels were studied by direct recordings from two types of large glutamatergic nerve terminals of the mammalian auditory brainstem –endbulbs of Held and calyces of Held.

Endbulb of Held terminals were identified by their high input resistance and small capacitance. Presynaptic VGCCs in endbulbs were predominantly of the P/Q type and expressed at a high density with an estimated average number of 6400 channels per terminal. Presynaptic Ca^{2+} currents activated and deactivated rapidly. Simulations of action potential (AP)-driven gating of VGCCs suggests that endbulb APs trigger brief Ca^{2+} influx with a mean half-width of 240 μs and a peak amplitude of 0.45 nA which results from the opening of approximately 2600 channels. Endbulb terminals are endowed with a large readily releasable vesicle pool (1064 vesicles) of which only a small fraction is consumed during a single AP-like stimulus. Unlike Ca^{2+} currents at the calyx of Held, $I_{\text{Ca(V)}}$ of endbulb terminals showed no inactivation during trains of AP-like presynaptic depolarizations.

Because of their larger size, calyx of Held terminals can be easily visualized. Presynaptic P/Q-type channels expressed in calyx terminals show two types of Ca^{2+} -dependent feedback regulation – inactivation (CDI) and facilitation (CDF). We studied the

mechanisms and intracellular Ca^{2+} requirements for CDI and CDF. $I_{\text{Ca(V)}}$ in calyx terminals inactivated with a biphasic time course. The fast component of inactivation was Ca^{2+} -dependent. CDI during sustained depolarizations was relatively insensitive to Ca^{2+} chelators. The contribution to $I_{\text{Ca(V)}}$ inactivation of Ca^{2+} depletion from the synaptic cleft or that of metabotropic feedback mechanisms was negligible. Recovery of $I_{\text{Ca(V)}}$ from inactivation was slow and followed a biexponential time course with average time constants of ~320 ms and ~7.2 s. In contrast, $I_{\text{Ca(V)}}$ facilitation decayed very fast with an average time constant of ~30 ms. Intracellular Ca^{2+} requirement for CDI and CDF were probed by Ca^{2+} uncaging via flash photolysis. $[\text{Ca}^{2+}]_i$ elevations in the micromolar range were sufficient to induce CDI and CDF. Half maximum concentrations were ~6 μM and ~2 μM for CDI and CDF, respectively. During repetitive AP firing, the global $[\text{Ca}^{2+}]_i$ can easily reach levels of a few micromoles in unperturbed calyx terminals suggesting that CDF and CDI can be induced during normal physiological presynaptic AP firing. Because of the divergent onset and recovery kinetics of CDI and CDF, facilitation of VGCCs is expected to occur during high-frequency AP bursts. In contrast, low-frequency firing will lead to cumulative inactivation of presynaptic VGCCs.

Bibliography

- Augustine GJ (1990) Regulation of transmitter release at the squid giant synapse by presynaptic delayed rectifier potassium current. *J Physiol* 431:343-364.
- Augustine GJ, Charlton MP, Smith SJ (1985) Calcium entry into voltage-clamped presynaptic terminals of squid. *J Physiol* 367:143-162.
- Banks MI, Smith PH (1992) Intracellular recordings from neurobiotin-labeled cells in brain slices of the rat medial nucleus of the trapezoid body. *J Neurosci* 12:2819-2837.
- Barnes-Davies M, Forsythe ID (1995) Pre- and postsynaptic glutamate receptors at a giant excitatory synapse in rat auditory brainstem slices. *J Physiol* 488 (Pt 2):387-406.
- Benton MD, Raman IM (2009) Stabilization of Ca current in Purkinje neurons during high-frequency firing by a balance of Ca-dependent facilitation and inactivation. *Channels (Austin)* 3:393-401.
- Bischofberger J, Geiger JR, Jonas P (2002) Timing and efficacy of Ca²⁺ channel activation in hippocampal mossy fiber boutons. *J Neurosci* 22:10593-10602.
- Borst JG, Sakmann B (1998a) Facilitation of presynaptic calcium currents in the rat brainstem. *J Physiol* 513 (Pt 1):149-155.
- Borst JG, Sakmann B (1998b) Calcium current during a single action potential in a large presynaptic terminal of the rat brainstem. *J Physiol* 506 (Pt 1):143-157.
- Borst JG, Sakmann B (1999a) Depletion of calcium in the synaptic cleft of a calyx-type synapse in the rat brainstem. *J Physiol* 521 Pt 1:123-133.
- Borst JG, Sakmann B (1999b) Effect of changes in action potential shape on calcium currents and transmitter release in a calyx-type synapse of the rat auditory brainstem. *Philos Trans R Soc Lond B Biol Sci* 354:347-355.
- Borst JG, Helmchen F, Sakmann B (1995) Pre- and postsynaptic whole-cell recordings in the medial nucleus of the trapezoid body of the rat. *J Physiol* 489 (Pt 3):825-840.
- Brandt A, Khimich D, Moser T (2005) Few CaV1.3 channels regulate the exocytosis of a synaptic vesicle at the hair cell ribbon synapse. *J Neurosci* 25:11577-11585.
- Brawer JR, Morest DK (1975) Relations between auditory nerve endings and cell types in the cat's anteroventral cochlear nucleus seen with the Golgi method and Nomarski optics. *J Comp Neurol* 160:491-506.
- Brawer JR, Morest DK, Kane EC (1974) The neuronal architecture of the cochlear nucleus of the cat. *J Comp Neurol* 155:251-300.
- Brown AM, Tsuda Y, Wilson DL (1983) A description of activation and conduction in calcium channels based on tail and turn-on current measurements in the snail. *J Physiol* 344:549-583.
- Cant NB, Morest DK (1979) Organization of the neurons in the anterior division of the anteroventral cochlear nucleus of the cat. Light-microscopic observations. *Neuroscience* 4:1909-1923.
- Catterall WA (2000) Structure and regulation of voltage-gated Ca²⁺ channels. *Annu Rev Cell Dev Biol* 16:521-555.

- Catterall WA, Goldin AL, Waxman SG (2005a) International Union of Pharmacology. XLVII. Nomenclature and structure-function relationships of voltage-gated sodium channels. *Pharmacol Rev* 57:397-409.
- Catterall WA, Perez-Reyes E, Snutch TP, Striessnig J (2005b) International Union of Pharmacology. XLVIII. Nomenclature and structure-function relationships of voltage-gated calcium channels. *Pharmacol Rev* 57:411-425.
- Chanda S, Xu-Friedman MA (2010) A low-affinity antagonist reveals saturation and desensitization in mature synapses in the auditory brain stem. *J Neurophysiol* 103:1915-1926.
- Chaudhuri D, Issa JB, Yue DT (2007) Elementary mechanisms producing facilitation of Cav2.1 (P/Q-type) channels. *J Gen Physiol* 129:385-401.
- Colecraft HM, Brody DL, Yue DT (2001) G-protein inhibition of N- and P/Q-type calcium channels: distinctive elementary mechanisms and their functional impact. *J Neurosci* 21:1137-1147.
- Cox DH, Dunlap K (1994) Inactivation of N-type calcium current in chick sensory neurons: calcium and voltage dependence. *J Gen Physiol* 104:311-336.
- Cuttle MF, Tsujimoto T, Forsythe ID, Takahashi T (1998) Facilitation of the presynaptic calcium current at an auditory synapse in rat brainstem. *J Physiol* 512 (Pt 3):723-729.
- DeMaria CD, Soong TW, Alseikhan BA, Alvania RS, Yue DT (2001) Calmodulin bifurcates the local Ca²⁺ signal that modulates P/Q-type Ca²⁺ channels. *Nature* 411:484-489.
- Dunlap K, Luebke JI, Turner TJ (1995) Exocytotic Ca²⁺ channels in mammalian central neurons. *Trends Neurosci* 18:89-98.
- Ertel EA, Campbell KP, Harpold MM, Hofmann F, Mori Y, Perez-Reyes E, Schwartz A, Snutch TP, Tanabe T, Birnbaumer L, Tsien RW, Catterall WA (2000) Nomenclature of voltage-gated calcium channels. *Neuron* 25:533-535.
- Fedchyshyn MJ, Wang LY (2005) Developmental transformation of the release modality at the calyx of held synapse. *J Neurosci* 25:4131-4140.
- Feeney CJ, Karunanithi S, Pearce J, Govind CK, Atwood HL (1998) Motor nerve terminals on abdominal muscles in larval flesh flies, *Sarcophaga bullata*: comparisons with *Drosophila*. *J Comp Neurol* 402:197-209.
- Forsythe ID, Tsujimoto T, Barnes-Davies M, Cuttle MF, Takahashi T (1998) Inactivation of presynaptic calcium current contributes to synaptic depression at a fast central synapse. *Neuron* 20:797-807.
- Grandes P, Streit P (1989) Glutamate-like immunoreactivity in calyces of Held. *J Neurocytol* 18:685-693.
- Grant L, Fuchs P (2008) Calcium- and calmodulin-dependent inactivation of calcium channels in inner hair cells of the rat cochlea. *J Neurophysiol* 99:2183-2193.
- Grynkiewicz G, Poenie M, Tsien RY (1985) A new generation of Ca²⁺ indicators with greatly improved fluorescence properties. *J Biol Chem* 260:3440-3450.
- Hackney CM, Osen KK, Ottersen OP, Storm-Mathisen J, Manjaly G (1996) Immunocytochemical evidence that glutamate is a neurotransmitter in the cochlear nerve: a quantitative study in the guinea-pig anteroventral cochlear nucleus. *Eur J Neurosci* 8:79-91.
- Hagiwara S, Ohmori H (1982) Studies of calcium channels in rat clonal pituitary cells with patch electrode voltage clamp. *J Physiol* 331:231-252.

- Harlow ML, Ress D, Stoschek A, Marshall RM, McMahan UJ (2001) The architecture of active zone material at the frog's neuromuscular junction. *Nature* 409:479-484.
- Heinemann SH, Conti F (1992) Nonstationary noise analysis and application to patch clamp recordings. *Methods Enzymol* 207:131-148.
- Held H (1893) Die zentrale Gehörleitung. *Arch Anat Physiol* 17:201-248.
- Helmchen F, Borst JG, Sakmann B (1997) Calcium dynamics associated with a single action potential in a CNS presynaptic terminal. *Biophys J* 72:1458-1471.
- Hessler NA, Shirke AM, Malinow R (1993) The probability of transmitter release at a mammalian central synapse. *Nature* 366:569-572.
- Heuser JE, Reese TS (1981) Structural changes after transmitter release at the frog neuromuscular junction. *J Cell Biol* 88:564-580.
- Hodgkin AL, Huxley AF (1952) A quantitative description of membrane current and its application to conduction and excitation in nerve. *J Physiol* 117:500-544.
- Hoffpauir BK, Grimes JL, Mathers PH, Spiro GA (2006) Synaptogenesis of the calyx of Held: rapid onset of function and one-to-one morphological innervation. *J Neurosci* 26:5511-5523.
- Inchauspe CG, Forsythe ID, Uchitel OD (2007) Changes in synaptic transmission properties due to the expression of N-type calcium channels at the calyx of Held synapse of mice lacking P/Q-type calcium channels. *J Physiol* 584:835-851.
- Ishikawa T, Kaneko M, Shin HS, Takahashi T (2005) Presynaptic N-type and P/Q-type Ca^{2+} channels mediating synaptic transmission at the calyx of Held of mice. *J Physiol* 568:199-209.
- Iwasaki S, Takahashi T (1998) Developmental changes in calcium channel types mediating synaptic transmission in rat auditory brainstem. *J Physiol* 509 (Pt 2):419-423.
- Iwasaki S, Momiyama A, Uchitel OD, Takahashi T (2000) Developmental changes in calcium channel types mediating central synaptic transmission. *J Neurosci* 20:59-65.
- Joris PX, Carney LH, Smith PH, Yin TC (1994) Enhancement of neural synchronization in the anteroventral cochlear nucleus. I. Responses to tones at the characteristic frequency. *J Neurophysiol* 71:1022-1036.
- Jun K, Piedras-Renteria ES, Smith SM, Wheeler DB, Lee SB, Lee TG, Chin H, Adams ME, Scheller RH, Tsien RW, Shin HS (1999) Ablation of P/Q-type Ca^{2+} channel currents, altered synaptic transmission, and progressive ataxia in mice lacking the $\alpha(1A)$ -subunit. *Proc Natl Acad Sci U S A* 96:15245-15250.
- Kasai H, Aosaki T (1988) Divalent cation dependent inactivation of the high-voltage-activated Ca -channel current in chick sensory neurons. *Pflügers Arch* 411:695-697.
- Kopp-Scheinpflug C, Tolnai S, Malmierca MS, Rübsamen R (2008) The medial nucleus of the trapezoid body: comparative physiology. *Neuroscience* 154:160-170.
- Kraus RL, Li Y, Grogan Y, Gotter AL, Uebele VN, Fox SV, Doran SM, Barrow JC, Yang ZQ, Reger TS, Koblan KS, Renger JJ (2010) In vitro characterization of T-type calcium channel antagonist TTA-A2 and in vivo effects on arousal in mice. *J Pharmacol Exp Ther* 335:409-417.
- Kreiner L, Lee A (2006) Endogenous and exogenous Ca^{2+} buffers differentially modulate Ca^{2+} -dependent inactivation of $\text{Ca}_v2.1$ Ca^{2+} channels. *J Biol Chem* 281:4691-4698.

- Kushmerick C, Price GD, Taschenberger H, Puente N, Renden R, Wadiche JI, Duvoisin RM, Grandes P, von Gersdorff H (2004) Retroinhibition of presynaptic Ca^{2+} currents by endocannabinoids released via postsynaptic mGluR activation at a calyx synapse. *J Neurosci* 24:5955-5965.
- Lee A, Scheuer T, Catterall WA (2000a) Ca^{2+} /calmodulin-dependent facilitation and inactivation of P/Q-type Ca_2^+ channels. *J Neurosci* 20:6830-6838.
- Lee A, Zhou H, Scheuer T, Catterall WA (2003) Molecular determinants of Ca^{2+} /calmodulin-dependent regulation of $\text{Ca}_v2.1$ channels. *Proc Natl Acad Sci U S A* 100:16059-16064.
- Lee SH, Rosenmund C, Schwaller B, Neher E (2000b) Differences in Ca^{2+} buffering properties between excitatory and inhibitory hippocampal neurons from the rat. *J Physiol* 525 Pt 2:405-418.
- Li L, Bischofberger J, Jonas P (2007) Differential gating and recruitment of P/Q-, N-, and R-type Ca^{2+} channels in hippocampal mossy fiber boutons. *J Neurosci* 27:13420-13429.
- Liang H, DeMaria CD, Erickson MG, Mori MX, Alseikhan BA, Yue DT (2003) Unified mechanisms of Ca_2^+ regulation across the Ca_2^+ channel family. *Neuron* 39:951-960.
- Limb CJ, Ryugo DK (2000) Development of primary axosomatic endings in the anteroventral cochlear nucleus of mice. *J Assoc Res Otolaryngol* 1:103-119.
- Lindau M, Neher E (1988) Patch-clamp techniques for time-resolved capacitance measurements in single cells. *Pflügers Arch* 411:137-146.
- Llinas R, Sugimori M, Simon SM (1982) Transmission by presynaptic spike-like depolarization in the squid giant synapse. *Proc Natl Acad Sci U S A* 79:2415-2419.
- Luebke JI, Dunlap K, Turner TJ (1993) Multiple calcium channel types control glutamatergic synaptic transmission in the hippocampus. *Neuron* 11:895-902.
- Miljanich GP, Ramachandran J (1995) Antagonists of neuronal calcium channels: structure, function, and therapeutic implications. *Annu Rev Pharmacol Toxicol* 35:707-734.
- Mintz IM, Adams ME, Bean BP (1992) P-type calcium channels in rat central and peripheral neurons. *Neuron* 9:85-95.
- Morad M, Davies NW, Kaplan JH, Lux HD (1988) Inactivation and block of calcium channels by photo-released Ca_2^+ in dorsal root ganglion neurons. *Science* 241:842-844.
- Muller M, Felmy F, Schneggenburger R (2008) A limited contribution of Ca^{2+} current facilitation to paired-pulse facilitation of transmitter release at the rat calyx of Held. *J Physiol* 586:5503-5520.
- Müller M, Felmy F, Schwaller B, Schneggenburger R (2007) Parvalbumin is a mobile presynaptic Ca^{2+} buffer in the calyx of held that accelerates the decay of Ca_2^+ and short-term facilitation. *J Neurosci* 27:2261-2271.
- Murthy VN, Sejnowski TJ, Stevens CF (1997) Heterogeneous release properties of visualized individual hippocampal synapses. *Neuron* 18:599-612.
- Nakamura T, Yamashita T, Saitoh N, Takahashi T (2008) Developmental changes in calcium/calmodulin-dependent inactivation of calcium currents at the rat calyx of Held. *J Physiol* 586:2253-2261.

- Nakamura Y, Takahashi T (2007) Developmental changes in potassium currents at the rat calyx of Held presynaptic terminal. *J Physiol* 581:1101-1112.
- Neher E (1998) Vesicle pools and Ca^{2+} microdomains: new tools for understanding their roles in neurotransmitter release. *Neuron* 20:389-399.
- Neises GR, Mattox DE, Gulley RL (1982) The maturation of the end bulb of Held in the rat anteroventral cochlear nucleus. *Anat Rec* 204:271-279.
- Newcomb R, Szoke B, Palma A, Wang G, Chen X, Hopkins W, Cong R, Miller J, Urge L, Tarczy-Hornoch K, Loo JA, Dooley DJ, Nadasdi L, Tsien RW, Lemos J, Miljanich G (1998) Selective peptide antagonist of the class E calcium channel from the venom of the tarantula *Hysterocrates gigas*. *Biochemistry* 37:15353-15362.
- Nicol MJ, Walmsley B (2002) Ultrastructural basis of synaptic transmission between endbulbs of Held and bushy cells in the rat cochlear nucleus. *J Physiol* 539:713-723.
- Oleskevich S, Walmsley B (2002) Synaptic transmission in the auditory brainstem of normal and congenitally deaf mice. *J Physiol* 540:447-455.
- Oleskevich S, Youssoufian M, Walmsley B (2004) Presynaptic plasticity at two giant auditory synapses in normal and deaf mice. *J Physiol* 560:709-719.
- Park HY, Kim SA, Korlach J, Rhoades E, Kwok LW, Zipfel WR, Waxham MN, Webb WW, Pollack L (2008) Conformational changes of calmodulin upon Ca^{2+} binding studied with a microfluidic mixer. *Proc Natl Acad Sci U S A* 105:542-547.
- Patil PG, Brody DL, Yue DT (1998) Preferential closed-state inactivation of neuronal calcium channels. *Neuron* 20:1027-1038.
- Pawson PA, Grinnell AD, Wolowske B (1998) Quantitative freeze-fracture analysis of the frog neuromuscular junction synapse--I. Naturally occurring variability in active zone structure. *J Neurocytol* 27:361-377.
- Perez-Reyes E (2003) Molecular physiology of low-voltage-activated t-type calcium channels. *Physiol Rev* 83:117-161.
- Randall A, Tsien RW (1995) Pharmacological dissection of multiple types of Ca^{2+} channel currents in rat cerebellar granule neurons. *J Neurosci* 15:2995-3012.
- Reim K, Mansour M, Varoqueaux F, McMahon HT, Südhof TC, Brose N, Rosenmund C (2001) Complexins regulate a late step in Ca^{2+} -dependent neurotransmitter release. *Cell* 104:71-81.
- Roberts WM, Jacobs RA, Hudspeth AJ (1990) Colocalization of ion channels involved in frequency selectivity and synaptic transmission at presynaptic active zones of hair cells. *J Neurosci* 10:3664-3684.
- Rodriguez-Contreras A, van Hove JS, Habets RL, Locher H, Borst JG (2008) Dynamic development of the calyx of Held synapse. *Proc Natl Acad Sci U S A* 105:5603-5608.
- Rollenhagen A, Satzler K, Rodriguez EP, Jonas P, Frotscher M, Lubke JH (2007) Structural determinants of transmission at large hippocampal mossy fiber synapses. *J Neurosci* 27:10434-10444.
- Rosenmund C, Clements JD, Westbrook GL (1993) Nonuniform probability of glutamate release at a hippocampal synapse. *Science* 262:754-757.

- Ryugo DK, Fekete DM (1982) Morphology of primary axosomatic endings in the anteroventral cochlear nucleus of the cat: a study of the endbulbs of Held. *J Comp Neurol* 210:239-257.
- Ryugo DK, Sento S (1991) Synaptic connections of the auditory nerve in cats: relationship between endbulbs of held and spherical bushy cells. *J Comp Neurol* 305:35-48.
- Ryugo DK, Wu MM, Pongstaporn T (1996) Activity-related features of synapse morphology: a study of endbulbs of held. *J Comp Neurol* 365:141-158.
- Ryugo DK, Montey KL, Wright AL, Bennett ML, Pongstaporn T (2006) Postnatal development of a large auditory nerve terminal: the endbulb of Held in cats. *Hear Res* 216-217:100-115.
- Sabatini BL, Regehr WG (1997) Control of neurotransmitter release by presynaptic waveform at the granule cell to Purkinje cell synapse. *J Neurosci* 17:3425-3435.
- Sakaba T, Neher E (2001) Quantitative relationship between transmitter release and calcium current at the calyx of Held synapse. *J Neurosci* 21:462-476.
- Sala F (1991) Activation kinetics of calcium currents in bull-frog sympathetic neurones. *J Physiol* 437:221-238.
- Sätzler K, Sohl LF, Bollmann JH, Borst JG, Frotscher M, Sakmann B, Lübke JH (2002) Three-dimensional reconstruction of a calyx of Held and its postsynaptic principal neuron in the medial nucleus of the trapezoid body. *J Neurosci* 22:10567-10579.
- Schneggenburger R, Neher E (2000) Intracellular calcium dependence of transmitter release rates at a fast central synapse. *Nature* 406:889-893.
- Schneggenburger R, Meyer AC, Neher E (1999) Released fraction and total size of a pool of immediately available transmitter quanta at a calyx synapse. *Neuron* 23:399-409.
- Shipe WD et al. (2008) Design, synthesis, and evaluation of a novel 4-aminomethyl-4-fluoropiperidine as a T-type Ca²⁺ channel antagonist. *J Med Chem* 51:3692-3695.
- Sigworth FJ (1980) The variance of sodium current fluctuations at the node of Ranvier. *J Physiol* 307:97-129.
- Sonntag M, Englitz B, Kopp-Scheinpflug C, Rübsamen R (2009) Early postnatal development of spontaneous and acoustically evoked discharge activity of principal cells of the medial nucleus of the trapezoid body: an in vivo study in mice. *J Neurosci* 29:9510-9520.
- Soong TW, DeMaria CD, Alvania RS, Zweifel LS, Liang MC, Mittman S, Agnew WS, Yue DT (2002) Systematic identification of splice variants in human P/Q-type channel $\alpha 1(2.1)$ subunits: implications for current density and Ca²⁺-dependent inactivation. *J Neurosci* 22:10142-10152.
- Striessnig J (1999) Pharmacology, structure and function of cardiac L-type Ca(2+) channels. *Cell Physiol Biochem* 9:242-269.
- Sun JY, Wu LG (2001) Fast kinetics of exocytosis revealed by simultaneous measurements of presynaptic capacitance and postsynaptic currents at a central synapse. *Neuron* 30:171-182.
- Tadross MR, Dick IE, Yue DT (2008) Mechanism of local and global Ca²⁺ sensing by calmodulin in complex with a Ca²⁺ channel. *Cell* 133:1228-1240.
- Takahashi T, Momiyama A (1993) Different types of calcium channels mediate central synaptic transmission. *Nature* 366:156-158.

- Takahashi T, Forsythe ID, Tsujimoto T, Barnes-Davies M, Onodera K (1996) Presynaptic calcium current modulation by a metabotropic glutamate receptor. *Science* 274:594-597.
- Taschenberger H, von Gersdorff H (2000) Fine-tuning an auditory synapse for speed and fidelity: developmental changes in presynaptic waveform, EPSC kinetics, and synaptic plasticity. *J Neurosci* 20:9162-9173.
- Taschenberger H, Leao RM, Rowland KC, Spirou GA, von Gersdorff H (2002) Optimizing synaptic architecture and efficiency for high-frequency transmission. *Neuron* 36:1127-1143.
- Townsend M, Yoshii A, Mishina M, Constantine-Paton M (2003) Developmental loss of miniature N-methyl-D-aspartate receptor currents in NR2A knockout mice. *Proc Natl Acad Sci U S A* 100:1340-1345.
- Tsien RW, Ellinor PT, Horne WA (1991) Molecular diversity of voltage-dependent Ca^{2+} channels. *Trends Pharmacol Sci* 12:349-354.
- Tsujimoto T, Jeromin A, Saitoh N, Roder JC, Takahashi T (2002) Neuronal calcium sensor 1 and activity-dependent facilitation of P/Q-type calcium currents at presynaptic nerve terminals. *Science* 295:2276-2279.
- von Gersdorff H, Schneggenburger R, Weis S, Neher E (1997) Presynaptic depression at a calyx synapse: the small contribution of metabotropic glutamate receptors. *J Neurosci* 17:8137-8146.
- Wadel K, Neher E, Sakaba T (2007) The coupling between synaptic vesicles and Ca^{2+} channels determines fast neurotransmitter release. *Neuron* 53:563-575.
- Walmsley B, Edwards FR, Tracey DJ (1988) Nonuniform release probabilities underlie quantal synaptic transmission at a mammalian excitatory central synapse. *J Neurophysiol* 60:889-908.
- Wang LY, Neher E, Taschenberger H (2008) Synaptic vesicles in mature calyx of Held synapses sense higher nanodomain calcium concentrations during action potential-evoked glutamate release. *J Neurosci* 28:14450-14458.
- Wang Y, Ren C, Manis PB (2010) Endbulb synaptic depression within the range of presynaptic spontaneous firing and its impact on the firing reliability of cochlear nucleus bushy neurons. *Hear Res* 270:101-109.
- Wölfel M, Lou X, Schneggenburger R (2007) A mechanism intrinsic to the vesicle fusion machinery determines fast and slow transmitter release at a large CNS synapse. *J Neurosci* 27:3198-3210.
- Wu LG, Borst JG, Sakmann B (1998) R-type Ca^{2+} currents evoke transmitter release at a rat central synapse. *Proc Natl Acad Sci U S A* 95:4720-4725.
- Wu LG, Westenbroek RE, Borst JG, Catterall WA, Sakmann B (1999) Calcium channel types with distinct presynaptic localization couple differentially to transmitter release in single calyx-type synapses. *J Neurosci* 19:726-736.
- Wu SH, Oertel D (1984) Intracellular injection with horseradish peroxidase of physiologically characterized stellate and bushy cells in slices of mouse anteroventral cochlear nucleus. *J Neurosci* 4:1577-1588.
- Xu-Friedman MA, Regehr WG (2003) Ultrastructural contributions to desensitization at cerebellar mossy fiber to granule cell synapses. *J Neurosci* 23:2182-2192.
- Xu J, Wu LG (2005) The decrease in the presynaptic calcium current is a major cause of short-term depression at a calyx-type synapse. *Neuron* 46:633-645.

-
- Yamashita T, Hige T, Takahashi T (2005) Vesicle endocytosis requires dynamin-dependent GTP hydrolysis at a fast CNS synapse. *Science* 307:124-127.
- Yang H, Xu-Friedman MA (2008) Relative roles of different mechanisms of depression at the mouse endbulb of Held. *J Neurophysiol* 99:2510-2521.
- Young SM, Jr., Neher E (2009) Synaptotagmin has an essential function in synaptic vesicle positioning for synchronous release in addition to its role as a calcium sensor. *Neuron* 63:482-496.
- Zhou Z, Neher E (1993) Mobile and immobile calcium buffers in bovine adrenal chromaffin cells. *J Physiol* 469:245-273.

Abbreviation

| | |
|-----------------|---|
| aCSF | artificial cerebrospinal fluid |
| ω -AgaTX | ω -agatoxin IVA |
| AMPA | a-Amino-3-hydroxy-5-methyl-4-isoxazolepropionic acid |
| AP | action potential |
| aVCN | anterior ventral cochlear nucleus |
| AZ | active zone |
| BAPTA | 1,2-bis(2-aminophenoxy)ethane-N,N,N',N'-tetraacetic acid |
| $[Ca^{2+}]_i$ | intracellular Ca^{2+} concentration |
| CBD | calmodulin-binding domain |
| CDI | Ca^{2+} -dependent inactivation |
| CDF | Ca^{2+} -dependent facilitation |
| C_m | membrane capacitance |
| CNQX | 6-cyano-7-nitroquinoxaline-2,3-dione |
| DNQX | 6,7-dinitroquinoxaline-2,3-dione |
| EGTA | ethylene glycol-bis(2-aminoethylether)-N,N,N',N'-tetraacetic acid |
| EPSC | excitatory postsynaptic currents |
| GBC | globular bushy cells |
| HH-model | Hodgkin–Huxley model |
| HVA | high voltage activated |
| $I_{Ca(V)}$ | presynaptic Ca^{2+} currents |
| LSO | lateral superior |
| LVA | low voltage activated |
| mGluR | metabotropic glutamate receptor |
| MNTB | medial nucleus of the trapezoid body |
| NMDA | N-methyl-D-aspartate |
| SBC | spherical bushy cell |
| SCG | superior cervical ganglion |
| SOC | superior olivary complex |
| TEA | tetraethylammonium |
| TTX | tetrodotoxin |
| VGCC | voltage-gated calcium channels |

Acknowledgment

First, I would like to thank my supervisor Dr Holger Taschenberger for giving me this opportunity to work in his group, for his patience he took in teaching me the theory of electrophysiology, for his tremendous support and for being a model scientist during my whole PhD project. My sincere thanks to the head of the department Prof. Erwin Neher and the members of my PhD committee, Dr Takeshi Sakaba and Prof. Tobias Moser for their critical suggestions and friendly support throughout my PhD years.

Thanks to all the members of the departments, specially to Dr. Lijun Yao and Dr. Jin Bao for very kindly instruction of patch-clamp techniques at the beginning of my study; Dr. Chao-Hua Huang, Yunfeng Hua, and Raunak Sinha were always around to help, support and discuss with me. In addition, I am heartily thankful to my desk neighbors Yunxiang Chu, I-Wen Chen and Shu-Wen Chang who always supplied me cookies, listened my complains and shared my happiness in the laboratory. Moreover, Dr. Nobutake Hosoi and Dr. Kristian Wadel, without your helpful “criticism”, flash photolysis experiments can not be finished in my project. Thanks a lot. Also, many thanks to Irmgard Barteczko, for her helps in life and administerial stuffs. I would like to give my sincere thanks to Sigrid Schmidt and Ina Herfort for her excellent technical assistances.

Big thanks to all my friends in Göttingen. I really have wonderful time in these thousand days here. I would like to extend my thanks to my parents and brother for all the love and

support. Finally, I am sincerely grateful to my girlfriend, Han-Ning Chuang for her great help, accompany and essential support in my life.

Curriculum Vitae

Personal information

Name: Kun-Han Lin
E-mail: klin@gwdg.de
Gender: Male
Date of birth: 29.11.1980
Place of birth: Tainan, Taiwan
Citizenship: Taiwanese

Education

2008 – 2011: **PhD project** in the research group for activity-dependent and developmental plasticity at the calyx of Held at Max Planck Institute for Biophysical Chemistry Göttingen, Germany
Sensory and Motor Neuroscience program in the Göttingen graduate school for neurosciences and molecular bioscience George August-University Göttingen, Germany

2002 – 2004: **M.Sc.** in Science
Institute of Biochemistry
National Yang-Ming University
Taipei, Taiwan

1998 – 2002: **B.Sc.** in Agriculture
Department of Agricultural Chemistry
National Taiwan University
Taipei, Taiwan

Publication list

1. Lin KH, Erazo-Fischer E, Taschenberger H. Similar intracellular Ca^{2+} requirements for inactivation and facilitation of voltage-gated Ca^{2+} channels in a glutamatergic mammalian nerve terminal. (in preparation)
2. Lin KH, Oleskevich S, Taschenberger H. Presynaptic Ca^{2+} influx and vesicle exocytosis at mouse endbulb of Held terminals: a comparison of two auditory nerve terminals. (under revision)
3. Lin CC, Huang CC, Lin KH, Cheng KH, Yang DM, Tsai YS, Ong RY, Huang YN, Kao LS (2007). Visualization of Rab3A dissociation during exocytosis : A study by total internal reflection microscopy. The journal of Cell Physiology; 211(2):316-26.